STRUCTURAL CHANGES AND DIFFUSION OF VACANCY CLUSTERS IN DIAMOND AND PARACYCLOPHANE CYCLOADDITION: INSIGHTS INTO UNUSUAL CARBON BONDING

A Dissertation
submitted to the Faculty of the
Graduate School of Arts and Sciences
of Georgetown University
in partial fulfillment of the requirements for the
degree of
Doctor of Philosophy
in Chemistry

By

Brad M. Slepetz, B.S.

Washington, DC
July 17, 2013

Copyright 2013 by Brad M. Slepetz
All Rights Reserved

STRUCTURAL CHANGES AND DIFFUSION OF VACANCY CLUSTERS IN DIAMOND AND PARACYCLOPHANE CYCLOADDITION: INSIGHTS INTO UNUSUAL CARBON BONDING

Brad M. Slepetz, B.S.

Thesis Advisor: Miklos Kertesz, Ph. D.

ABSTRACT

High energy irradiation of diamond produces point defects that are observable by spectroscopy. While many defects have been confirmed such as the monovacancy V_1, the divacancy V_2, and various interstitials, most remain unidentified. The prediction of the properties of these defects through computational modeling is an important ally in solving these mysteries. Computational work on smaller vacancy clusters V_n in diamond had previously been performed with n up to 14 but these were always done with assumptions about that structures of the low energy clusters. A novel generational algorithm has allowed for the identification of the low energy clusters without structural bias. By going beyond n=14 insights have been made into the structural optimizations of large voids in carbon materials, which is important in helping describe Carbide-derived carbons (CDCs) at the atomistic level. Studying the mechanism of V_2 formation has uncovered multiple stable non-contiguous divacancy structures with high spin that may be found in the ESR. The unique environment of vacancy clusters, within the rigid framework of the diamond lattice, gives rise to unusual carbon-carbon bond lengths. Molecular analogous where this kind of bonding can be found are rare but paracylophanes—which undergo [4+4] cycloaddition, spanning the spectrum of sp^2 to sp^3-hybridized carbon—are one example. This process mimics the diamond-to-graphite transition, the modeling of which offers valuable insight.

ACKNOWLEDGEMENTS

No one accomplishes anything by themselves and I am no exception. I am deeply grateful to many people, not all of whom I will be able to mention here. I am forever indebted to Professor Miklos Kertesz for accepting me into his laboratory and offering his never failing support. Few graduate students have boasted a mentor that is as accessible and encouraging as Miklos. His patience and helpfulness serve as an inspiration and will not be forgotten.

My predecessors in the Kertesz lab helped me learn the arcane computational chemistry language and learn the practical tools of the trade that allowed me to actually do my work. I am especially grateful Dr. Yonghui Tian, Dr. Shujiang Yang, and Dr. Jingson Huang for helping me acclimate to the group and feel accepted. Many undergraduate students have come through the lab and provided important work and I am grateful to Michael Roumanos for his computer science expertise and conversation banter and to David Hyde-Volpe for his summer work on the [V-C=C-V] project that I conceived.

My first project could not have been performed without the work of Professor Istvan Laszlo who wrote the tight-binding code that used for most of the calculations on vacancy clusters. His visits to the lab were indispensable. Collobrations with Professor Jack Fisher and Professor Yuri Gogotsi were very helpful in developing our course of research for vacancy clusters.

My committee members, past and present, have served as important helping hands in guiding my research, both with direct input concerning my work and also as instructors in

courses I found useful or interesting. These include Professor Toshiko Ichiye, Professor Tim Warren, Professor Bahram Moasser, Professor Holman.

A special acknowledgement is extended to Professor Amy Liu and Professor Richard Weiss. Professor Liu was extremely helpful teaching aspects of the PWscf program, which I used extensively, and interpreting the results. Professor Weiss offered the important eyes of an experimental organic chemist that has helped us wrap our mind around what we calculate.

One cannot do computational chemistry without computers and I am indebted to Mr. Ainsley Gibson, Mr. Jess Cannata, Mr. Woonki Chung, and Mr. William Craig for their roles in maintaining the various servers on which I did my calculations. These gentlemen were always available and helpful no matter how trivial my issue.

Finally, I would like to thank my family; my father who has encouraged me with positive reinforcement in whatever I have endeavored since birth and my sister who has shared her support and empathized with my successes and failures. It is regrettable that my mother did not live to see my academic success as I am sure she would be proud.

TABLE OF CONTENTS

CHAPTER 1

INTRODUCTION

Until the discovery of buckminsterfullerene in 1985[1] carbon was known to exist primarily in three solid allotropes: diamond, graphite, and amorphous carbon. In diamond, each carbon atom is tetrahedrally bonded to its neighbors creating a sp^3 network and are broadly divided into two types: cubic and hexagonal. Cubic diamond belongs to the $Fd\bar{3}m$-O_h^7 space group, has eight atoms in the unit cell, and a lattice constant of 3.5669[2]. All bond lengths are equivalent to 1.54 Å. The structure repeats after the third layer, or has an ABC motif. Cubic diamond may be further divided into types I*a*, I*b*, II*a*, and II*b* based on impurity concentration (primarily nitrogen) and subtle differences in the absorbance spectra, particularly the ultraviolet (UV) and infrared (IR); however, there are no noticeable variations in the lattice constant between these types[2]. Hexagonal diamond was first reported in 1967[3] and has the same cyclohexane-like layers as the cubic form but repeats after the second layer (ABA pattern). The result is a structure with lattice constants $a = b \neq c$, where a = 251 pm, c = 412 pm, and the interatomic distances are the same as found in cubic diamond. Except where noted, all references to diamond herein assume the cubic variety.

Graphite is quite different, displaying an aromatic network of sp^2 bonded carbons separated into planar sheets, about 3.4 Å apart[2]. Graphite competes energetically with diamond and at ordinary temperatures and pressures is slightly more stable[7] by 2.9 kJ mol^{-1}, owing primarily to the energy gain of aromaticity in forming the sp^2 planar network. The structure is hexagonal with the aromatic layers offset in such a way that the C_6 units do not directly overlap.

Instead, the C_6 unit of one layer is positioned so that an atom from the C_6 unit above or below is positioned directly in the center of the ring[2].

Amorphous carbon is defined by its complete lack of long-range regularity[2] and crystalline structure. Natural sources of amorphous carbon—such as soot—can contain impurities of both graphite and diamond. The advent of fullerenes, such as C_{60}, has increased the data bank of carbon allotropes to include many carbon molecules. Chief among these are nanotubes[4], which can be thought of as cylindrically shaped fullerenes that may be open or closed at either end.

No crystal is flawless and several kinds of imperfections deform the ideal diamond lattice. Aside from the fact that most diamond samples are mixtures of type I and II, inpurities may contaminate the solid (most notably nitrogen and boron)[5]. Another imperfection is the point defect, a distortion localized to a few neighboring lattice sites. The simplest point defect is the vacancy, which is a displaced atom from a lattice site. Isolated vacancies have an energetic motive for aggregation (to minimize 'dangling bonds') and this thesis deals with contiguous vacancy clusters V_n , n vacancies that would be connected in the diamond lattice had they not been absent. Vacated atoms may be displaced into non-ideal locations forcing abnormal bonding schemes between itself and its newest neighbors; such a defect is known as an interstitial. When a vacancy and interstitial occur in nearby space they are referred to as a Frenkel pair[6].

The absorption spectrum of natural diamond has been well studied. Like most insulators, the spectra for diamond is "transparent at long wavelengths and absorb strongly for wavelengths shorter than a certain value[7]." The change in absorbance is abrupt and is attributed to the transition from the valence band to the conduction band, and is thus a measure of the band gap. In type II*a* diamond the absorbance lacks any sharp peaks until a rapid rise at ca. 5.5 eV. When

diamond is irradiated with high energy electrons, neutrons, or gamma rays[8], sharp peaks are observed within the forbidden gap.

Many of these peaks have been assigned to specific point defects in the literature. The GR1 band (for general radiation, Clark's nomenclature[5]) with a zero-phonon line at 1.674 eV has been attributed[9] to the transition from the ground ^1E state to an excited $^1T_2$ state in the diamond monovacancy. The negatively charged monovacancy has been identified[10] with the ND1 band (natural diamond[5]) at 3.149 eV, as well as from the S1 electron paramagnetic resonance (EPR) center[11] with S = 3/2 . Though the ground state of the neutral vacancy is closed shell (see below) the $^5A_2$ excited state of the neutral vacancy has been identified[12] via EPR. Other successes of EPR spectroscopy in diamond have been cited[13] in identifying higher vacancy *chains*, along the 'zigzag' <110> direction, V_n, where n = 3, 4, 5, 6, 7, 8. Higher vacancy *clusters* with n = 9, 11, 13 have been tentatively assigned[14] as well from their S = 1 centers. The proposed structures of V_{11} and V_{13} do not match the low energy clusters predicted by Laszlo, et al.[15] by symmetry and we discuss the plausibility of these structures.

The first theoretical treatment of the monovacancy in diamond was given by Coulson and Kearsley[16]. They begin with a model in which an atom is removed from the lattice revealing four "dangling bonds," or sp^3 hybrid orbitals directed towards the vacated atom. The dangling bonds are each occupied by a single electron, for a total of four, arranged in a tetrahedral of T_d symmetry. The linear combination of atomic orbitals (LCAO) of the dangling bonds is used to find the suitable symmetry-allowed wave functions. The result is a configuration that lies within the band gap including one singly degenerate orbital of A_1 symmetry lying below a triply degenerate set of symmetry T_2. Coulson then considers all possible electron configurations and their resultant states, which are linear combinations of Slater determinants. The energies of

configurations are calculated by solving the Schrodinger equation with a Hamiltonian that includes approximate potential energy terms expressed as Coulomb repulsions in the field of electron charge clouds,

$$H = \sum_i T_i + V_i + \tfrac{1}{2}\sum_{i \neq j} \frac{1}{r_{ij}}$$

$$V_i = V_{Ai} + V_{Bi} + V_{Ci} + V_{Di} \ ,$$

where *i*, *j* index the vacancy electrons (four when neutral) and V_{Ai} accounts for the attraction between vacancy atom *A* and vacancy electron *i* as well as the repulsion due to two core shell electrons on atom *A* and the repulsion from the remaining three hybrids. The energies may then be calculated via method of variations. Coulson found the neutral vacancy to be in a ground state ^1E, lying about 2 eV below a $^3T_1$ state, verified by magnetic circular dichroism in 1977[17]. Jahn-Teller relaxations[18] occur when a degenerate orbital is partially filled (Figure 1). In such a case, the symmetry will be lowered by splitting the degeneracy of the partially filled orbital into two new orbitals, one of higher energy and one of lower energy with the lower energy orbital now filled to yield a closed shell configuration. Though a one-electron model of the monovacancy in diamond is subject to Jahn-Teller relaxation, the ground electronic state precludes this deformation. The relaxation may be dynamical with a low activation barrier. In any case, a simple one electron theory is not sufficient in describing the electronic states of the monovacancy. The ground state is closed shell and the geometry distorts symmetrically, retaining T_d symmetry, and the center is has not been identified with an EPR spectrum. Whether the distortion is inward or outward has yet to be verified. While the monovacancy in diamond has been well studied the true nature of the geometry is not understood and information about higher vacancies in the literature is sparse. The few experiments that been performed on multi-vacancy clusters is tenuous. Accurate calculations are needed to understand and identify peaks

found in the absorption spectra of irradiated diamonds. Knowledge of the stabilities of high vacancy clusters will give insight into the mechanisms at work inside porous carbon materials.

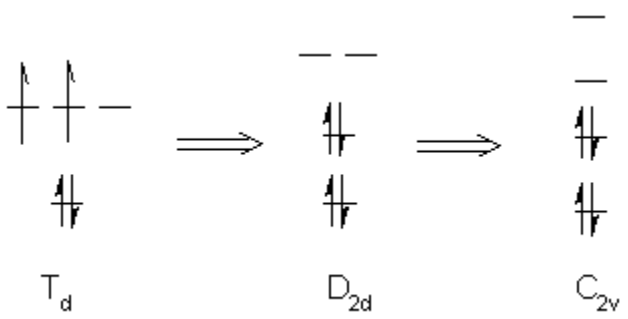

Figure 1. A one electron theory predicts the symmetry of the monovacancy's nearest neighbors in diamond to be reduced from T_d to D_{2d}. TBDFT predicts C_{2v} symmetry (see Table 2).

The stability and formation preference of extended contiguous vacancy clusters in diamond give atomistic insight into the electrical mechanisms of carbon porous materials, such as the carbide derived carbon supercapacitors of Gogotsi's group[19]. Initially, it appears that adamantane-like (Figure 2) vacancy structures are favored—because closed clusters minimize dangling bonds—but eventually graphitization of the atoms becomes energetically competitive and then favorable. In addition to interesting electrical properties, nanoporous carbon materials potentially offer new opportunities for gas sorption and transport[19]. Small vacancies have been studied using the supercell periodic boundary condition and finite cluster method. Simple force field simulations based on a Brenner[20] or Dreiding[21] potential allow theoreticians to get a first-approximation to how simple gases such as hydrogen and oxygen react or remain unreacted inside the studied cavities. It is the purpose of this thesis to develop insight into the stabilities of higher vacancy clusters in diamond to learn the nature of the reconstruction around the voids as a model for porous carbon materials. Quantum effects are necessary to model large vacancy clusters because of the inevitable competition between sp^2 and sp^3 hybridization. The

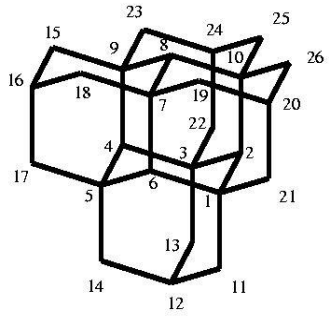

Figure 2. Closed loop "adamantine" structures that may be excised from the diamond lattice by removing the carbon atoms sequentially as numbered.

large number of structures that we deal with necessitate an economical method and we choose a tight-binding density functional approach[22] to deal with most clusters with higher levels that include electron correlation for special cases.

References

[1] Kroto, H. W.; Heath, J. R.; O'Brien, S. C.; Curi, R. F.; Smalley, R. E. *Nature*. **1985**, *318*, 162-163.

[2] Donohue, J. *The Structures of the Elements*; Wiley: New York, NY, 1974; pp 250-261.

[3] Bundy, F. P.; Kasper, J. S. *J. Chem. Phys*. **1967**, *57*, 1-12.

[4] Colbert, D. T.; Smalley, R. E. In *Perspectives of Fullerene Nanotechnology*. Osawa, E.; Kluwer Academic: Boston, MA, 2002; p 5.

[5] Clark, C. D. In *The Physical Properties of Diamond*; Berman, R.; Oxford, 1965; pp 295-324.

[6] Frenkel, Y. I. *Zetschrift feur Physik*. **1926**, *35*, 652-659.

[7] Clark, C. D.; Ditchburn, R. W.; Dyer, H. B. *Proc. Roy. Soc. A*. **1956**, *234*, 363-381.

[8] Goss, J. P.; Rayson, M. J.; Briddon, P. R. *Phys. Rev. B*. **2007**, *76*, 045203.

[9] Douglas, I. N.; Runciman, W. A. *J. Phys. C: Solid State Phys.* **1977**, *10*, 2253-2259.

[10] Davies, G. *Nature*. **1977**, *269*, 498.

[11] Isoya, J.; Kanda, H.; Uchida, Y.; Lawson, S. C.; Yamasaki, S.; Itoh, H.; Morita, Y. *Phys. Rev. B*. **1992**, *45*, 1436-1439.

[12] van Wyk, J. A.; Tucker, O. D.; Newton, M. E.; Baker, J. M.; Woods, G. S.; Spear, P. *Phys. Rev. B*. **1995**, *52*, 657-666.

[13] Iakoubovskii, K.; Stesmans, A. *Phys. Rev. B*. **2002**, *66*, 04506.

[14] Iakoubovskii, K; Stesmans, A. *Phys. Stat. Sol. A*. **2004**, *201*, 2509-2525.

[15] Laszlo, I.; Kertesz, M; Gogotsi, Y. *Mater. Res. Soc. Symp. Proc.* **2007**, 978.

[16] Coulson, C. A.; Kearsley, M. J. *Proc. R. Soc. A*. **1957**, *241*, 433-454.

[17] Douglas, I. N.; Runciman, W. A. *J. Phys. C: Solid State Phys.* **1977**, *10*, 2253-2259.

[18] Jahn, H. A.; Teller, E. *Proc. R. Soc. A*. **1937**, *161*, 220-235.

[19] Chmiola, J.; Yushin, G.; Gogotsi, Y.; Portet, C.; Simon, P.; Taberna, P. L. *Science*. **2006**, *313*, 1760-1763.

[20] Brenner, D. W. *Phys. Rev. B*. **1990**, *42*, 9458-9471.

[21] Mayo, S. L.; Olafson, B. D.; Goddard III, W. A. *J. Phys. Chem*. **1990**, *94*, 8897-8909.

[22] D. Porezag, Th. Frauenheim, Th. Köhler, G. Seifert, R. Kaschner, *Phys. Rev. B* **51**, (1995), p.12947.

CHAPTER 2

SIMULATIONS OF LARGE MULTI-ATOM VACANCIES IN DIAMOND[*]

Abstract

We generated and evaluated energetically a very large number of vacancy V_n clusters representing nanosize voids or cavities in diamond for n up to 14 using a new generational algorithm. We evaluated the relaxed geometries and energies of these contiguous vacancy clusters using a tight binding density functional theory (TBDFT). For up to n=7 we generated all possible structures and evaluated their relaxed geometries. For n=8 through n=14 we selectively generated a large number of vacancy clusters and obtained highly stable structures and their energies. By analyzing the energy levels and the corresponding orbitals, we identified the surface states of the voids and their symmetries. Significant differences with respect to vacancy clusters in silicon were found. The results were interpreted by finding that certain structures become relatively more stable due to a process we call local graphitization, which can be identified by a tetrahedron of graphitization (TOG), and it can be characterized by elongation of certain carbon-carbon contacts and by the concomitant appearance of new states in the gap. The beginning of graphitization, as indicated by geometrical and energetic descriptors in small stable vacancy clusters, may have a role in the formation mechanisms of various sp^2 hybridized structures in carbons.

[*] Reproduced with permission from [Laszlo, I.; Kertesz, M.; Slepetz, B.; Gogotsi, Y. *Diam Relat. Mater.* **2010**, *19*, 1153-1162] Copyright [2010] Elsevier.

1. Introduction

With the recent development in the production of porous carbons with controllable pore size[1] the basic question arises: what are the stable pore sizes and shapes in porous carbons on the nanoscale? The size and shape of pores have a profound effect on the energetics of adsorptive storage, which is of great potential technological importance. The problem of modeling a missing group of n atoms—a V_n vacancy cluster—has received considerable attention in silicon, providing a basis of comparison for similar experimental[2-5] and theoretical[6-10] work on diamond vacancy clusters. Due to the rich chemistry of carbon with its unique energetics of the close lying sp, sp^2, and sp^3 states (as opposed to the typically sp^3 hybridized silicon) suggests that stable carbon vacancy clusters might display a dazzling variety of shapes and sizes. These clusters will also greatly affect the optical properties of diamond. The literature on the modeling of vacancy clusters in diamond has been limited to either small clusters or to selecting representative samples from the astronomical number of combinatorially possible structures. Our goal is to:

a. Enumerate all distinct structures of V_n vacancy clusters with increasing n.

b. Evaluate a large number of V_n vacancy clusters (evaluation of all for large n is not possible) at a realistic level of quantum mechanical theory. Then, describe the optimized structures, their electronic states and total energies and any emerging trends in these descriptors.

c. Interpret the driving forces of the distortions originating in the ability of the dangling orbital electrons to form multicenter combinations that lower the energy of the vacancy clusters.

A simple model of electronic structure of these systems can be obtained by imagining the vacancy cluster as being generated by severing the bonds and removing n atoms following the model developed for V_1 by Coulson and Kearsley.[28] The number of such severed bonds, *sb*, depends on n and the topology of the given vacancy cluster. E.g. *sb*=4 for V_1, *sb*=6 for V_2. Each severed bond leaves behind an sp^3-like dangling bond orbital with a single electron. These dangling bond orbitals form various multicenter combinations, the lowest one being always the most bonding. In all cases we encountered in this work we found the lowest orbital is sufficiently stabilized to make it appear below the highest occupied band energy level, similar to the a_1 orbital for V_1 found by Coulson and Kearsley. Therefore, the number of dangling bond orbitals within the gap is less than *sb*. We will refer to these dangling bond orbitals within the gap as *s* before relaxation and *s'* after relaxation. These levels in the gap are mostly dangling bond levels and the geometrical relaxation of the vacancy cluster tends to increase s' relative to s. Due to the multicenter bonding specific to each vacancy cluster, it is also expected that the simulation will produce carbon-carbon contacts that are unusual in terms of coordination numbers and geometry.

Given the large number of possible structures for larger n (for details see later) it was necessary to develop an algorithm that generates low energy structures. The diversity of stable structures without structural bias needs to be known before any atomistic interpretation of medium and large vacancy clusters can begin. If in fact these structures do not show structural diversity that needs to be known as well. Alas, due to the extremely large number of possible

structures highly accurate ab initio methods[12] can be used only for a very limited number of vacancy clusters. TBDFT[11] level of theory offers qualitative and even sometimes quantitative results. Even the more sophisticated conventional *ab initio* methods[7-10] have to be improved to obtain the level of accuracy offered e.g. by Quantum Monte Carlo methods in the relatively simple case of a monoatomic vacancy (V_1) in diamond.[12]

The paper is structured as follows. First, we briefly review previous work on Si and diamond vacancy clusters. We discuss "adamantane-like" structures which ought to be particularly stable by simply counting the number of bonds cut. Then, we develop an algorithm to generate connected vacancy clusters, V_n, of increasing number of *n* missing atoms starting from a monoatomic vacancy, V_1. This is followed by a description of our results obtained for the most stable V_n vacancy clusters for n=1,2,...14.

2. Vacancy clusters in diamond

In diamond, more than 500 electronic and more than 150 vibrational optical centers have been documented.[37-39] The purpose of this section is to review key information relevant to the discussion. About half of these defects are believed to be related to impurity atoms which are outside of our scope. In our paper we shall study the defects related to connected V_n vacancy clusters. Single vacancies and interstitials can be produced by irradiation of diamond and the interstitials can be removed by annealing at about T = 400 ^{o}C.[23] It was found[20] that by annealing at T = 600 ^{o}C, single vacancies V_1 migrate and form divacancies V_2. Divacancies anneal out at T = 800 ^{o}C producing a series of EPR active S = 1 centers labeled R5, O1, R6, R10, R11, and

KUL11.[6, 23, 24] These centers are respectively associated with $\langle 110 \rangle$ -oriented vacancy chains with n = 3 to 8 by Iakoubovskii and Stesmans[2], although the concentration of the *n*-vacancy chains rapidly decreases with *n*. At T = 1150 ^{o}C all of these vacancy chains anneal out producing more stable vacancy clusters.[2] .

Baker's model for vacancy cluster formation[6] assumes that the clusters of vacancies must have been created by accumulation of migrating vacancies such that a "family tree of ancestors" with sufficient stabilities and life times can be identified. From this genealogical approach it follows that the steps to accumulate any particular cluster must involve precursors with the same configuration of vacancies, less one or two adjacent vacancies. These precursors must have been relatively stable and they should be observable as independent defects.[6] Baker's approach revealed some shortcomings of earlier models and provides useful guidelines for vacancy cluster growth. The consideration of genealogy of vacancy construction[6] is built into our algorithm described in Sec. 4.

Hounsome et al.[25] studied $\langle 110 \rangle$ vacancy chains, multi-vacancy clusters and vacancy discs in diamond using DFT with the AIMPRO and DFTB codes[26,27]. The multi-vacancy clusters under study were the clusters *a*-V_n (from n = 1 to n = 14) of Fig. 1 and their formation energies were calculated in the S = 0 and S = 1 spin states with the AIMPRO method. These clusters were obtained by minimizing the number of dangling bonds in analogy to Si vacancy clusters. In all cases, the more compact adamantane-like clusters were more energetically favourable than the $\langle 110 \rangle$ chains. Exceptionally stable clusters were found with the V_6, V_{10} and V_{14} adamantane-like

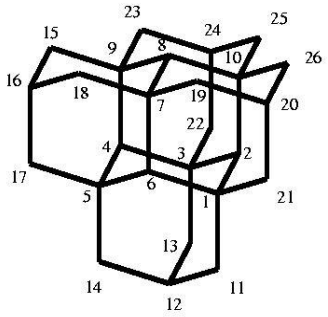

FIG. 1. Labeling of vacancy clusters. If it is not stated otherwise the vacancy cluster V_n is labelled in the order of removal of vacancy atoms. E.g. *a*-V_6 and *a*-V_{10} correspond to the removal of the first six and ten atoms in this figure, respectively. Clusters generated in this manner are all "adamantane-like" and are denoted as *a*-V_n.

vacancy clusters just as in the case of silicon, but for the diamond V_6, they did not obtain the healing phenomenon described by Hastings et al.[16] Further, they observed that the {111} vacancy disc, consisting of a {111} double plane of vacancies, had a much lower formation energy per vacancy at 1.20 eV than any of the multi-vacancy point defects. However, as stated in the introduction, no systematic large scale generation of clusters and their geometry optimization has been performed so far.

3. Energy calculations and structural descriptors

In our total energy calculations we used TBDFT[11] in the framework of periodic boundary conditions for the conventional cubic supercell of (N - n) atoms. n varied from 1 to 14, and N was 216. This parametrized non-SCF method uses only one s and three p orbitals on each carbon atom and has well known limitations but it is very fast computationally. The equilibrium positions of the atoms were determined by the conjugate gradient method and due to the large number of possible cases we restricted ourselves to the Γ-point approximation. In each V_n cluster calculation, we first doubly occupied the lowest 2(N-n) energy levels of the available 4(N-n) levels. For determining the most stable structures we developed an algorithm to generate

V_n vacancy clusters from those of the previous generation V_{n-1} by adding a V_1. The most stable vacancy cluster generated is V_{n_1} and V_{n_k} is the k-th in the order of stability.

After generating a list of V_{n_k} vacancy clusters having decreasing stability with increasing k, we recalculated the geometry of the most stable ones for testing our results obtained by only 50 conjugate gradient steps using partial occupation numbers when the highest orbitals were degenerate. The surface atoms are defined as those with one or more cut bonds. A bond is considered cut if either it has a neighbour in the V_n or if its original first neighbour distance increased due to relaxation to a distance greater than 1.9Å. A vacancy atom with three cut bonds defines three adjacent surface atoms. The distances among these are denoted by r_1, r_2, and r_3. A vacancy atom with two cut bonds defines two surface atoms; their distance is marked by r_4. Distances between a four coordinated atom and its neighbors are referred to as r_a, r_b, r_c and r_d. The deformation of the surrounding of such a motif adjacent to vacancies leads to the shortening of three bonds, and the lengthening of a bond perpendicular to the plane of these three bonds defined by the corresponding three neighboring atoms. We used tetrahedra to describe these locally distorted "graphitized" structures helping to identify these situations effectively. We use the term tetrahedron of graphitization, TOG, to identify these structural motifs that play a key role in this work.

For comparison we provide the corresponding distances of the ideal diamond structure in parentheses when needed. For reference, our optimized diamond structure corresponds to r_{CC} = 1.5487Å. The symmetry of a V_n is defined by the symmetry of its surface atoms. We have calculated the symmetries of the orbitals using only its coefficients on the surface atoms. Thus, $n\lambda$ is the n-th molecular orbital that belongs to the irreducible representation λ. Thus e.g. $429a_1$,

refers to the 429-th orbital A_1 irreducible representation. For the N=216 supercell without vacancies (n=0), we obtained for the Highest Occupied Molecular Orbital and Lowest Unoccupied Molecular Orbital: HOMO = -5.17eV and LUMO = 2.27eV which were used as the gap of diamond. We also refer to the total weight on the dangling orbitals of various orbitals that play an active role in the properties of a given V_n. These are normalized sums or atomic orbital coefficients on the surface atoms of a vacancy cluster and help identify bulk vs. surface states.

4. Algorithm for generating connected vacancy clusters*

In the previous sections, we have seen two procedures for generating vacancy clusters. They are the hexagonal ring clusters (HRC) and the spherically shaped clusters (SPC) method. The HRC method can be seen as a procedure for minimizing the number of dangling bonds, N_{DB} . Both procedures remove atoms one after the other from an ideal diamond structure. If a vacancy cluster V_n has already been generated, the next V_{n+1} cluster can be generated in several ways by removing one atom that is directly connected to another in V_n. The number of such sites grows fast as n increases. A particular V_{n+1} cluster so generated can be identical to another if they can be transformed into each other by translation, rotation, reflection or any combination of these transformations.

The following algorithm generates our vacancy clusters of *n* missing adjacent atoms from the lattice for each *n*, starting with V_1. The algorithm uses a diamond lattice (the *Ur lattice*) on

* Algorithm developed by Istvan Laszlo

which some of the steps of the algorithm are executed. All calculations refer to periodic boundary conditions using a supercell with N - n atoms (N sites, n vacancies).

1. We start with the monoatomic V_1 vacancy, and increase n one by one.
2. Generate all possible V_n vacancy clusters on the lattice by adding one neighboring atom in all possible positions for each of the V_{n-1} vacancy clusters that were generated in the previous step with sufficiently low energies to be kept on the list.
3. Eliminate the inequivalent vacancy clusters on the *Ur*-lattice based on the eigenvalues of the modified adjacency matrix and only one of each equivalent set is kept. The number of the inequivalent structures in step n is I_n.
4. Optimize the geometries of all I_n structures.
5. Calculate the formation energies for all V_n vacancy structures obtained.
6. Keep only the M_n lowest energy vacancy clusters. M_n should be as large as permitted by the computational facilities.
7. n → n+1, and GO TO 2. The process terminates at a predetermined n value.

Steps 2 and *3* are executed on the ideal *Ur*-lattice, not on the optimized structures (even if those are available), turning the process into a discrete problem. In *Step* 2, the algorithm checks all atoms on the inner surface of each of the M_{n-1} vacancy clusters adding one more missing atom from that surface. The surface is defined as atoms that have less than four adjacent (connected) atoms. A practical element of this modeling is that the connectivities of each structure can be easily reconstructed. Selection of equivalent structures in *Step* 3 was done by diagonalizing the modified adjacency matrix, D which is defined as the transformed interatomic distances, $r_{i,j}$:

$$D_{i,j} = \exp(-ar_{i,j}) \qquad (3)$$

Two structures are considered equivalent if their eigenvalues are the same. In our calculations we used a=1.0Å^{-1}. The conventional adjacency matrix, A, is obtained from D when only first neighbor distances are considered which are all taken to be the same. The advantage of diagonalizing D instead of A is that certain structures that are degenerate for A are not degenerate for D allowing a finer discrimination of structures. This is important, since in the selection process degenerate structures, if kept, would create a computational overload and may significantly reduce the diversity of the final structures. Using the abovementioned algorithm, we have calculated the number of all possible vacancy clusters in the range from V_1 to V_{14}. The notation n(p/q) means that the number of all possible V_n vacancy clusters is p which was reduced to q inequivalent ones. We obtained the following results: 1(1/1), 2(4/1), 3(6/1), 4(8,3), 5(30/7), 6(83/24), 7(328/88), 8(1357/385), 9(6617/1713), 10(32417/8112), 11(167511/38865), 12(869139/190081), 13(4574468/937194), 14(24139560/4660000). (The last q value for n=14 was extrapolated.) Thus the algorithm generated, for example, 167511 V_{11} vacancy clusters with only 38865 inequivalent ones.

In *Step 4*, the geometry optimization was done with a conjugated gradient method for each of the I_n structures. The geometry relaxation process typically required at least 50 steps. The most stable structures were determined by filling up the lowest one electron energy levels. In the case of degeneracy, we used the accidental order of the eigenvalues generated by the computer. We choose N = 216 for the diamond supercell with n up to 14. In Tables SI through SIII we present the genealogy of all V_n's with their respective formation energies. For $8 \leq n \leq 14$ the same information is given only for the ten lowest energy structures in Table SIV.

In *Step 5*, the relative stability of the *n*-vacancy clusters was expressed by the formation energy E_f^n:

$$E_f^n = E_{vac}^n - \frac{N-n}{N} E_{cryst}^N \qquad (4)$$

The formation energy per vacancy is $E_{fV}^n = E_f^n / n$. Here E_{vac}^n is the total energy of a supercell with (N - n) atoms and $E_{cryst}^N = E_{vac}^0$.

Step 6 refers to the choice of M_n. For small *n* the maximum value of M_n is (max(M_n). This number is limited (e.g. max(M_2)= max(M_3)=1) but max(M_n) rapidly raises with *n* to astronomical numbers. Up to n = 7, we included all possible vacancy clusters, for n > 7 we used the following parameters $M_7 = M_8 = M_9 = M_{10} = M_{11} = 5$ and $M_{12} = M_{13} = 7$. Table SV contains genealogical information on how the different structures can be generated from their "parents".

5. Results

We present the outcomes for each of the V_n vacancy clusters. Fig. 1 contains the atomic numbering, Fig. 2 and 3 show the most stable vacancy clusters, and Fig. 4 and 5 contain specific vacancy clusters used in the analysis or because of earlier discussions of these structures in the literature. Figs 2 –5 contain relaxed (columns 5 and 6) and unrelaxed (columns 2 and 3) geometries of the respective V_n's. Column 4 shows the removed atoms which are also indicated in columns 2 and 6 in addition to the surface atoms of each V_n. Notation used in the earlier literature is adjacent to the symmetry labels of the relaxed structures in column 7. Column 1

contains the symmetry of the ideal unrelaxed structures. Figs 6-9 illustrate specific cases and their geometrical descriptors. Figures S1-S3 (see the Supporting Data Section) show the energy levels and symmetries of the dangling bond orbitals. In Table I, we collected characteristic distances obtained for the relaxed geometries. These are analyzed after the discussion of the specific diamond vacancy clusters with n=1 through 14. Further detailed analysis of the specific vacancy cluster energy levels and geometrical characteristics are given in the Supporting Data Section. For several vacancy clusters we confirm earlier assignments, while for some vacancy clusters a novel interpretation is offered based on the presented modeling.

V_1 vacancy

According to experimental and theoretical results[20-22, 29, 30] the neutral monovacancy in diamond has T_d symmetry (Figs 2 and 6). V_1 in Si undergoes a T_d to D_{2d} distortion.[19] Coulson and Kearsley[28] and later Yamaguchi[31] assumed that the electrons in the dangling orbitals surrounding the vacancy primarily determine the electronic properties. In our TB calculations, the HOMO was a triply degenerate non-bonding t_2 orbital containing two electrons, that is *sb*=4 and *s*=*s'*=3. In order to obtain a T_d symmetry relaxed structure in the conjugate gradient procedure we used a fractional occupation number of 2/3 in the HOMO (Fig. S1). In the relaxed structure, the four three-coordinated carbon atoms define the size of the tetrahedron-like void with a side of 2.61 (2.52) Å. The first neighbors of the vacancy atom experience an outward displacement of 0.044 Å while the second neighbors undergo a 0.024Å inward displacement. These values are similar but smaller than in previous work.[21] We obtained a formation energy of 7.538 eV for V_1. Local density calculations gave 7.2 eV formation energy on a supercell of 64

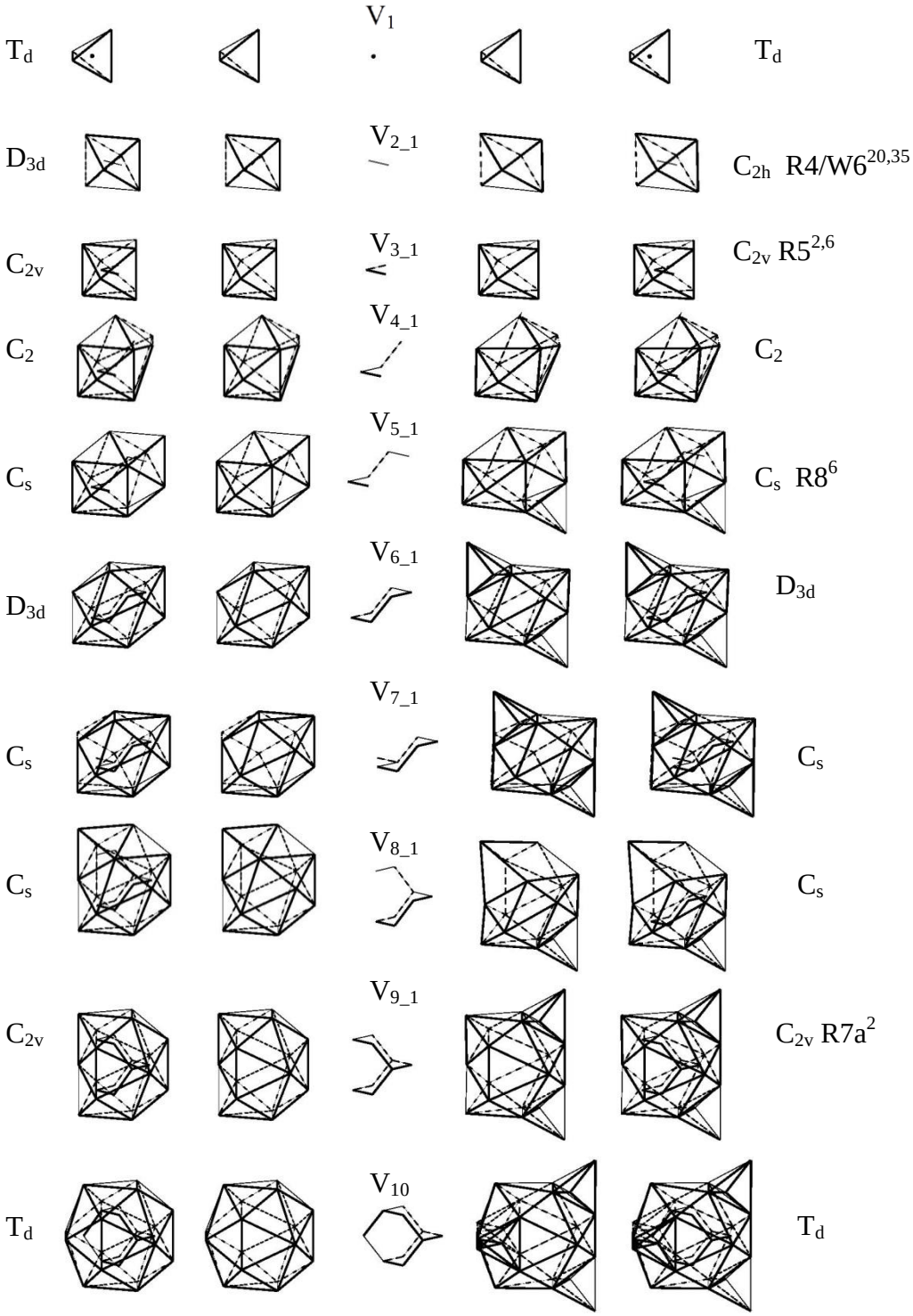

FIG. 2. Most stable V_n vacancy clusters in diamond for n=1 through n=10 as obtained by the presented algorithm and TBDFT energy calculations. The middle column represents the removed atoms constituting the cluster. Columns 2 and 3 are unrelaxed geometries, columns 5 and 6 are the relaxed geometries. Columns 2 and 6 contain the removed atoms, columns 3 and 5 do not.

atoms.[32] Without any constraint to the symmetry, we obtained 7.272 eV for the formation energy with a geometrical distortion to C_{2v} symmetry (Table SI).

V_2 vacancy

The removal of two neighboring atoms from the diamond structure yields a defect with D_{3d} symmetry[20, 33-35] (Figures 2, S1) that contains six dangling bonds (*sb*=6) and six electrons. Upon geometry relaxation, a Jahn-Teller distortion drives the structure to C_{2h} (Fig. S1). The two equilateral triangles formed by the dangling bond atoms around the three-fold axis changed to two isosceles triangles with the following distances: $r_1 = 2.50\,(2.52)$ Å, $r_2 = 2.63$ (2.52) Å, $r_3 = 2.63$ (2.52) Å (Fig. 7). Besides the changing of the symmetry we observe on average a small increase of the interatomic distances of the two triangles. The R4/W6 EPR center observed in irradiated diamond is attributed to the neutral charge state of the divacancy[20, 35]. EPR measurements at 80 K showed that it has S = 1 and C_{2h} symmetry.[20] There has been no explanation for the driving force for the distortion to C_{2h}. In our calculation we obtained the C_{2h} symmetry, but we assume the spin state of S = 0. In tight-binding calculations, assuming an S = 1 state and using partial occupation numbers for the HOMO of e_u symmetry, the final relaxed structure will have D_{3d} symmetry.

V_3 vacancy

The void of the V_3 vacancy has C_{2v} symmetry and *sb*=8 (the two terminal atoms have 3 dangling bonds and the center atom has 2) which are on the eight neighboring (or surface) atoms

of the void (Fig. 8, S1). During the relaxation, the relative position of these orbitals remain unchanged (s=s'=5).

The equilateral triangles composed by the surface atoms at the two terminal vacancy atoms changed to isosceles triangles as with the V_2 vacancy. The relaxed interatomic distances are the following: $r_1 = 2.49$ Å, (2.52) $r_2 = 2.61$ (2.52) Å, $r_3 = 2.61$. (2.52) The distance r_1 is perpendicular to the mirror plane containing the vacancy atoms (Fig. 2). The distance $r_4 = 2.49$ (2.52) is also perpendicular to this plane and the corresponding surface atoms have cut bonds with the middle atom of the vacancy cluster as illustrated in Fig. 8. In our most stable structure with S = 0 spin, the HOMO($426b_2$) – LUMO($427a_2$) energy difference is 0.24 (0.11) eV. Inclusion of electron correlation may show a triplet ground state when the gap is this small. EPR measurements on irradiated diamond attributed the R5 center to the neutral V_3 vacancy with S = 1 spin state.[2,6]

V_{3_is} vacancy

Here we describe a set of three isolated V_1 vacancies forming a special kind of three-atom vacancy with C_{3v} symmetry, the V_{3_is} (Fig. 4, S1), where the three vacancy atoms are in second neighbor position in the (111) plane. Their interatomic distance is 2.52 Å and they form an equilateral triangle. Relaxation in V_{3_is} produces what we call a "*tetrahedron of graphitization*", TOG. If we translate by r_{CC} the three vacancy atoms of V_{3_is} in the (111) direction we find three carbon atoms at these positions. These three carbons have a joint neighbor. During the relaxation process, this neighboring atom will move toward the plane of the vacancy atoms developing sp^2 hybridization. We use the notation r_a for the increased interatomic bond and r_b, r_c and r_d for the

other interatomic bonds of the moving atom in the tetrahedron. This displaced atom with its original four neighbors form the TOG with the elongation of the r_a bond and the simultaneous shortening of the adjacent bonds. The number of dangling bond states is increased by one due to the formation of the TOG. The corresponding new gap state is antibonding (π^*). TOG displays the smallest unit with traces of π-bonding and helps analyze more complex cases and it can be easily identified for in col. 5 and 6 in Fig. 4. This protrusion is a characteristic of the TOG that is apparent when comparing the diagrams in col. 5 and 6 with the unrelaxed structures in col. 2 and 3 in Figures 2 through 4. V_{3_is} is the smallest vacancy cluster for which such a protrusion occurs.

V_4 vacancy

V_{4_1} is chain-like and has C_2 symmetry (Fig. 2 and Table SI) and the ten hybridized dangling bonds are listed in Fig. S1. The corresponding energy level of the doubly occupied HOMO orbital $424a$ and the energy levels around it are defect states that are in the gap. The two equilateral surface triangles at the two ends of V_4 relaxed to $r_1 = 2.34(2.52)$ Å, $r_2 = 2.66(2.52)$ Å and $r_3 = 2.58(2.52)$ Å. The distance between the surface atoms near the two interior vacancy atoms is $r_4 = 2.30(2.52)$ Å.

EPR on irradiated diamond indicated a V_4 vacancy with C_{2v} and in the S = 1 state[2,6,36], labeled the O1 center. It has been associated with a $\langle 110 \rangle$ chain[6,36] with C_{2h} symmetry (V_{4_3} in Table SI and Fig. 4, S1) contradictory to the EPR finding[2] that indicated C_{2v}. In our calculation for the C_{2h} symmetry structure the HOMO orbital $424b_g$ is in the gap with other five surface orbitals (Fig. S1). The situation is the same before and after the relaxation. The

parameters for the two equilateral surface triangles at the two ends of the V_{4_3} vacancy are the following: $r_1 = 2.54(2.52)$ Å, $r_2 = 2.57(2.52)$ Å and $r_3 = 2.57(2.52)$ Å. The distance between the surface atoms near to the two interior vacancy atoms is $r_4 = 2.37(2.52)$ Å as defined in Fig. 8. In a connected chain of vacancies each has two dangling bonds, except for the ends which have three each. These trends are different from those found in earlier calculations where the dangling bonds reconstruct in pairs leaving two dangling bonds, one at each end of the chain.[6,36] Note that both V_{4_3} and V_{4_2} are significantly less stable than V_{4_1}.

V_5 vacancy

The most stable V_5 void, the V_{5_1}, has C_s symmetry (Figs 2 and S1). The energy level of the doubly occupied HOMO orbital $422a'$ is in the valence band and the energy levels above it are in the gap. After the relaxation, the void determined by the atoms having at least one dangling bond can be seen in Fig. 2. The most interesting phenomenon of this void is the appearance of a tetrahedron of graphitization (TOG), which appears as a protrusion in col. 5 and 6 in Fig. 2. The parameters of the TOG are $r_a = 1.99(1.54)$, $r_b = 1.55(1.54)$, $r_c = r_d = 1.47(1.54)$ Å. V_{5_1} has similar to V_{3_is} three atoms which produced the simplest TOG. Baker attributed this V_{5_1} structure to the EPR detected R8 center[6] although its measured symmetry is C_{2v}. The R6 EPR center has been attributed to the V_{5_6} chain lying in the (110) plane (Table SI and Fig. 4, S1).[2,6] According to our calculation, this structure is the penultimate in the stability order of V_5 voids with C_{2v} symmetry as in the EPR experiment.

V_6 vacancy

The most stable V_6 vacancy cluster has the cyclohexane-like structure with D_{3d} symmetry. As each vacancy atom has two cut bonds, the number of dangling bonds and surface atoms is twelve (*sb*=12) (V_{6_1} in Fig. 2). After the relaxation, we obtained two TOGs as the cyclohexane-like structure of vacancy atoms can be imagined as a pair of connected V_{3_is} vacancies as can be seen in Fig. 2. Col. 5 and 6 for $V_{6\_1\ in}$. These two protrusions indicate of two TOGs. The parameters of the TOGs are $r_a = 1.99(1.54)$, $r_b = r_c = r_d = 1.59(1.54)$ Å. At the same time the interatomic distance is lengthened significantly: $r_4 = 2.15(2.52)$ Å (Fig. 9). The extra stability of the carbon V_6 cyclohexane-like vacancy is due to the formation of two TOGs not seen in the Si case.

The number of inequivalent V_6 vacancy clusters is 24 and the least stable, V_{6_24}, corresponds to the chain lying in the (110) plane. This structure is usually attributed to the R10 EPR center[2,6] but it has C_{2h} symmetry contrary to the C_{2v} symmetry obtained in EPR experiment. (Table SII and Fig. 4). The dangling bond states in the gap are shown in Fig. S2. The parameters for the two equilateral surface triangles at the two ends of the V_{6_24} vacancy are the following: $r_1 = 2.38(2.52)$ Å, $r_2 = r_3 = 2.58(2.52)$ Å. The distance between the surface atoms of the other two middle point vacancy atoms from the side of the void are $r_4 = 2.15(2.52)$ Å, $r_4 = 2.12(2.52)$ Å.

V_7 vacancy

The most stable V_7 void has C_s symmetry (V_{7_1} in Table SIII and Figs 2 and S2). The vacancy cluster contains the previous V_6 cyclohexane-like structure plus an atom in equatorial position. After the relaxation we obtained the two TOGs, just as for V_{6_1} (Fig. 2.).

In the stability order the next V_7 void is the V_{7_2}, constructed from the V_6 cyclohexane-like structure plus an atom in axial position (Table SIII and Fig. 5, S2). This was assumed to be the most stable V_7 vacancy cluster in previous calculations.[25] This defect also has C_s symmetry. Baker attributed the V_{7_6} structure (C_2) to the EPR active R7a center[6] although its measured symmetry is C_{2v} (Table SIII, Fig. 5, S2). The number of inequivalent V_7 vacancy clusters is 88 and the V_{7_77}, corresponds to the chain lying in the (110) plane. This structure has been attributed to the R11 EPR center[2,6] . It has C_{2v} symmetry as it is expected from EPR experiment (Table SIII and Fig. 4, S2).

V_8 vacancy

The most stable V_8 void, the V_{8_1}, has C_s symmetry (Table SIII and Fig. 2, S2). After relaxation, the orbital $426a'$ has a small weight in the vicinity of the vacancy cluster and came from the conduction band. The doubly occupied HOMO orbital $416a''$ is in the valence band. Here we obtained one TOG (Fig. 2.). Baker[6] suggested the V_{8_*} structure of Fig. 5 as a relatively stable structure as it is a closed ring. (* indicates that our algorithm did not generate this structure). We obtained E_{fV}^{8} = 3.2476 eV for this structure, slightly less stable than the 6th most stable we generated. Its relaxed structure does not have TOG. Although V_{7_6} is a parent structure

Table I. Special distances (in Å) between surface atoms of selected vacancy clusters discussed in the paper. For the notation see Figures 6, 7, 8, and 9 and the text.

	r_1	r_2	r_3	r_4				r_a	r_b	r_c	r_d
V_{2_1}	2.50	2.63	2.63								
V_{3_1}	2.49	2.61	2.61	2.49							
V_{3_is}								1.93	1.46	1.46	1.46
V_{4_1}	2.34	2.66	2.58	2.30							
V_{5_1}	2.48	2.52	2.54	2.25	2.23			1.99	1.55	1.47	1.47
V_{6_1}				2.15				1.99	1.59	1.59	1.59
V_{7_1}	2.64	2.46	2.46	2.13	2.18	2.15		1.86	1.53	1.59	1.59
								1.99	1.59	1.58	1.58
V_{8_1}	2.81	3.15	3.15	2.19	2.12	2.01		1.98	1.60	1.58	1.58
				2.16							
V_{9_1}				2.09	2.13	2.44		1.97	1.58	1.58	1.58
V_{10}			2.10				1.97	1.58	1.58	1.58	
V_{11_1}				2.09	2.10			1.97	1.58	1.58	1.58
								1.97	1.57	1.57	1.58
V_{12_1}				2.07	2.08	2.09		1.97	1.58	1.57	1.57
								1.96	1.58	1.58	1.57
V_{13_1}				2.83	2.02	2.16	2.13	2.12	1.57	1.57	1.43
				2.15				1.96	1.59	1.59	1.60
								1.90	1.60	1.59	1.54
V_{14_1}				2.12				2.08	1.45	1.57	1.57
V_{4_2}	2.31	2.52	2.52								
V_{4_3}	2.54	2.57	2.57	2.37							
V_{5_6}	2.49	2.55	2.55	2.34	2.17						
V_{6_24}	2.38	2.58	2.58	2.15	2.12						
V_{7_77}	2.53	2.58	2.58	2.17	2.14	2.11					
V_{8_ch}	2.39	2.66	2.66	2.17	2.12	2.11					
V_{7_2}	2.29	2.70	2.70	2.13	2.38	2.17		1.98	1.59	1.58	1.58
V_{7_6}	2.09	2.40	2.51	2.26	3.07	2.18					
V_{7_10}	2.44	2.69	2.53	2.59	2.24	2.66					
V_{8_*}				2.61	2.22						
V_{11_*}				2.02	2.83	2.21	2.17	1.96	1.59	1.59	1.60
				2.59	2.56						
V_{13_*}				3.07	2.27	2.51	1.94				

V_{8_ch} stands for V_{8_chain}.

for V_{8_*}, our algorithm did not produce it as we used the $M_7 = 5$ parameter.

In Fig. 4 and S3 we can see the V_{8_chain} structure of the chain lying in the (110) plane. This structure has been attributed to the KUL11 EPR center[2,6] although it has C_{2h} symmetry contrary to the EPR evidence that supports C_{2v}. This structure can not be found in the list of Table SIV for V_8 as it has relatively high E_{fV}^{8} =3.75eV. During the relaxation process, we obtained an extra energy level in the gap.

V_9 vacancy

The most stable V_9 void has C_{2v} symmetry (V_{9_1} in Table SIII and Figs. 2, S3) and its relaxed structure has two TOGs. During the relaxation the number of dangling bond states increased by two. The parameters of the TOG are $r_a = 1.97(1.54)$, $r_b = 1.58(1.54)$, $r_c = r_d = 1.58(1.54)$ Å. The distances between the surface atoms close to the three different kinds of interior atoms (starting from the symmetry axis) are: $r_4 = 2.09(2.52)$, $r_4 = 2.13(2.52)$, $r_4 = 2.44(2.52)$ Å. This V_{9_1} void was attributed to the R7a EPR center.[2]

V_{10} vacancy

V_{10_1} (T_d) is particularly stable. It has four TOGs in the relaxed structure (Table SIII and Figs 2, S3).

V_{11} vacancy

The most stable V_{11_1} void (C_{3v}) has four TOGs in the relaxed structure. (Table SIV and Figs 2, S3). One TOG has the same axis of rotation as the void and the other three TOGs can be transformed by the three-fold axis. Iakoubovskii and A. Stesmans[2] attributed the V_{11_*} void of Fig. 5 to the R7 EPR center. Although this structure has one TOG, its formation energy per vacancy is 2.9021 eV being less stable than our 10 most stable V_{11} structures.

V_{13} vacancy

The most stable V_{13} void has C_s symmetry and 1 + 1 + 2 = 4 TOGs in the relaxed structure (V_{13_1} in Table SIV and Fig. 2, S2). However, Iakoubovskii and A. Stesmans[2] and Baker[6] attributed the V_{13_*} void of Fig. 5 to the R8 EPR center. It has C_{2v} symmetry and its formation energy per vacancy (2.93eV) is higher than the formation energies of the V_{13} structures listed in Table SIV.

V_{14} vacancy

Especially stable is the lowest energy V_{14_1} (D_{3d}) with six equivalent TOGs in the relaxed structure (Table SIV and Fig. 2, S3).

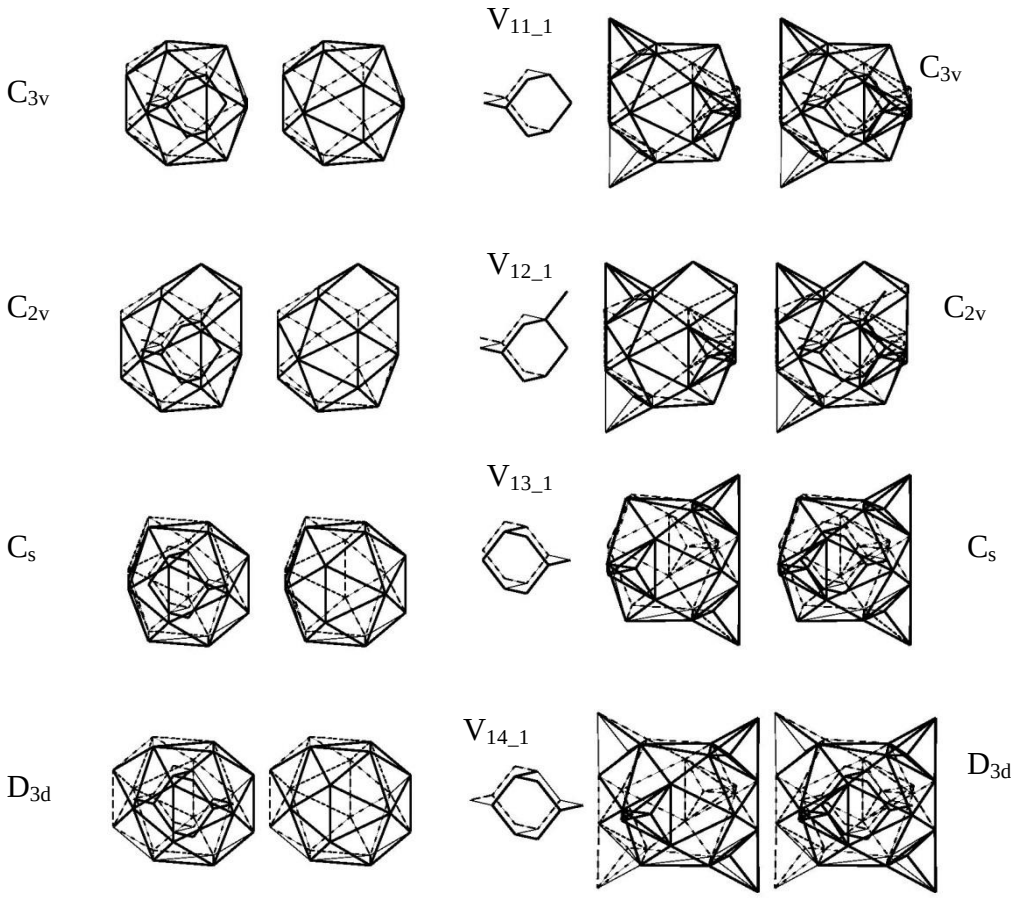

FIG. 3. Most stable V_n vacancy clusters in diamond for n=11 through n=14 as obtained by the presented algorithm and TBDFT energy calculations. The seven columns are the same as in Fig. 2.

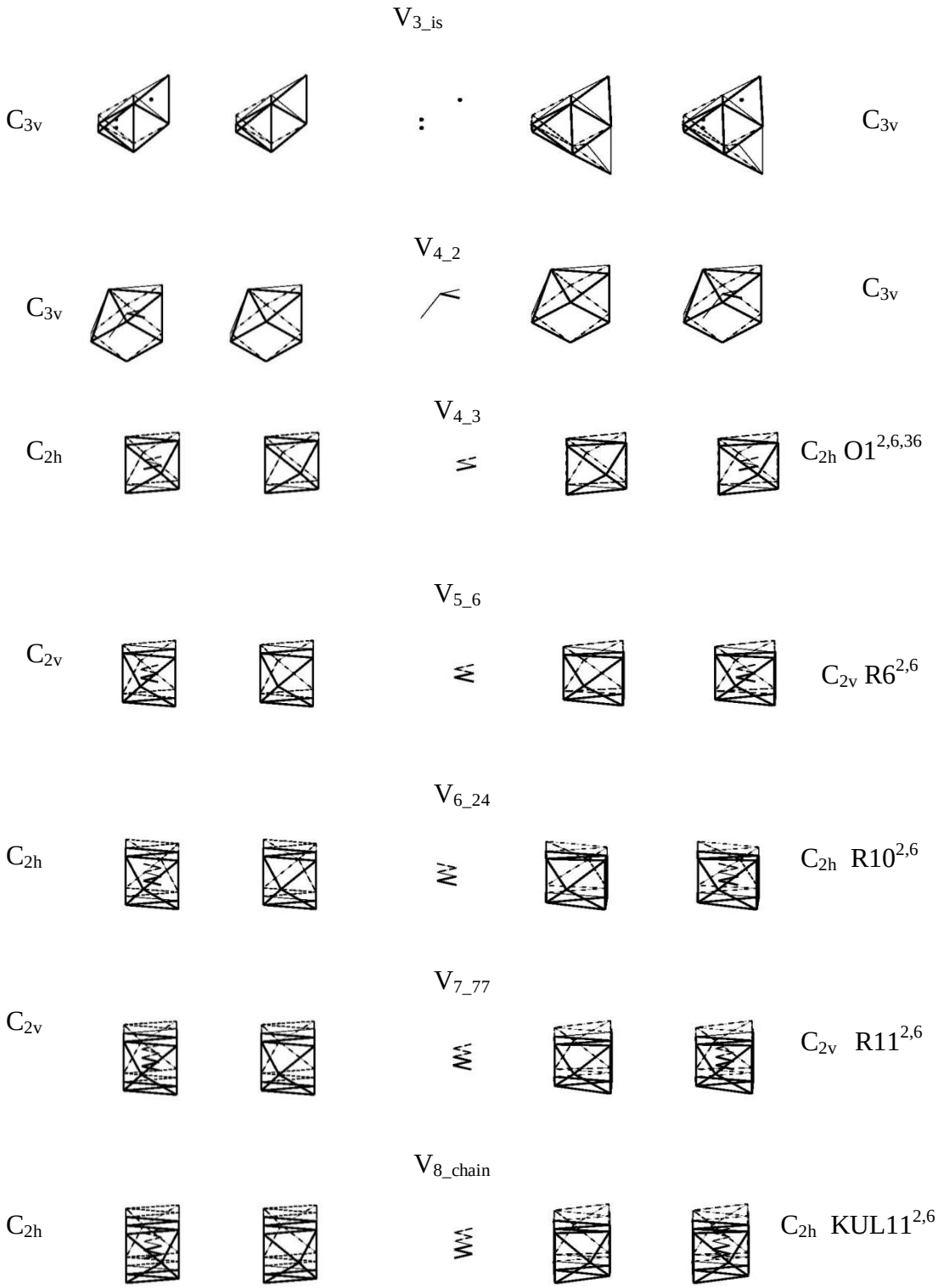

FIG. 4. Selected chain-like V_n vacancy clusters in diamond for n=3 through n=8. The seven columns are the same as in Fig. 2.

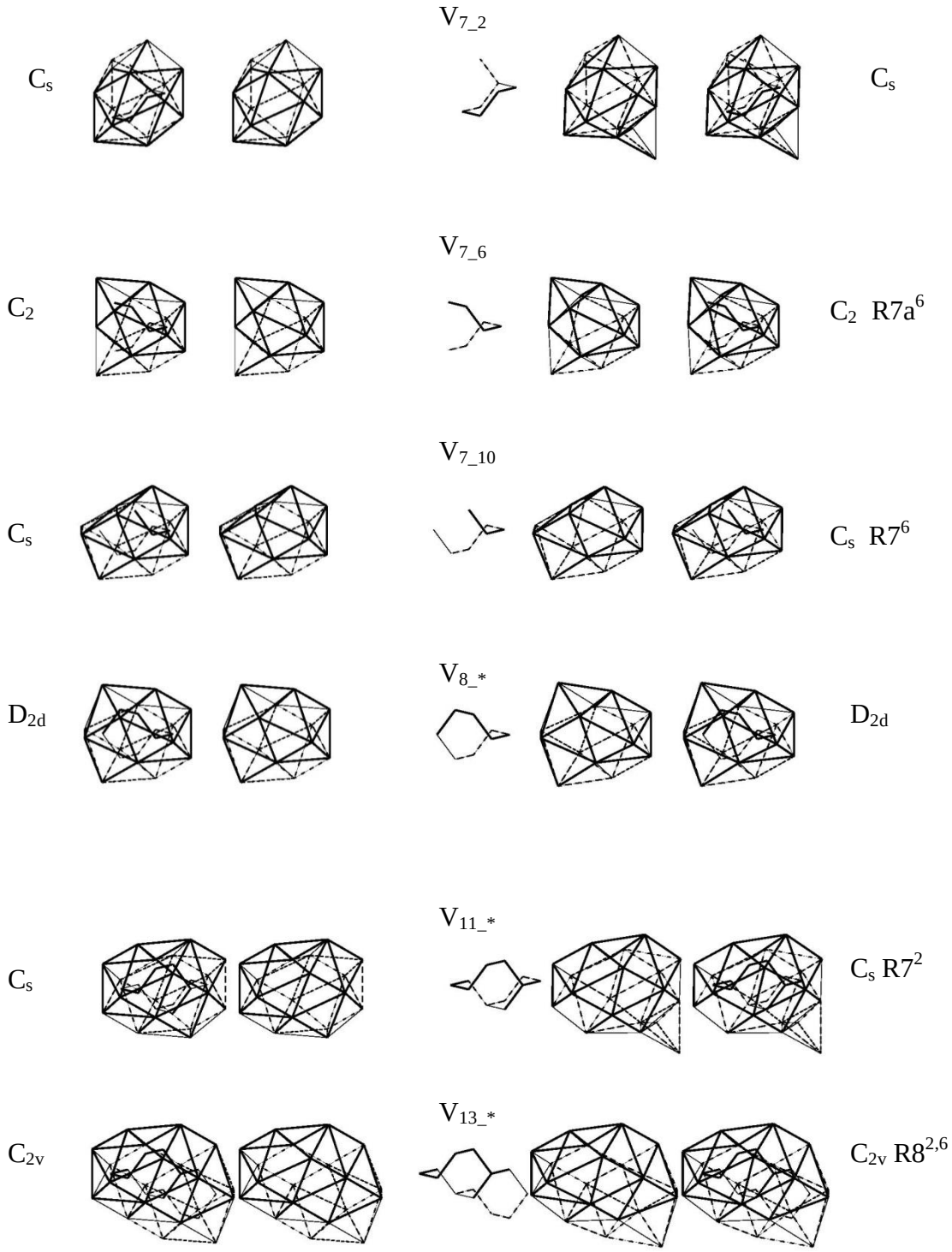

FIG. 5 Selected V_n vacancy clusters in diamond for n=7 through n=13. The seven columns are the same as in Fig. 2.

Trends in vacancy cluster geometries

We have noticed trends among the distances marked by the identical notation (Table I). These regularities point to the possibility of rich chemistry and physics of vacancy clusters given their unusual CC contacts. Most remarkable are the CC contacts that appear to represent a new kind of bonding in the tetrahedra of graphitization.

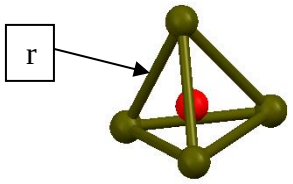

FIG. 6. The nearest neighbors to the vacancy cluster V_1 (removed atom in red) site maintain T_d symmetry with r = 2.61 when the HOMO t_2 orbitals all equally occupied by 2/3 electrons.

The parameters of the TOG are in the ranges $r_a = 2.01 \pm 0.11$ Å, $r_b = 1.525 \pm 0.075$ Å, $r_c = 1.525 \pm 0.075$ Å and $r_d = 1.525 \pm 0.075$ Å. Clearly, the first neighbor contact distances of 2.01 ± 0.11 Å found in the TOGs is highly unusual and not found as an equilibrium carbon-carbon bond distance in any of the over 400,000 organic molecular structures in the CSD.[40] As pointed out above many of the contact distances are stabilized only by the surrounding dangling orbitals of the carbon network and the multicenter bonding that they provide.

Some second neighbor distances also show trends that are summarized below. In the most stable vacancy clusters for example only the vacancies V_1, V_{2_1}, V_{3_1}, V_{4_1}, V_{5_1}, V_{7_1} and

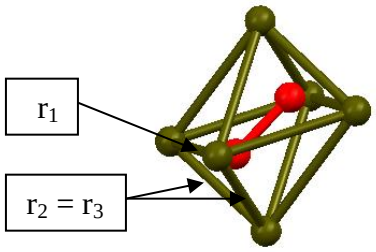

FIG. 7. The relaxed geometry surrounding V_{2_1} (removed atoms in red). Labeled distances refer to the separations between the three neighbors to the vacancy terminus.

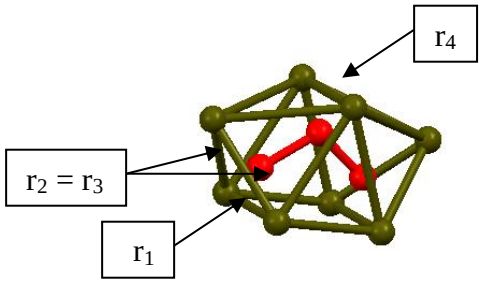

FIG. 8. The relaxed geometry surrounding V_{3_1} (removed atoms in red). As with the V_{2_1}, r_1, r_2, and r_3 denote the separations between the three neighbors surrounding the termini. r_4 is the separation between the two neighbors of the middle vacant atom.

V_{8_1} have vacancy atoms with at least three cut bonds. The chain-like structures V_{2_1}, V_{3_1}, V_{4_3}, V_{5_6}, V_{7_77} belong to the family defined by the following characteristics: r_1

$= 2.515 \pm 0.025$ Å, r_2=$r_3 = 2.59 \pm 0.04$ Å. For V_{6_24} we obtained a slightly smaller r_1, but the r_2=r_3 value is in the same range. The exception of V_{8_chain} can be explained by the limited size of the supercell. In other structures there are special relative positions between the surface atoms of the voids leading to r_1, r_2 and r_3 distances outside of the abovementioned ranges. Similar remarks can be made for the r_4 distances as well. There are some exceptions due to insufficient supercell size, e.g. for V_{13_*}. Most of them are in the range $r_4 = 2.1 \pm 0.09$ Å, which makes these contacts approach values where multicenter bonding contributes to the stability of the structure.

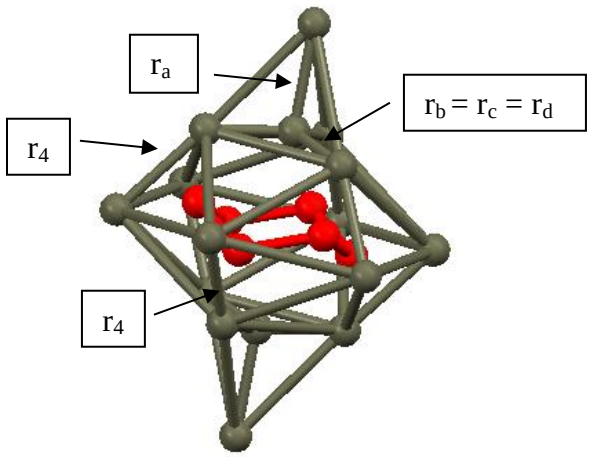

FIG. 9. The relaxed structure surrounding the V_{6_1} (removed atoms in red). There are six equivalent r_4 distances (two are shown) corresponding to the interatomic separation between the axial and equatorial neighbors to the vacancy. r_a, r_b, r_c, r_d are the four distances stemming from the central atom in the tetrahedron of graphitization (TOG); only one of two equivalent sets are shown.

6. Concluding remarks

We have obtained the structures and properties of V_n multi-vacancy voids in diamond in the range of n=1 through 14. Most of these structures are novel and are described for the first time. Several of these voids are different from the corresponding multi-vacancy voids in silicon. We have traced these differences to the tendency of carbon to form π-bonds in the "tetrahedron of graphitization" (TOG) allowing the adjacent dangling bonds to turn towards each other and "heal."

The tendency to form π-bonds is a sign of a certain degree of *graphitization* around some of these voids, which in turn removes the non-bonding dangling orbitals from the middle of the gap lending both stability and, perhaps, reduced reactivity to these voids. This was a surprising result and we speculate that if this tendency is maintained for larger voids, the characteristics of such voids and pores for chemical storage may be favorable. The tendency of local "graphitization" around parts of the vacancy cluster appears already at an unexpectedly small size. We have identified a noncontiguous vacancy cluster of three monovacancies, $V_{3\text{-isol}}$. We found that this motif goes hand in hand with similar local graphitization tendencies in all vacancy clusters studied. Each tetrahedron of graphitization (TOG) produced an extra energy level in the gap. It is possible, even likely, that in large vacancy clusters such tendencies for graphitization on the atomic scale may lead to the formation of larger graphitic regions significantly affecting their properties as gas storage or electrode materials. The multi-vacancy voids studied in this paper were generated by a novel generational algorithm that proceeds to spawn generation n+1 from the list of the most stable structures in generation n. A key point in the algorithm is to determine and eliminate equivalent structures, which is done by comparing

the eigenvalues of a modified adjacency matrix of the contiguous atoms of the vacancy. This novel method permits a significant reduction of the number of inequivalent vacancy clusters to consider for any given n. This allowed us to describe all possible vacancy clusters up to V_7 for the first time. We also obtained the optimized geometries by tight binding DFT for all possible vacancy clusters up to V_7.

An advantageous feature of the generational algorithm is that it is fully reproducible because five integers contain all the information necessary to define a member of the new generation. Using this algorithm combined with tight binding DFT, we determined the most stable contiguous vacancy clusters for V_8 through V_{14}. For the most stable structures we identified the surface states and their symmetries. These can be used in devising more sophisticated calculations for determining the measured electronic transitions.

We also investigated structures suggested by other groups[2,6,24] based on EPR experiments for vacancy clusters with n=2, 3, 4, 5, 7, 9, and 11. Most of these structures were found to be higher in energy than the most stable vacancy clusters generated by our algorithm, in some cases significantly higher. Note that our calculations, being of the TB kind, is limited to spin=0 states. There is controversy in the literature concerning the identities of these structures (see Figures 2-5). It seems that if the identification of these structures with EPR signals is correct in the literature, then the more stable structures obtained in this work should also exist in the S=0 state. For possible existing structures see, for example, those highly stable structures in Figures 2 and 3 which are not are visible by EPR.

One of the interesting features of this study is the high frequency of neighboring C-C distances in the unusual range of 1.8 to 2.6 Å. There are no molecular examples of such distances

either as intramolecular bond distances or intermolecular contact distances in the Cambridge Structural Database (CSD), as most C-C contacts are found below 1.6 Å and above 3.2 Å. It is clear that the environment surrounding vacancies in diamond is entirely unique and different from other carbon systems owing to the presence of dangling radicals whose relaxation is hindered due to the scaffold of the surrounding covalent network. Whether these unusual contacts have all the features of ordinary chemical bonds remains to be seen. They appear to be more variable than ordinary electron pair bonds, but variability is not unusual for multielectron multicenter delocalized bonding.

Acknowledgement

Support from the DOE (Grants No. DE-FG02-07ER46472 and DE-FG01-05ER05-01) is gratefully acknowledged.

Supporting data

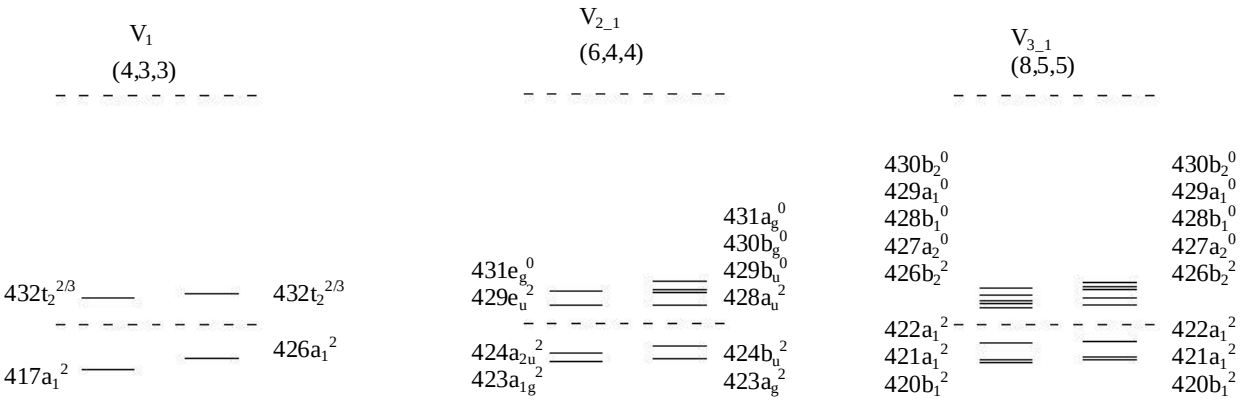

FIG. S1a. Electronic structure of vacancy clusters. Under the name of vacancy cluster V_{n_k} the notation (sb, s, s') contains the number of severed bonds sb, and the s, s' numbers of dangling bond orbitals before and after the relaxation. On the left are the dangling bond energy levels before relaxation, on the right after the relaxation. Symmetries and occupation numbers are also indicated. The symbols for the gap states and the valence states are separated a line break. The dashed lines correspond to the upper (LUMO=2.27eV) and lower (HOMO=-5.17eV) edges of the gap in the bulk material.

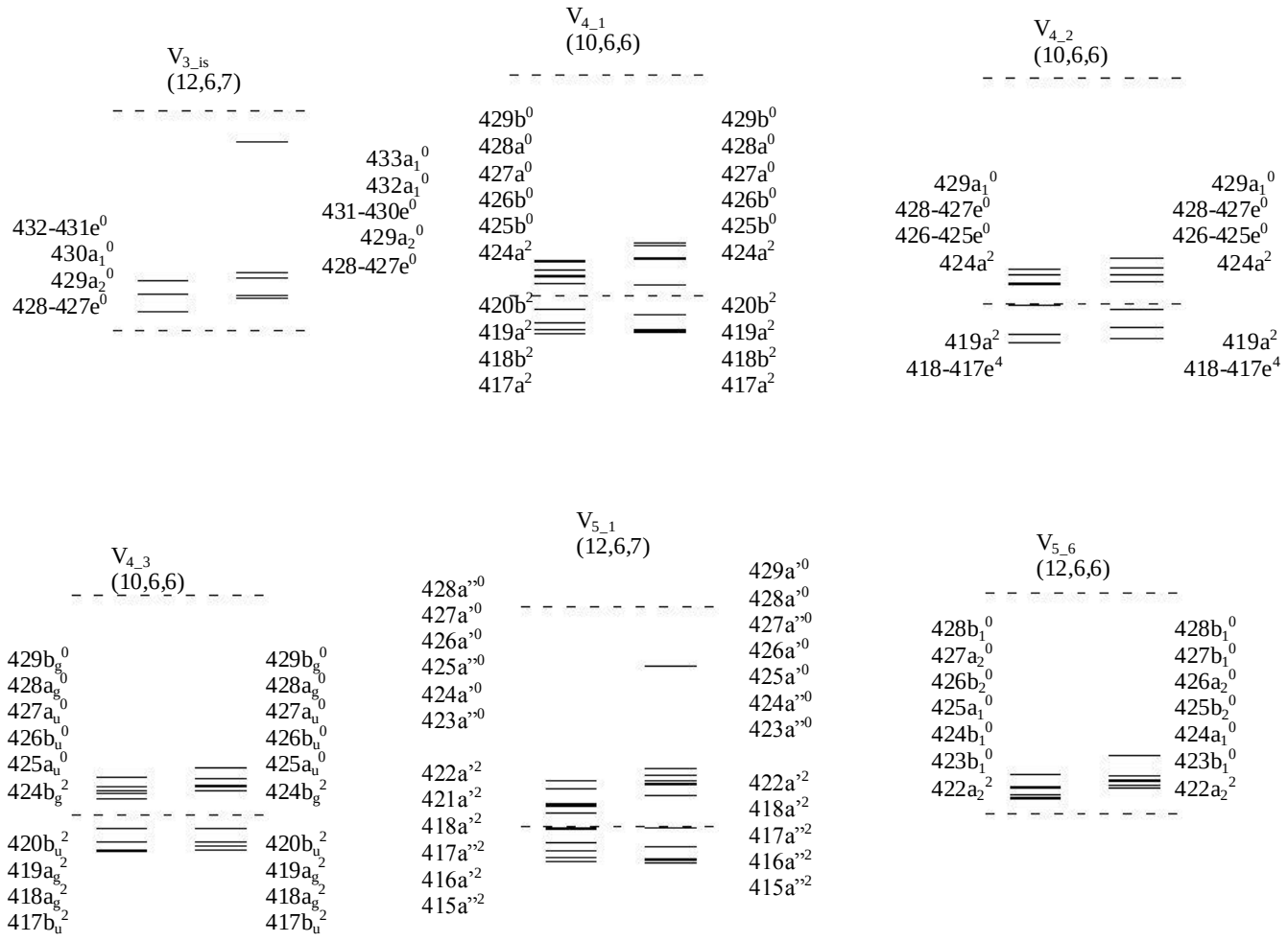

FIG. S1b. Electronic structure of vacancy clusters. Under the name of vacancy cluster V_{n_k} the notation (sb, s, s') contains the number of severed bonds sb, and the s, s' numbers of dangling bond orbitals before and after the relaxation. On the left are the dangling bond energy levels before relaxation, on the right after the relaxation. Symmetries and occupation numbers are also indicated. The symbols for the gap states and the valence states are separated a line break. The dashed lines correspond to the upper (LUMO=2.27eV) and lower (HOMO=-5.17eV) edges of the gap in the bulk material.

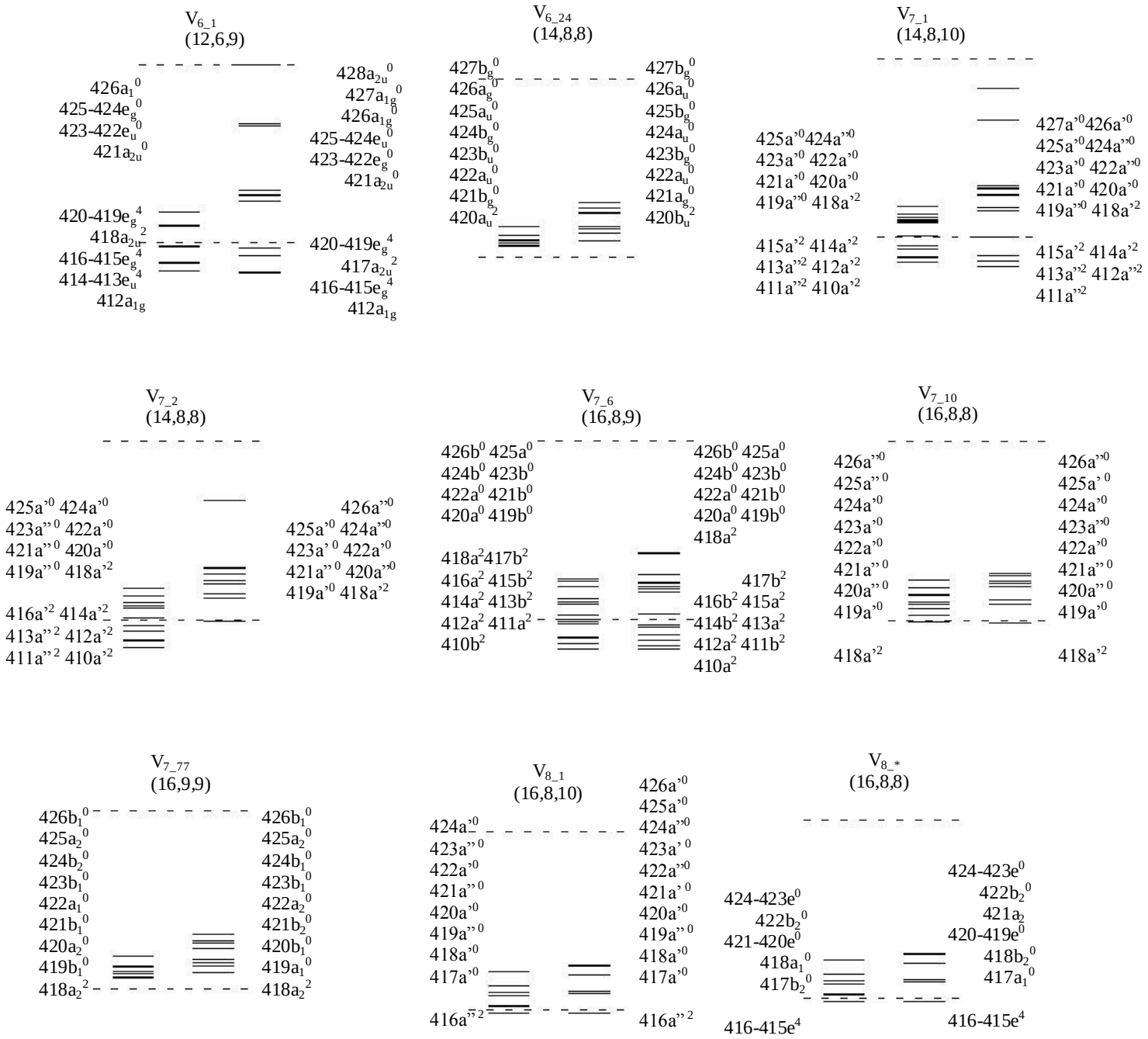

FIG. S2. Electronic structure of vacancy clusters. See the notation at Fig S1.

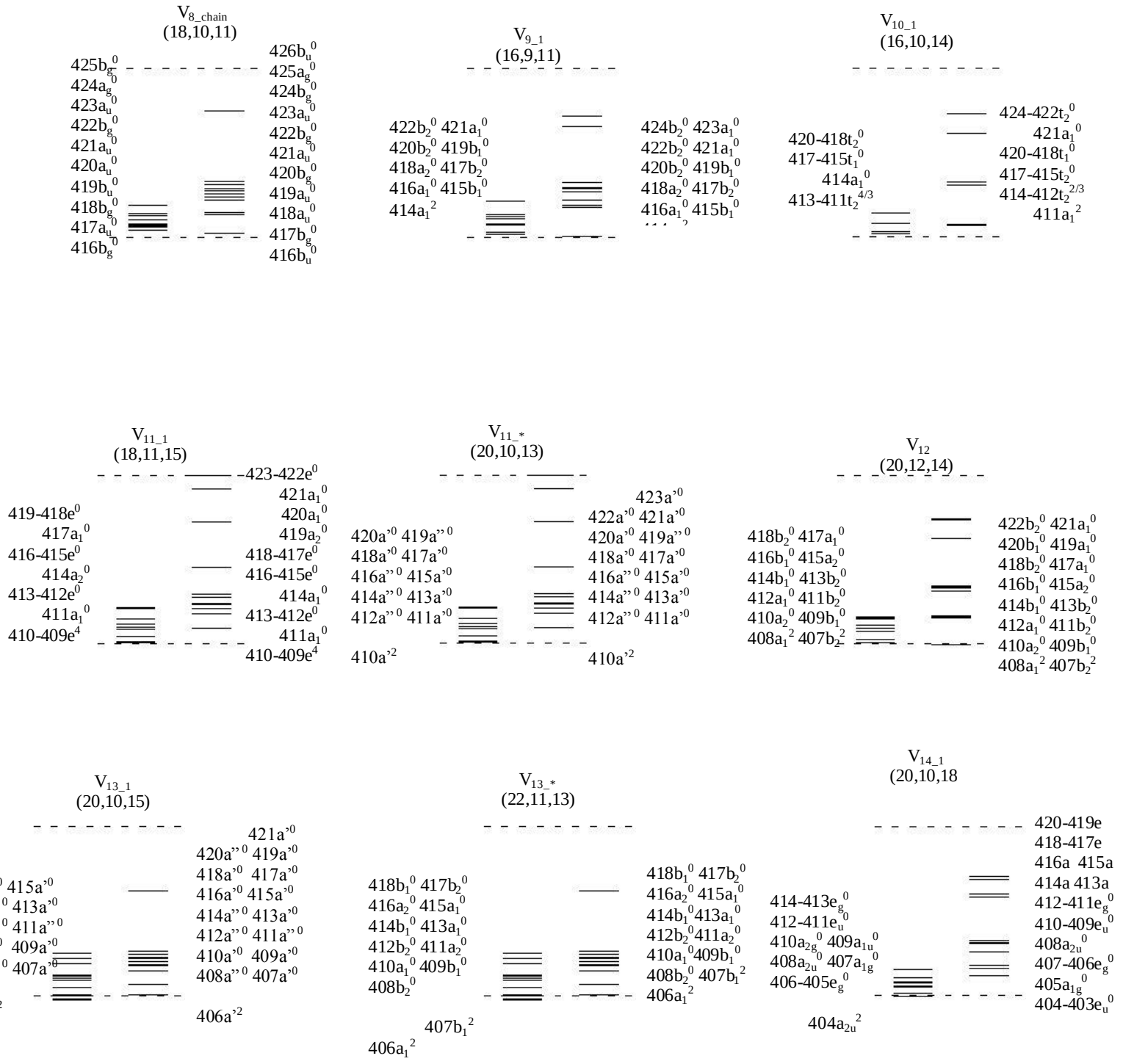

FIG. S3. Electronic structure of vacancy clusters. See the notation at Fig S1.

REFERENCES

[1]Y. Gogotsi, R.K. Dash, G. Yushin, T. Yildirim, G. Laudisio, J.E. Fischer, *J. Am. Chem. Soc.* **127**, (2005), p.16006.

[2]K. Iakoubovskii , A. Stesmans, *Phys. Stat. Sol. (a)* **201**, (2004), p.2509.

[3]U. Bangert, A.J. Harvey, R. Jones, C. J. Fall, A. T. Blumenau, R. Briddon, M. Schreck, F. Hörmann, *New J. Phys*. **6**, (2004), p.184.

[4]U. Bangert, A. J. Harvey, M. Schreck, F. Hörmann, *Ultramicroscopy* **104**, (2005), p. 46.

[5]K. Iakoubovskii, S. Dannefaert, A. Stesmans. *Phys. Rev. B* **71**, (2005), Art. nu.233201.

[6]J.M. Baker, Diam. and Rel. Mat. **16**, 216 (2007).

[7]L. S. Hounsome, R. Jones, P. M. Martineau, D. Fisher, M. J. Shaw, P. R. Briddon, S. Öberg, *Phys. Stat. Sol. (c)* **4**, (2007), p.2950.

[8]R. Jones, L. S. Hounsome, N. Fujita, S. Öberg, P. R. Briddon, *Phys. Stat. Sol.* (a), **204**, (2007), p.3059.

[9]L. S. Hounsome, R. Jones, P. M. Martineau, D. Fisher, M. J. Shaw, P. R. Briddon, S. Öberg, *Phys. Rev. B* **73**, (2006), p.125203.

[10] N. Fujita, R. Jones, S. Öberg, P. R. Briddon A. T. *Diamond Rel. Mater*. **18**, (2009), p. 843.

[11]D. Porezag, Th. Frauenheim, Th. Köhler, G. Seifert, R. Kaschner, *Phys. Rev. B* **51**, (1995), p.12947.

[12]R. Q. Hood, P. R. C. Kent, R. J. Needs, P. R. Briddon, *Phys. Rev. Lett.* **91**, (2003), p. 76403.

[13]Y.-H. Lee, J.W. Corbett, *Phys. Rev. B* **8**, (1973), p. 2810.

[14]D.J. Chadi, K.J. Chang, *Phys. Rev. B* **38**, (1988), p. 1523.

[15]C.Z. Wang, C.T. Chan, K.M. Ho, *Phys. Rev. Lett.* **66**, 189 (1991).

[16]J.L. Hastings, S.K. Estreicher, P.A. Fedders, *Phys. Rev. B* **56**, (1997), p.10215.

[17]A. Bongiorno, L. Colombo, T. D. De la Rubia, *Europhys. Lett*. **43**, (1998), p. 695.

[18]T. Akiyama, A. Oshiyama, O. Sugino, *J. Phys. Soc. of Jap.* **67**, (1998), p. 4110.

[19]T.E.M. Staab, A. Sieck, M. Haugk, M.J. Puska, Th. Frauenheim, H.S. Leipner, *Phys. Rev. B* **65**, (2002), 115210.

[20]D.J. Twitchen, M.E. Newton, J.M. Baker, T.R. Antony, W.F. Banholzer, *Phys. Rev. B* **59**, (1999), p.12900.

[21]D.P. Joubert, L. Li, J.E. Lowther, *Solid State Commun.* **100**, (1996), p.561.

[22]S.J. Breuer, P.R. Briddon, *Phys. Rev. B* **51**, (1995), p. 6984.

[23]C.A.J. Ammerlaan, in. *Semiconductors, Impurities, Defects in Group IV Elements, III-V Compounds*, edited by O. Madelung and M. Schultz (Springer, Berlin, 1990).

[24]J. N. Lomer, A.M.A. Wild, *Radiat. Effects* **17**, (1973), p. 37.

[25]L.S. Hounsome, R. Jones, P.M. Martineau, M.J. Shaw, P.R. Briddon, S. Öberg, A.T. Blumenau, N. Fujita, *Phys. Stat. Sol. (a)* **202**, (2005), p. 2182.

[26]R. Jones et al., in *Special Defects in Semiconducting Materials, Solid State Phenomena,* Ed. R. P. Agarwala, Vol. 71. pp 173. (Scietech Publications, Zuerich-Uetikon, Switzerland, 2000).

[27]A. Blumenau, R. Jones, T. Frauenheim, B. Willems, O. I. Lebedev, G. van Tendeloo, *Phys. Rev. B* **68**, (2003), 014115.

[28]C.A.Coulson and M.J. Kearsley, *Proc. Roy. Soc., Ser. A* **241**, (1957), p.433.

[29]A. J. Mainwood, J. Phys. C: *Solid State Phys*. **11**, (1978), p.2703.

[30]G.D. Watkins, R.P. Messmer, *Phys. Rev. Lett.,* **32**, (1975), p.1244.

[31]T. Yamaguchi, *J. Phys. Soc. Jap*. **17**, (1962), p.1359.

[32]J. Bernholc, A. Antonelli, T.M. Del Sole, Y. Bar-Yam, S.T. Pantelides, *Phys. Rev. Lett*. **61**, (1988), p. 2689.

[33]G. D.Watkins, J.W. Corbett, *Phys. Rev*. **138**, (1965), p. A543.

[34]S. Öğüt, J. R. Chelikowsky, Phys. Rev. Lett. **83**, (1999), p. 3852.

[35]B.J. Coomer, A. Resende, J.P. Goss, R. Jones, S. Öberg, P.R. Briddon, *Physica* B **273-274**, (1999), p. 520.

[36]K. Iakoubovskii, A. Stesmans, *Phys. Rev. B* **66**, (2002), Art. nu.045406.

[37]K. Iakoubovskii , A. Stesmans, *J. Phys : Condens Matter* **14**, (2002), p. R467.

[38]A. M. Zaitsev, *Phys. Rev. B* **61**, (2000), p.12909.

[39]A. M. Zaitsev, *Optical Properties of Diamond: a Data Handbook* (Springer, Berlin, 2001).

[40]Cambridge Structural Database (CSD), http://www.ccdc.cam.ac.uk/products/csd/

CHAPTER 3

CHARACTERIZATION OF LARGE VACANCY CLUSTERS IN DIAMOND FROM A GENERATIONAL ALGORITHM USING TIGHT-BINDING DENSITY FUNCTIONAL THEORY*

Abstract

Point defects and pores in diamond affect its optical and electrical properties. We generated and evaluated a large number of vacancy V_n clusters representing nanosized voids in diamonds for n up to 65. Our generational algorithm spawns the new generation $n + 1$ from the list of the most stable structures in the previous generation n. With energy the only criterion, we generate a large structural diversity that allows their unbiased analysis. Since π–electron delocalization is important for carbon, we used quantum mechanical tight-binding density functional theory (TBDFT). Adamantane-like globular shapes are preferred for n up to ~22. Beginning around n~35, the most stable structures show overall oblate shapes with some irregularities. These novel structures have not been seen before because hitherto only highly regular structures were considered. We see local graphitization in these relaxed structures providing an atomistic justification for the widely used "slit pore" model. The preference for structures with minimum number of cut bonds diminishes as n increases. There are no particularly stable "magic" sizes for vacancy clusters larger than n = 22 indicating that these larger voids can easily incorporate small vacancies and vacancy clusters. Radial distribution analysis shows that unusual contact or bond distances in the 1.6 to 2.8 Å range appear in the

* Reproduced with permission from [Slepetz, B.; Laszlo, I.; Gogotsi, Y.; Hyde-Volpe, D.; Kertesz, M. *Phys. Chem. Chem. Phys.* **2010**, *12*, 14017-14022] Copyright [2010] RSC Publishing.

vicinity of the internal surfaces of the vacancy clusters. Extremely long C-C bonds emerge as a result of structural relaxation of the dangling bonds in the vicinity of the vacancy clusters that cannot be simply described by ordinary sp^2/sp^3 hybridization.

Introduction

Diamond-structured materials, including nanodiamonds[23], diamond-like carbon and irradiated diamond crystals, contain a large variety of vacancy cluster defects, some of which are well characterized, while others are difficult to identify at the atomic level.[24,25] We arrived at the problem of modeling large vacancy clusters from a different direction. Carbide derived carbons (CDC) display a dazzling variety of structures, including those with sp^3 bonding and controllable nanosized pores[26] with important practical implications as supercapacitors in the energy sector.[27] The problem poses interesting basic structural questions as well, because these carbon networks display unusual carbon-carbon bonding situations due to the various dangling bonds and their relaxations within a rigid carbon network. Compared to Si, much less effort has been devoted to vacancy clusters in diamond. Previous density functional theory (DFT) work included the discussion of small relaxed vacancy clusters[28] and the systematic modeling of V_1 to V_{14} multi-vacancy clusters (chains, clusters and discs) in diamond[29] with the AIMPRO and DFTB codes.[30] The same group also investigated a large globular vacancy cluster (V_{71}) that may explain the brown coloration of diamond.[31] In our own preceding work, we have applied tight-binding density functional theory (TBDFT)[32] in combination with our genearational algorithm to study vacancy clusters–V_n with n up to 14–without imposing any shape constraint.[33] The present work extends these investigations to n = 65. Given the large number of essentially amorphous

structures obtained in this modelling, we focus on trends and general structural information. Given the structural diversity maintained in our algorithm together with the large sizes of the vacancy clusters, novel trends emerge, which we describe and interpret in this paper. We need to emphasize that given the lack of information on structures of large vacancy clusters, it is imperative that any realistic modelling include a large diversity of structures not limiting them to symmetrical, disk-like, adamantane-like or other special structures.

The choice of the methodology for obtaining optimized structures needs to be based on energetics that includes the important electronic effects, such as π-conjugation, delocalization, and aromaticity, which are essential for understanding the relative stabilities of carbon networks[34] especially in a case like the present problem where the comparison of different hybridizations is essential. Also, as pointed out by Irle et al.,[34] these effects are absent in the popular many-body bond-order potentials.[35,36] While full ab initio DFT calculations would be preferred,[28,29,30,31,37] given the large number of energetically competitive structures, the simplified TBDFT is used here. Similar TBDFT has been used recently in combination of molecular dynamics to model the nucleation of diamond under high pressure.[38] For structures in which delocalization of π-electrons over several sp^2 –like centers is important, one must use quantum mechanical methods that automatically include these effects. Given the large numbers of structures emanating in the modelling of large vacancy clusters without structural assumptions, the obvious choice of a currently viable and economical methodology is TBDFT.

Methods

As described in ref. 33, our generational *algorithm* spawns the new generation $n + 1$ from the list of the most stable structures in the previous generation n, starting from a monovacancy V_1. Energy is evaluated by full geometry optimization using the tight-binding density functional theory (TBDFT) energy on a 216 carbon site supercell ($N = 216$) with n vacant atoms using the Porezag et al. parametrization.[32] Note that this level of theory is appropriate for modeling diamond, graphite, amorphous carbon and the transitions among them.[32,33] We use periodic boundary conditions (PBC), with only the Γ-point representing k-space integrals. The dimensions of the supercell are kept constant.

Equivalent starting structures are eliminated by evaluating the eigenvalues of a modified adjacency matrix.[33] Only the M_n lowest energy structures in the n-th generation are used to spawn the members of the $n+1^{st}$ generation, which is done by adding one more vacant atom to all possible surface sites of the previously generated stable vacancy clusters. To avoid dealing with an astronomical number of structures, we kept $M_n = 7$ for $n \geq 14$ starting from the results of ref. 33 for n up to 14. Typically 300-500 structures were thus generated for each n, which were then minimized by energy. M_n of these were kept and used to spawn the new generation up to $n = 65$ resulting in the full geometry optimization of approximately 20,000 structures.

An important consequence of keeping several members of each generation is that the "winner" in each generation may not be the parent of the "winner" in the next. This aspect is the strength of the presented algorithm that maintains structural diversity from n to $n+1$. Due to the limitation on the supercell size, n values above ~50 correspond to vacancy clusters that interact with those in the neighboring supercell. Therefore, our results become more qualitative

approaching $n \sim 50$. But even these large n cases representing interacting vacancy clusters can give insights into the structures obtained by high-temperature chlorination of carbides.[27] Namely, in these structures, metals and metalloids are removed as chlorides, leaving behind a newly formed carbon with up to 80% open pore volume.[26] In what follows, we analyze the most stable of these for each n. It appears that keeping $M_n = 7$ of the most stable non-degenerate structures in each generation ensures a wide structural diversity that includes, at least for smaller n, highly symmetrical adamantane-like structures as well as many other structural motifs not seen before. As it turns out, some of these unusual novel structures are more stable than the intuitively appealing adamantane-like structures for larger values of n.

The relative stability of the n-vacancy clusters was expressed by the formation energy E_f^n

$$E_f^n = E_{vac}^n - \frac{N-n}{N} E_{cryst}^N \qquad (1)$$

and the formation energy per vacancy $E_{fV}^n = E_f^n / n$. Here, E_{vac}^n is the total energy of a defect supercell with (N - n) atoms and $E_{cryst}^N = E_{vac}^0$.

We have devoted some effort to find structures for a given n with minimum cut bonds. This is equivalent to finding adamantanes (generally diamondoids[39]) with a given number of carbon atoms but with the minimum number of hydrogen atoms. Assuming that the classical adamantane (tetrahedral $C_{10}H_{16}$) belongs to the class of such molecules, we proceeded generating other tetrahedral diamondoid clusters with apparently minimum number of H-atoms. These also contain the maximum number of closed 6-membered rings. Starting from these structures, we obtained smaller clusters by removing those atoms that created the minimum number of hydrogens for the given cluster. The results of this construction are part of Fig. 1 and their

significance is discussed there in that context. Note that these adamantane-like structures with the minimum hydrogens (or cut bonds for the vacancy clusters) are referred to here as "globular" due to their relatively compact shapes.

The optimized structures are analyzed with the Materials Studio (MS)[40] molecular visualizer by evaluating the radial distribution function (pair correlation function) g(r) for $1.3 < r < 2.4$ Å. Angular distribution functions are also calculated for bonded contacts defined as r(CC)<1.65 Å, although MS does not take into account the PBC, leading to an undercount of the angles at the boundary of the supercell. The r(CC)<1.65 Å criterion has also been imposed for determining the coordination number, CN in the carbon networks, in this case including the PBC. In the following, V_n refers to the most stable structure obtained for *n*, unless noted otherwise.

Results and Discussion

One of the original ideas about relative stabilities of vacancy clusters and pores comes from counting cut bonds.[41] For a given *n*, so long as *n* is small, the structures that correspond to the minimum number of cut bonds maximize cyclohexane-like six membered rings and are presumed to correspond to stable structures. The network of these structures corresponds to the carbon framework of adamantane-like structures (diamondoids). Of these, particularly stable should be those that are most "compact", closest to a spherical (globular) shape.

This is true for silicon (with the notable exception[42] of $n = 17$) and diamond, provided that *n* is small. Note that the most stable structure for V_{17} has been identified in silicon as being different from an adamantane-like structure due to relaxation.[42] Our generational algorithm

automatically included this structure, which cannot be generated from the adamantene structures directly, but our generational algorithm does generate it and found it to be V_{17_3} (in our nomenclature, this is the 3rd most stable of the V_{17} structures). This fact alone suggests that our algorithm is capable of finding structures that are more stable than those obtained by more ad hoc procedures.

Figure 1 shows the number of cut bonds calculated for the most stable V_ns as a function of *n* compared with the minimum number of cut bonds for a continuous cluster of *n* atoms that may be excised from a diamond lattice. Note that for some *n* values it may be possible that a smaller number of cut bonds can be found; our curve represents an upper bound. The numbers plotted correspond to structures that we have constructed. The true minimum may be lower, but the data in Fig. 1 clearly show that for $n > 25$, and even more so for $n > 40$, the structures with the smallest energy have more cut bonds than the minimum number. This is a key result that has important consequences for discussing low density carbon structures. Relaxation seems to stabilize structures that have a higher number of cut bonds than the minimum number. Clearly, factors other than the number of cut bonds contribute significantly to the energy, confirming that quantum mechanical treatment that includes non-local effects must be used for these systems in order to obtain the correct overall behavior.

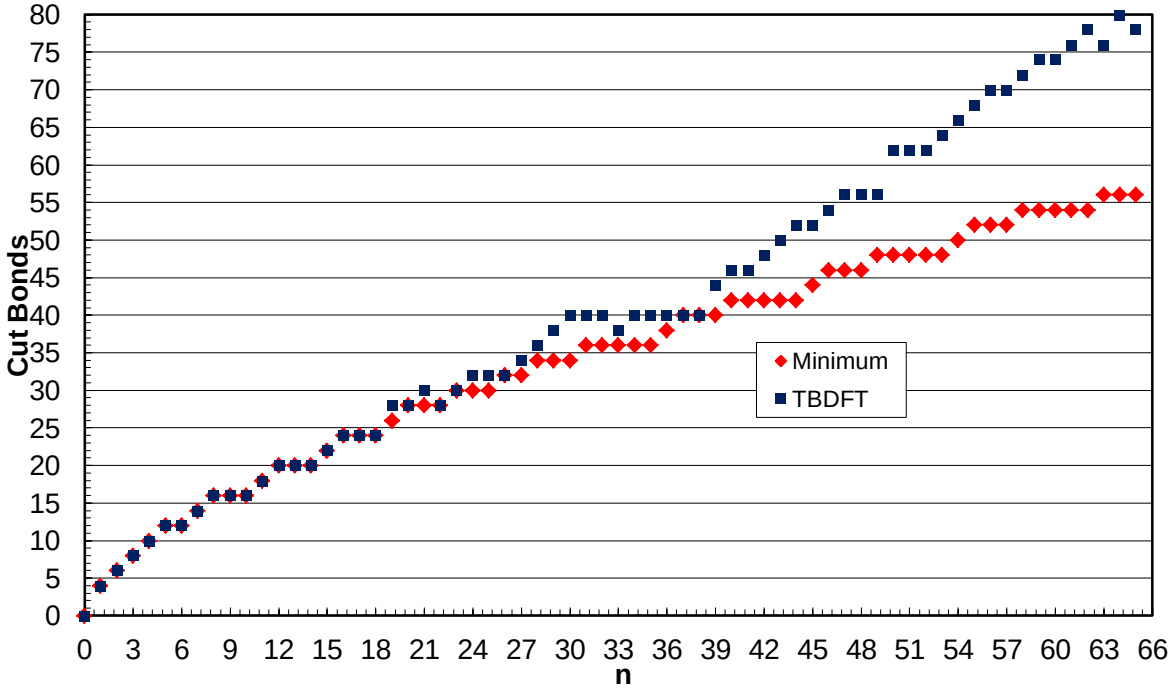

Figure 1. Number of cut bonds in the most stable V_ns as a function of *n*, obtained by the algorithm of this paper and TBDFT (squares), compared to the minimum number of cut bonds that is possible within a diamond-like connectivity (diamonds) as a function of *n*. Where diamonds are invisible, the TBDFT results correspond to the minimum number of cut bonds.

The number of cut bonds is constant in certain regions for a few *n* values before jumping by two. The *n* values before the jump are "magic" numbers in the sense of counting cut bonds, because they correspond to a local maximum of the ratio *n*/CB. However, these "magic" numbers are not defined on the grounds of energetics. Therefore, it is clear that these "magic" numbers, MN, (6, 10, 14, 18, 22, 26, 30, 35, 39, 44, 48, 53, etc.) are not always the most stable, as already discovered earlier for specific cases. [29,42] This observation is a key motivation for keeping several members of each generation. As mentioned above, the presented algorithm satisfies this requirement by maintaining structural diversity and deviating from any preconceived notion about the ideal stable shapes for vacancies and pores, such as adamantane-

like or graphitic. Note that the assumption of graphitic shapes has been adopted in various analyses of pore properties.[43] Do we find graphitic shapes are particularly stable?

The formation energies are shown in Fig. 2 as a function of *n* for the most stable structures. The following trends are observed. We concur with other work on silicon and carbon that for smaller values of *n*, "magic *n* values" appear as particularly stable: for *n* = 6, 10, 14 and 22. Beyond these values the curve becomes less structured, partially owing to the fact that the "parentages" are switching in the algorithm as *n* increases.

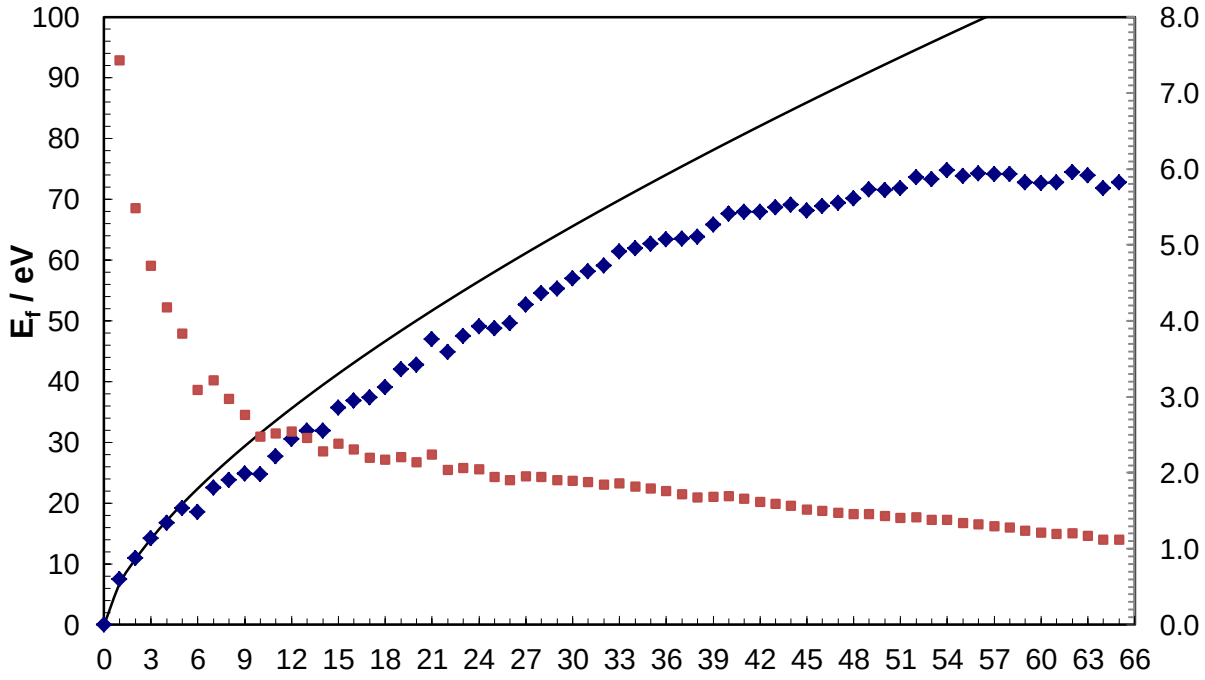

Figure 2. Formation energy, E_f^n, of the most stable V_ns as a function of *n*. The continuous line is Eq. (2) with $f = 0.6233$, see text.

Simple dimensional analysis yields the following result. Assuming simple additivity (no energy bands or delocalization) and a globular (essentially spherical) pore with radius *R*, one

concludes that if *CB* is the number of bonds cut in cluster, then $E_f^n \sim CB$. Since *CB* ~ Surface Area ~ R^2 , and *n* ~ volume ~ R^3,

$$E_f^n(\text{dim.}) = kn^f \ . \qquad (2)$$

Here *k* is a fitting constant and *f* = 2/3. We have obtained a linear regression of the TBDFT calculated $\log E_f^n$ values vs. log *n*. This fit gave an exponent of *f* = 0.6233 for *n* < 43, and *k* = 6.708 (R^2 = 0.996) . The respective plot is included in Fig. 2. Deviations from this simple relationship of Eq. (2) clearly indicate the special stabilities of clusters with the 'magic' values of *n* = 6, 10, 14, 22. (The fact that n=18 is not particularly stable is an early indication that counting CBs can go only so far.) Larger stable *n* values are less pronounced, and beyond *n* > 50 a new trend seems to take over with smaller differences between neighboring E_f^n values. For these larger *n* values the periodic cells start to allow the interactions of the vacancy clusters in adjacent cells, and eventually they become interconnected pore structures.

The *n* = 6, 10, 14 and 22 values correspond to adamantane-like structures with "magic" numbers. An additional minimum occurs on the curve around *n* = 25-26 (the actual structure is still adamantane-like, but does not correspond to the structure with minimum cut bonds). There is a small blip but not a minimum at *n* = 37-38. Note that the next adamantane-like structure at *n* = 33 (not a magic number) is stable, but it does not appear to be particularly more stable than the adjacent V_{32} or V_{34}. The lack of well-defined minima for larger *n* is another indication that stabilization of these structures becomes less local, and the number of cut bonds criteria is being replaced by a more global transition to graphitization. This is illustrated by Fig. 3 which shows the relaxed structures for n=45. (Several other cases are shown in the Supporting Information.)

Regions of planarization and graphitization can be clearly recognized and emerge without picking any structural motifs before the optimization based on some preconceived notion of how the structures should look. These are the optimized structures that appear as most stable from the diversity of initial atomic arrangements via the presented generational algorithm.

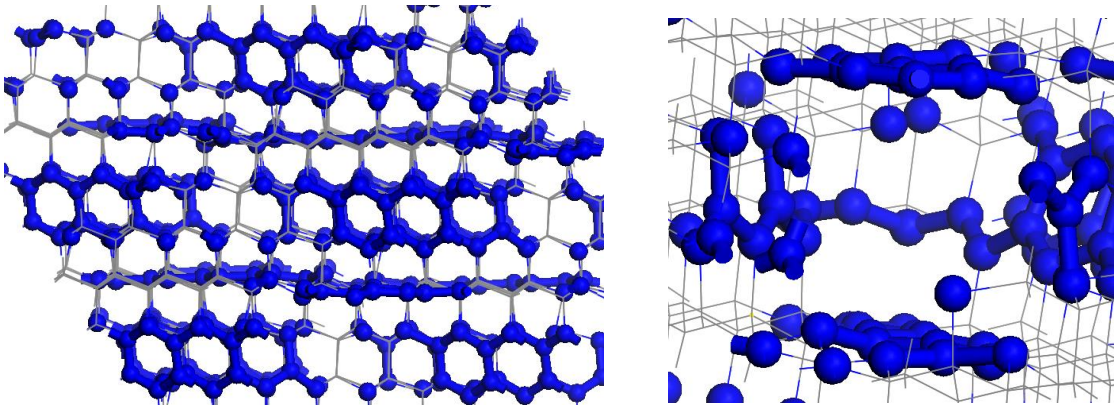

Figure 3. Structure of the most stable V_{45} obtained in the modeling. Large spherical atoms indicate carbons that are nearly sp^2 hybridized indicating local graphitization. These atoms are near the void created by the vacancy cluster and have coordination numbers below 4. Two views are provided to aid the visualization. The regions of local graphitization are apparent and are represented by several condensed aromatic-like rings.

Since there appears little preference for vacancy clusters with "magic" number of cut bonds beyond n = 22, one might like to see if there is any preference for incorporating smaller vacancy clusters, such as V_1 or V_2 as they diffuse through the material. In particular, we have asked the question: What is the energy gain, E(n-1,1) in the following "reaction":

$$V_{n-1} + V_1 \rightarrow V_n \, ? \qquad (3)$$

The respective energy difference is plotted in Fig. 4. The data clearly show the particular stability of the "magic" n values of n = 6, 10, 14 and 22. For larger vacancy clusters, n = 25 and 45 appear significantly more stable than their neighbors indicating regions of higher and lower

stability as a function of *n*. Given the generic shapes of these larger vacancy clusters, simple interpretations based on adamantane or other preferred structures do not seem possible.

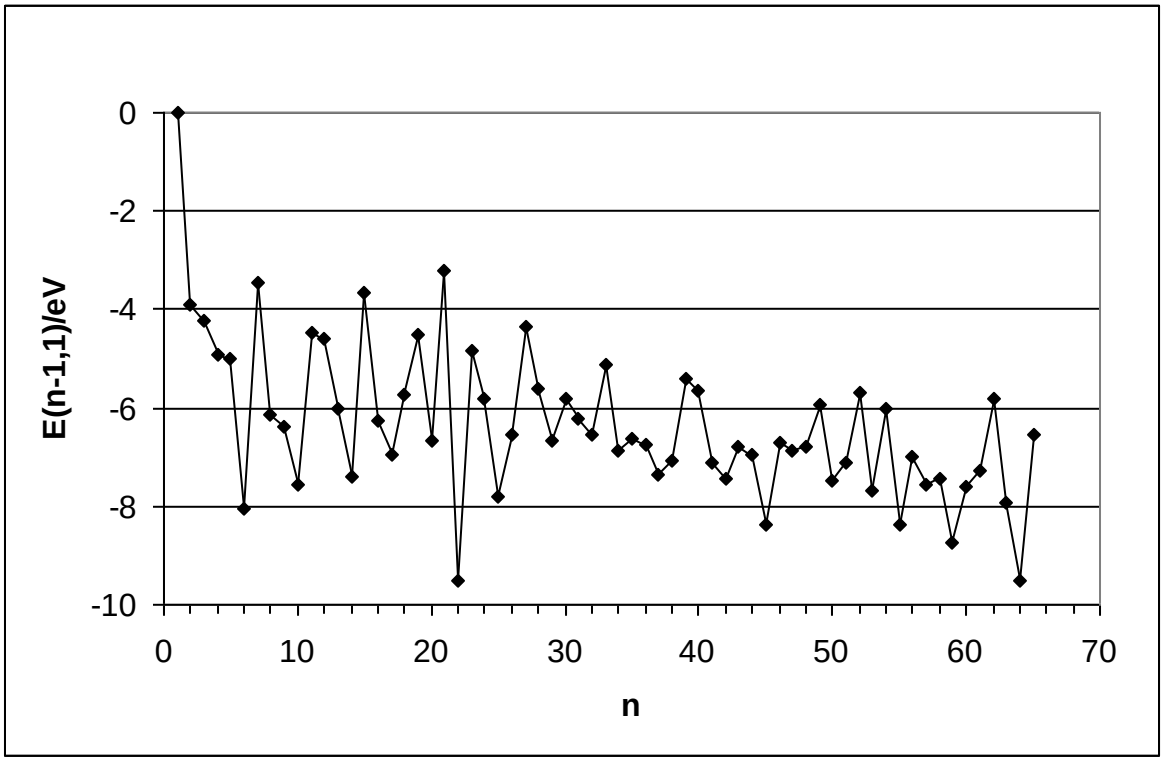

Figure 4. Formation energy difference for the $V_{n-1} + V_1 = V_n$ process, Eq (3). The energy of this reaction is calculated by E(*n*-1,1)= $E_f^n - E_f^{n-1} - E_f^1$.

However, a new trend has emerged. With increasing *n*, the excised vacancies develop in an *oblate*, rather than globular, fashion. By *n* = 20, cut bond minimization is no longer as important as local structural graphitization. Fig. 5 shows the low energy vacancy clusters for n=35 and 45 that were cut from the diamond lattice. It is clear that by n=35 the oblate structures win out against the alternatives and remain the most stable structures as n increases further. (The Electronic Supplementary Information section contains figures of further selected structures.)

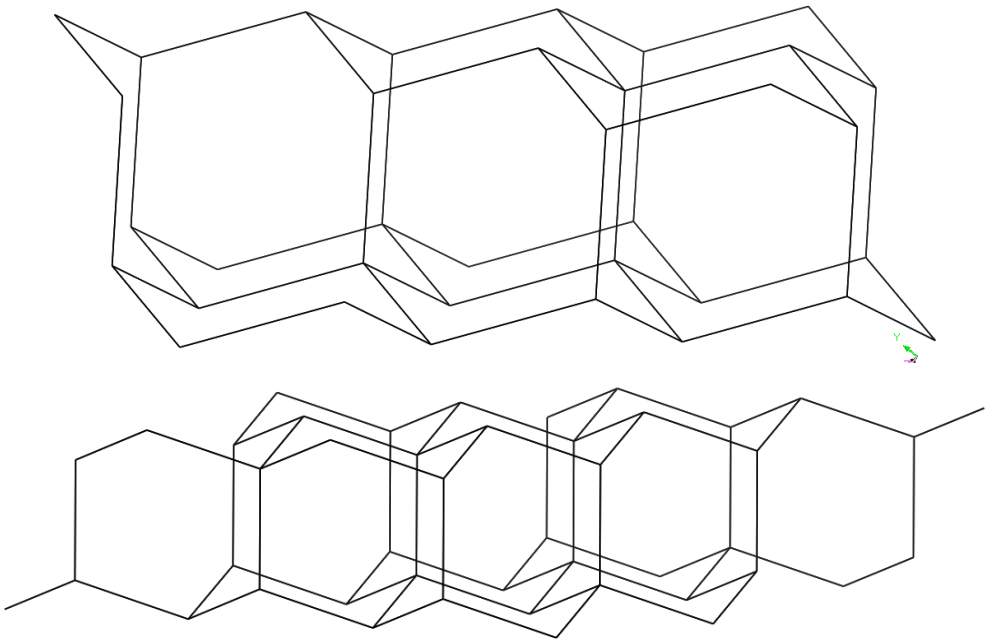

Figure 5. Selected unrelaxed structures: the V_{35} (top) and V_{45} (bottom) vacancy clusters represented as diamondoids. These structures turned out to be the most stable for the given n after geometry relaxation

Inspection of the stable structures for n>20, indicates that structural elements appear showing three-connected atoms and near planar six-member rings, indicating approximately sp^2 hybridization. The spontaneous emergence of oblate pores and nearly sp^2 hybridization are a key result of the presented modeling: pores that show graphitic tendencies emerge if there is no structural bias in the structures available for the energy minimization. This is an atomistic level proof for the applicability of the slit pore model,[43] which was developed for porous graphitic carbons, to diamond.

Pore structures with larger *n* appear more amorphous, and therefore a statistical analysis is useful. We have calculated the pair correlation function for the optimized structures. Significant values of this function indicate unique bonding schemes in addition to the typical

distances for single bonds at ~1.54 Å, and ~1.40 Å for graphitic/aromatic bonds. For instance, we observe some shorter double bond-like distances at ~1.35 Å. Significant contributions for *r* values below 1.5 Å and above 1.6 Å indicate special bonding circumstances that form an important component of the analysis of the resulting optimized structures. Fig. 6 shows the result for n = 45 which is representative for the larger V_ns. (Further examples for similar g(r) functions are given in the ESI section.)

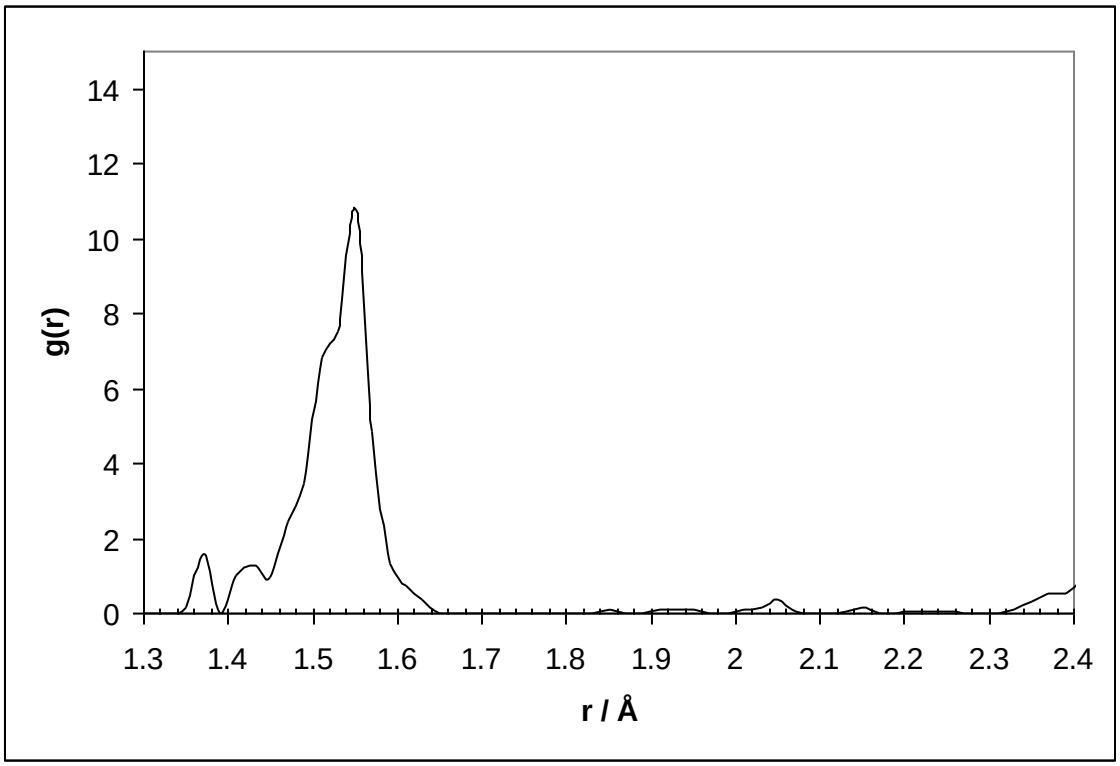

Figure 6. Calculated pair correlation function, g(r) for V_{45} in the 1.3 Å < r < 2.4 Å range. Note the appearance of contacts in the usually absent regions, as discussed in the text.

While each case is different, the following trends can be observed. The dominant peak is at 1.54 Å corresponding to the ordinary σ-bonds prevalent in diamond even when vacancy

clusters are present. The side peak and a shoulder at smaller values of *r* correspond to aromatic/graphitic CC bonds that are close to sp^2 hybridization and appear at 1.45 Å and 1.50 Å. The minor peak at 1.35 Å indicates particularly short CC bonds. Given the absence of chains[44] (coordination number CN=2 along consecutive neighbors) these data do not indicate the presence of CC triple bonds or cumulene-like bonds (Eq. (3)) or acetylene like bonds (Eq.(4)) which require CN=2. We see no evidence of the emergence of these bond types, as

…C(3) = C(2) = C(3)… or (3)

…C(any)-C(2) ≡ C(2) - C(any)… (4)

within the network of the simulated vacancy cluster. Here C(j) indicates a carbon with j neighbors.

Low coordination numbers emerge in various computational models of carbons phases.[45] However, we do not see linear chains or chain segments in the presented low energy relaxed structures. This aspect needs further theoretical modeling and experimental research. For $r > 1.54$ Å, a clear shoulder appears at 1.59 – 1.63 Å. Such bonds are known in the chemistry literature and can be attributed to lengthened single bonds that appear in strained rings.[46]

Most unusual, however, are the small peaks between 1.7 and 2.4 Å. These contacts—can we call them bonds, or even stretched bonds?—appear as the structure attempts to accommodate the strains caused by the presence of the vacancy cluster and the delocalization of the electrons in the dangling bonds. These appear for smaller V_ns, even for V_6, and are discussed in ref. 33 as being the consequence of the relaxation around the dangling bonds and can be described with a

tetrahedron of local graphitization, TOLG. Clearly, the first neighbor contact distances of 2.01 ± 0.11 Å, found in the TOGs for $n \leq 14$, are highly unusual. Equilibrium carbon-carbon bond distance in any of the over 400,000 organic molecular structures in the Cambridge Structural Database (CSD) do not show any CC contacts in the 1.75 to 2.8 Å range.[47] For $n > 14$ discussed in this paper, a variety of these CC contacts appear. Due to the presence of second neighbor distances in the 2.4 to 2.8 Å range, we focus on the statistics below r = 2.4 Å. The specific locations of these peaks in g(r) vary, but they are present in all stable structures obtained in the paper. With increasing n, the different regions of r values appear first sporadically and then more frequently and more evenly distributed. These contact distances between 1.7 and 2.4 Å indicate that larger vacancy clusters display a significant number of unusual CC contacts (bonds) that cannot relax into the usual CC bond distances and graphitic van der Waals contacts. Note that a CC distance similar to these at 2.1 Å appears in the monovacancy (5-9 defect) of graphene.[48]

The absence of carbons with a low coordination number, CN=2, in our modeling needs further comment. Such structural elements are highly characteristic and would have important consequences for reactivity, vibrational and other properties. However, what we find is that the low coordination number typically implies in these vacancy clusters that any two-connected carbon has another additional neighbor to which it is weakly coupled and is less tightly bonded because this additional (3^{rd}) neighbor lies a bit further away. For instance, in the V_{45} case we found two carbons with coordination number, CN=2, if coordination number is defined as the number of carbon neighbors with CC contacts < 1.65 Å. However, the three nearest distances for one of these carbons is 1.588, 1.604, 1.939, and for the other: 1.572, 1.578, 2.014 Å. Thus the

third neighbor is at ~2 Å away, and so the carbon cannot be considered as cumulenic or acetylenic in the usual sense, due to the presence of this third ligand carbon. Such a third neighbor is an essential feature of the structures we see, and is similar to the examples found for smaller vacancy clusters that are part of the unusually elongated CC bonds characteristic of relaxed vacancy clusters.[33] At this point we have only indirect evidence that these CN=2 sites are highly reactive as indicated by their modified Fukui indices that we have calculated. These indices will be analyzed and discussed in a forthcoming publication.[49] We also note that as expected, these reactivity indices are low for those carbons that are part of a graphitic-like network.

Structural information is presented in an alternative manner as the distribution of the bond angles. A typical case, the V_{30} is shown in Fig. 7, a few further representative cases are given in the SI. The dominant peak is near the ideal tetrahedral angle of the diamond network, 109.5°. The additional peak near 120° is a clear sign of graphitization. The small peak below 100° and the side peaks near the tetrahedral angle peak represent strained bonding environments. There is a complete lack of angles beyond 125° is in contrast to the amorphous modeling based on Brenner-type potentials.[45a] The bond angle distribution is a sensitive tool to capture graphitic, tetrahedral and linear hybridizations (or the lack thereof as in this case), it also supplements the information obtained from the distance distribution that provided a more detailed description of the relaxation mechanism that are at work in allowing the surfaces of the vacancy clusters to move toward more graphitic regions.

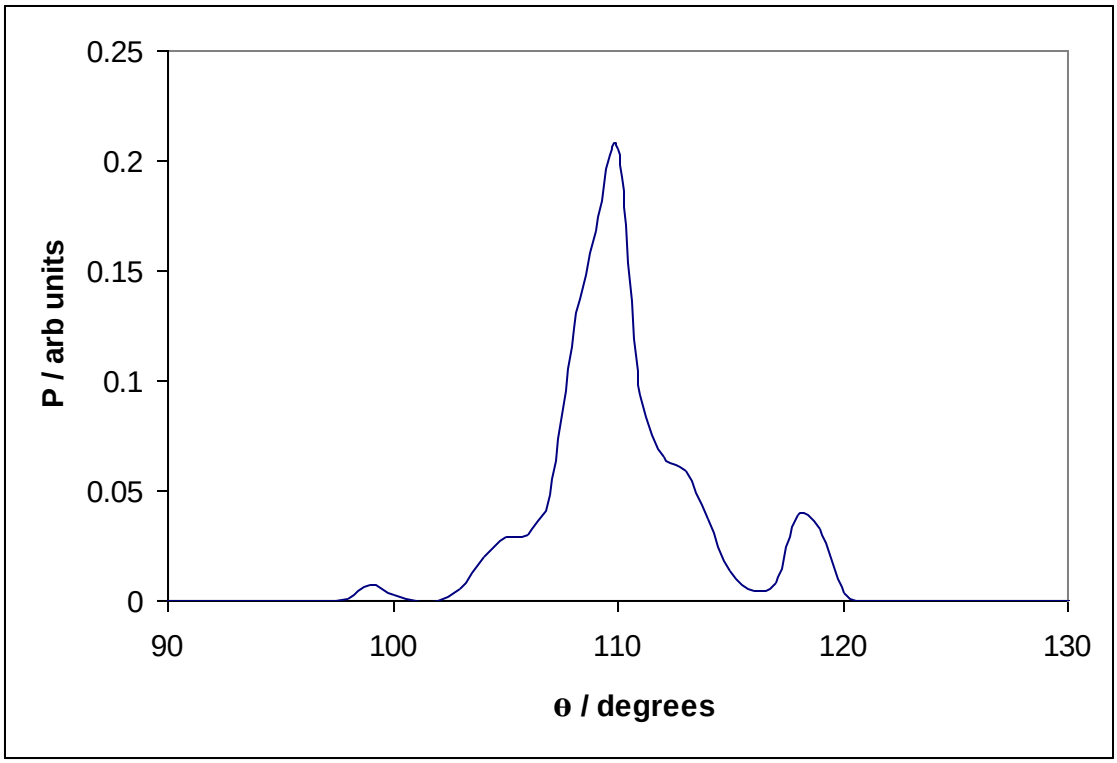

Figure 7. Calculated bond angle distribution function for V_{30}.

Concluding Remarks

Through extensive modeling of a large number of vacancy clusters obtained by a generational algorithm with up to 65 missing carbon atoms we have demonstrated that the shapes of stable large vacancy clusters in diamond are determined not by minimizing cut bonds, but from the creation of pores with internal surface relaxation leading to graphitic-like local structures. This is clearly visible in the angle distributions, and its consequences are seen in the radial distributions as well. These large vacancy clusters show structural elements not seen in other areas of the chemistry of carbon due to the rigid covalently connected carbon framework surrounding the vacancy cluster. The trend towards oblate clusters and the beginning of

graphitization in larger vacancy clusters provides an atomistic basis for the use of slit pore model[43] to diamond-structured materials.

Acknowledgements. Support from the DOE (Grant No. DE-FG02-07ER46472 and DE-FG01-05ER05-01) is gratefully acknowledged. David Hyde-Volpe's stay at Georgetown University was supported by a Research Opportunity for Undergraduates Grant from NSF (CHE-0851581). Support by GridChem is acknowledged for computer time. We thank Georgetown University's Advanced Research Computing Group for their assistance.

Supplementary Information

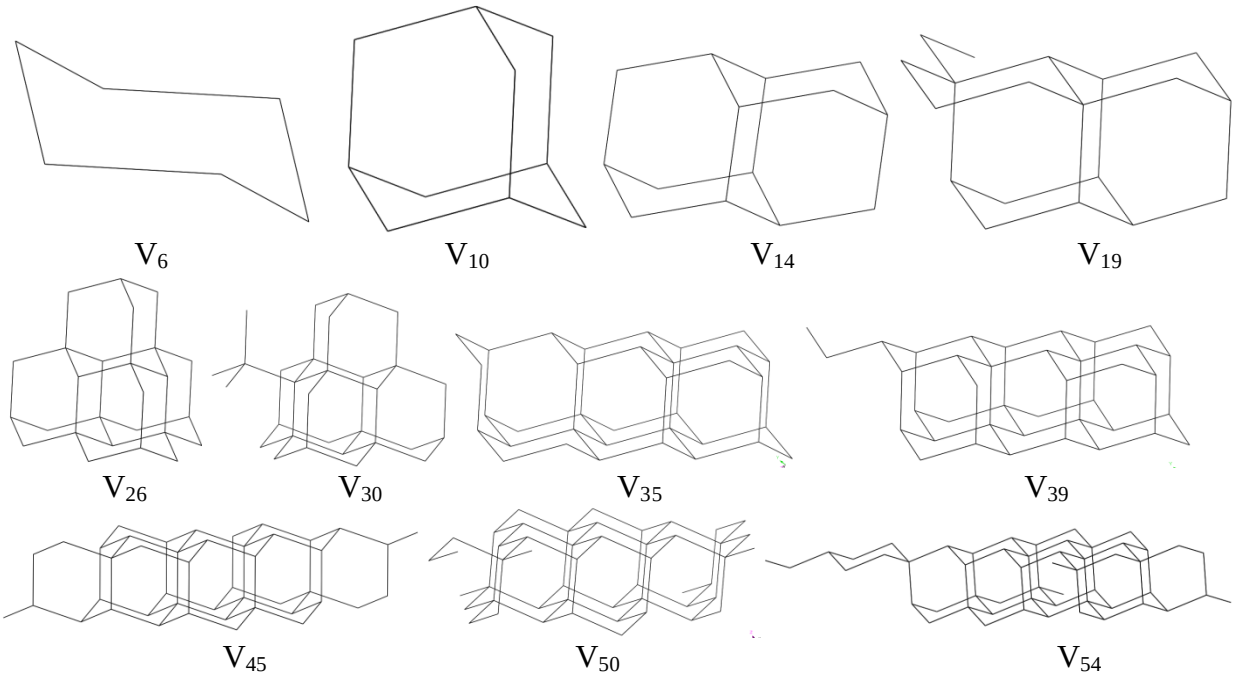

Figure S1. Unrelaxed structures of selected vacancy clusters V_n (n=6, 10, 14, 19, 26, 30, 35, 39, 45, 50, 54). Not that these structures turned out to be the most stable for the given n after geometry relaxation

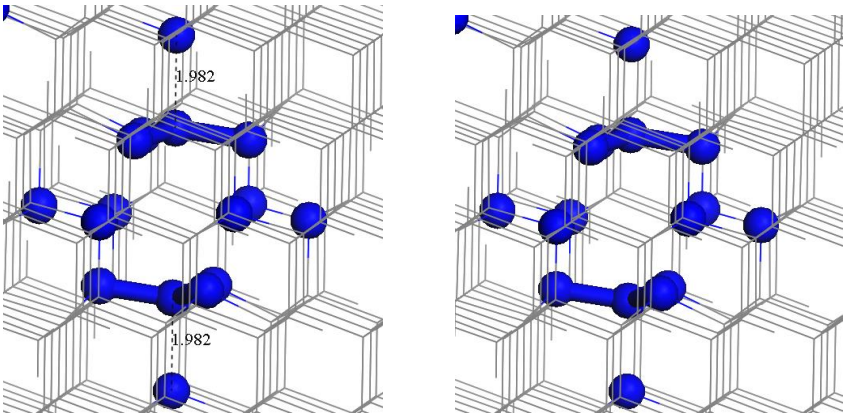

V_6

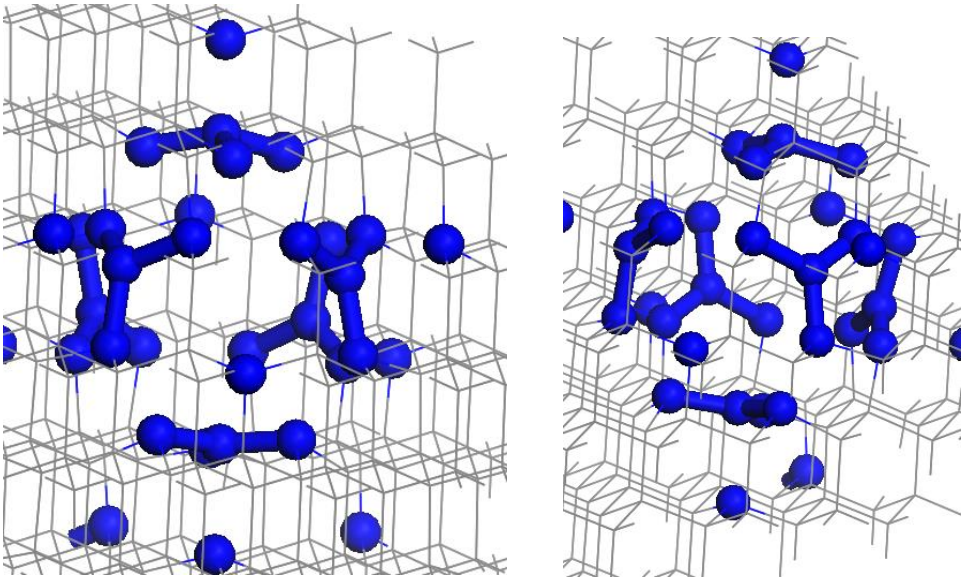

V_{14}

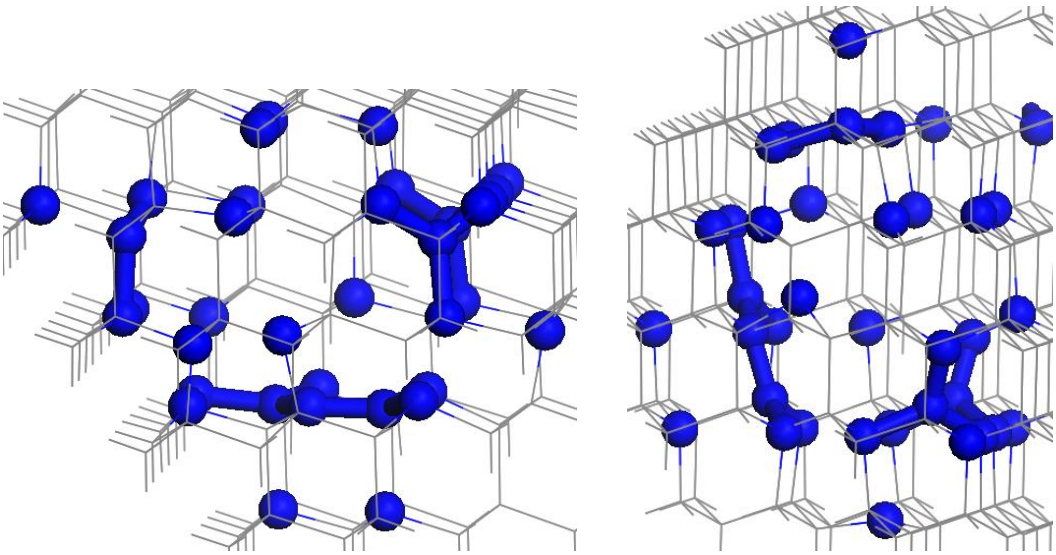

V_{19}

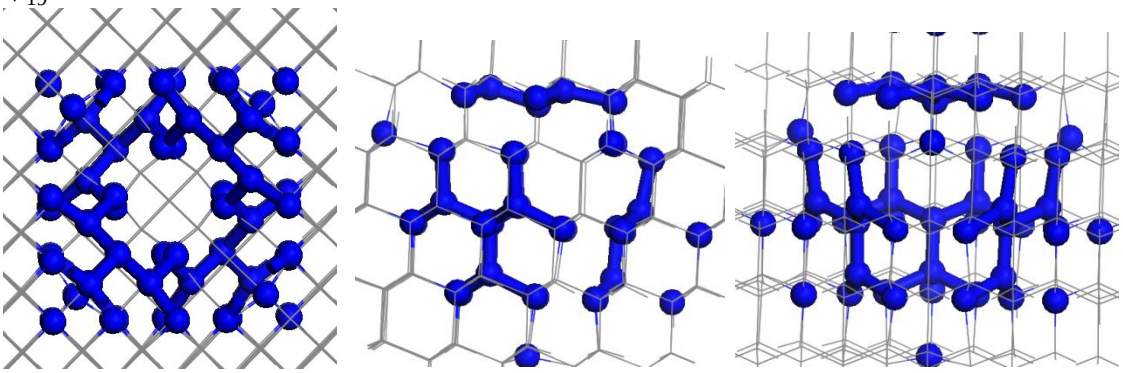

V_{26}

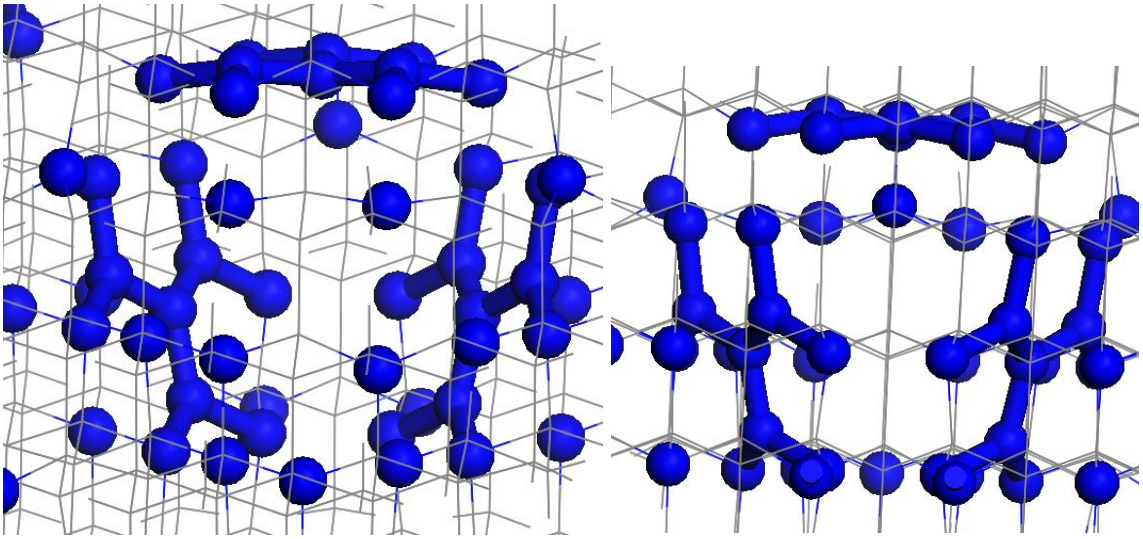

V_{30}

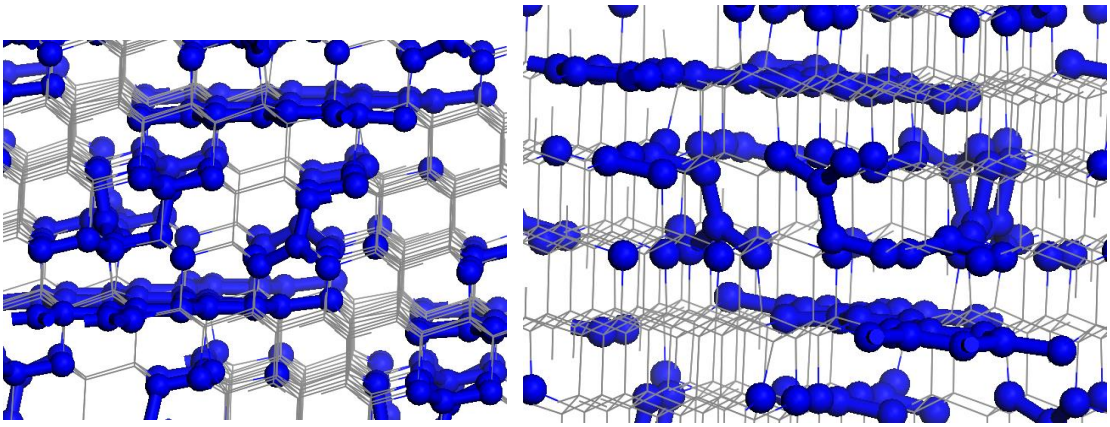

V_{39}

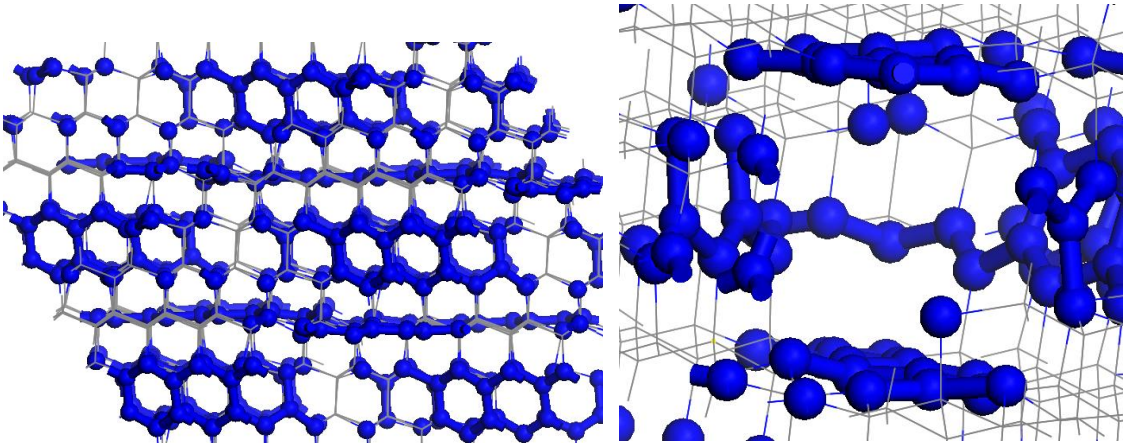

V_{45}

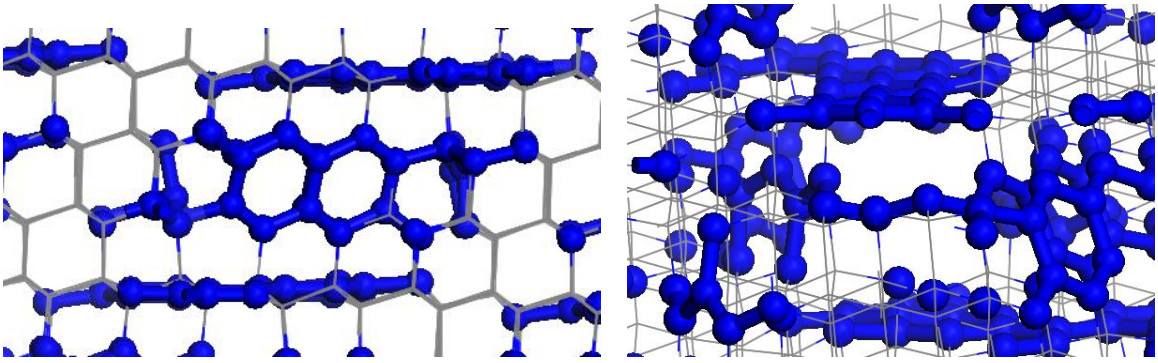

V_{50}

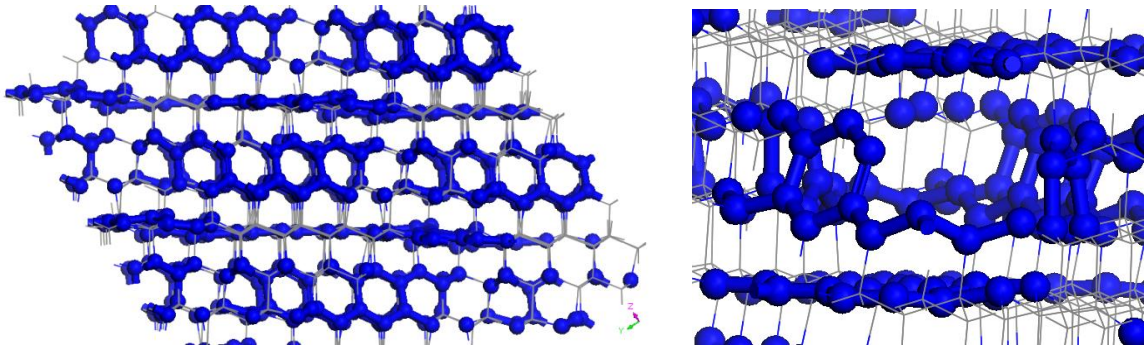

V_{54}

.

Figure S2. Relaxed structures of selected vacancy clusters V_n (n=6, 14, 19, 26, 30, 39, 45, 50, 54). These structures are the most stable for the given n values. Larger blue atoms indicate those that are adjacent to the pore left by the vacancy cluser and undergo the largest rearrangement upon relaxation. As n increases, regions of local graphitization become energetically favorable. For each V_n different views are provided to aid the visualization.

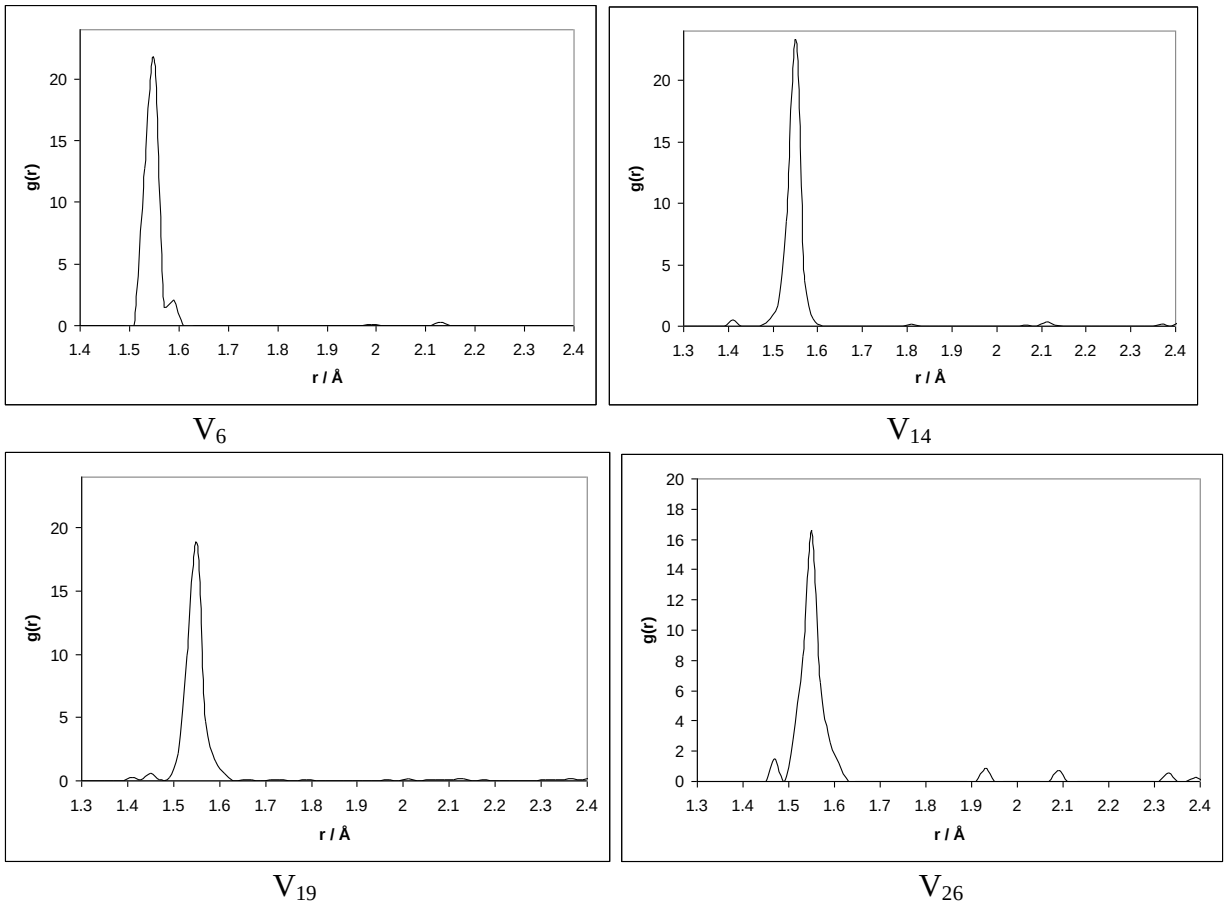

V_6 V_{14}

V_{19} V_{26}

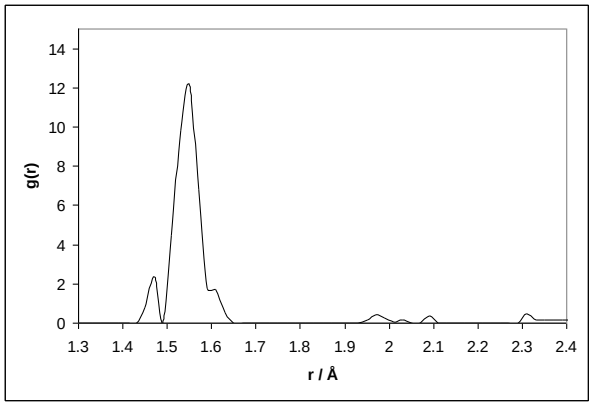

V_{30}

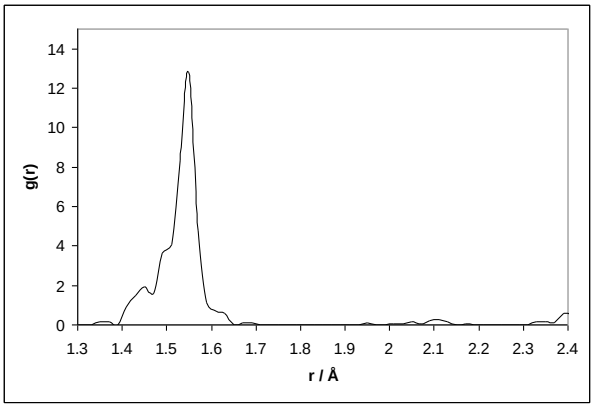

V_{39}

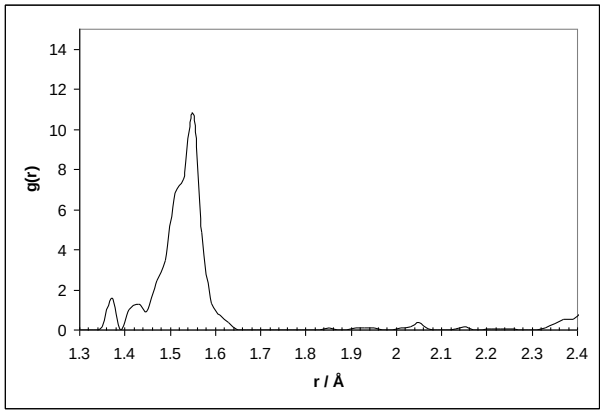

V_{45}

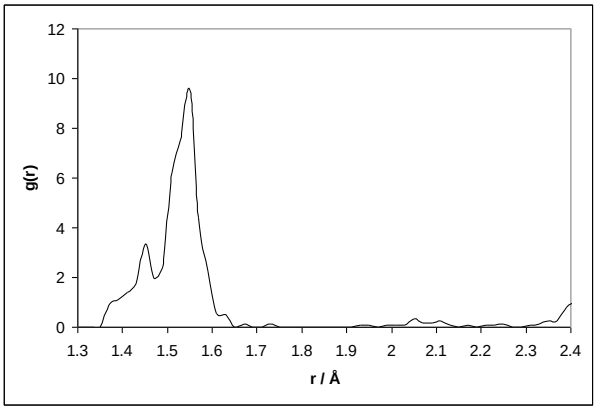

V_{50}

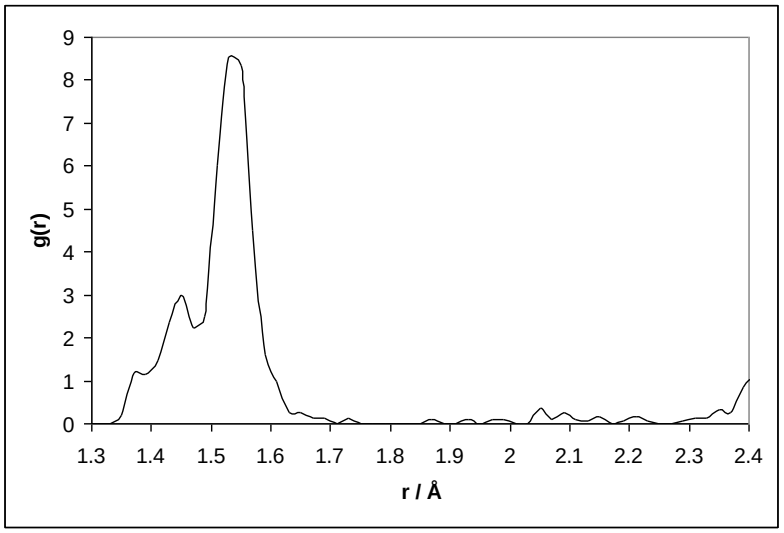

V_{54}

Figure S3. Calculated pair correlation function, g(*r*) for V_n in the 1.3 Å < *r* < 2.4 Å range. (n=6, 14, 19, 26, 30, 39, 45, 50, 54).

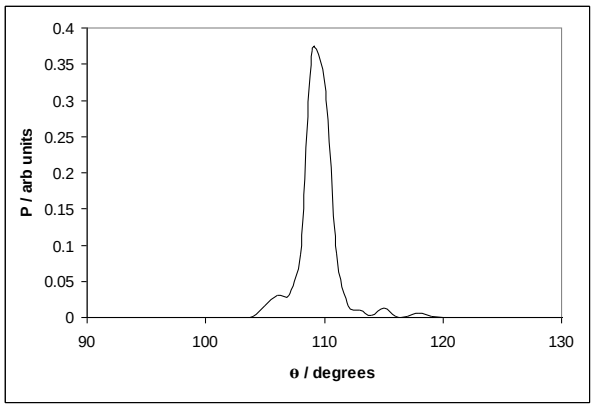

V_6

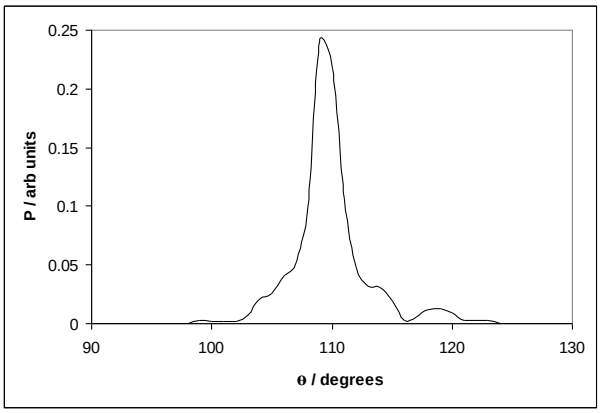

V_{14}

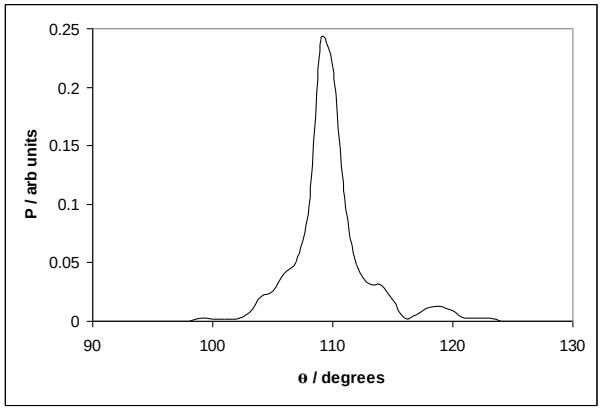

V_{19}

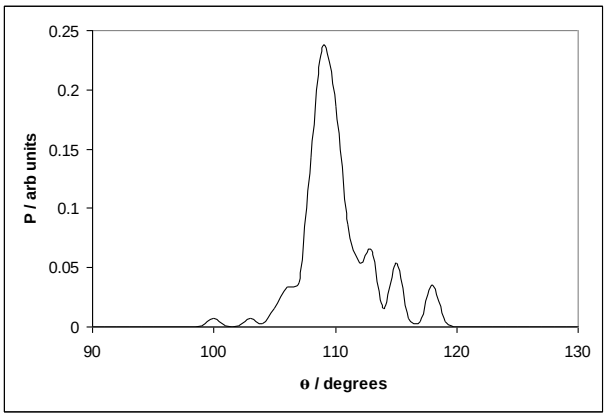

V_{26}

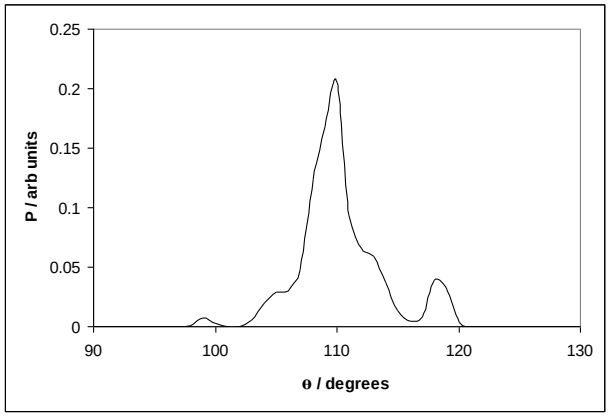

V_{30}

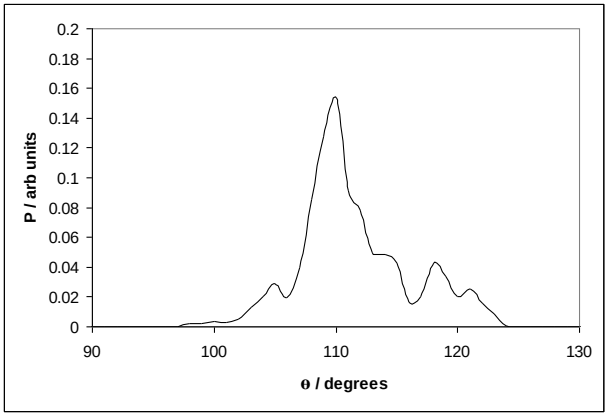

V_{39}

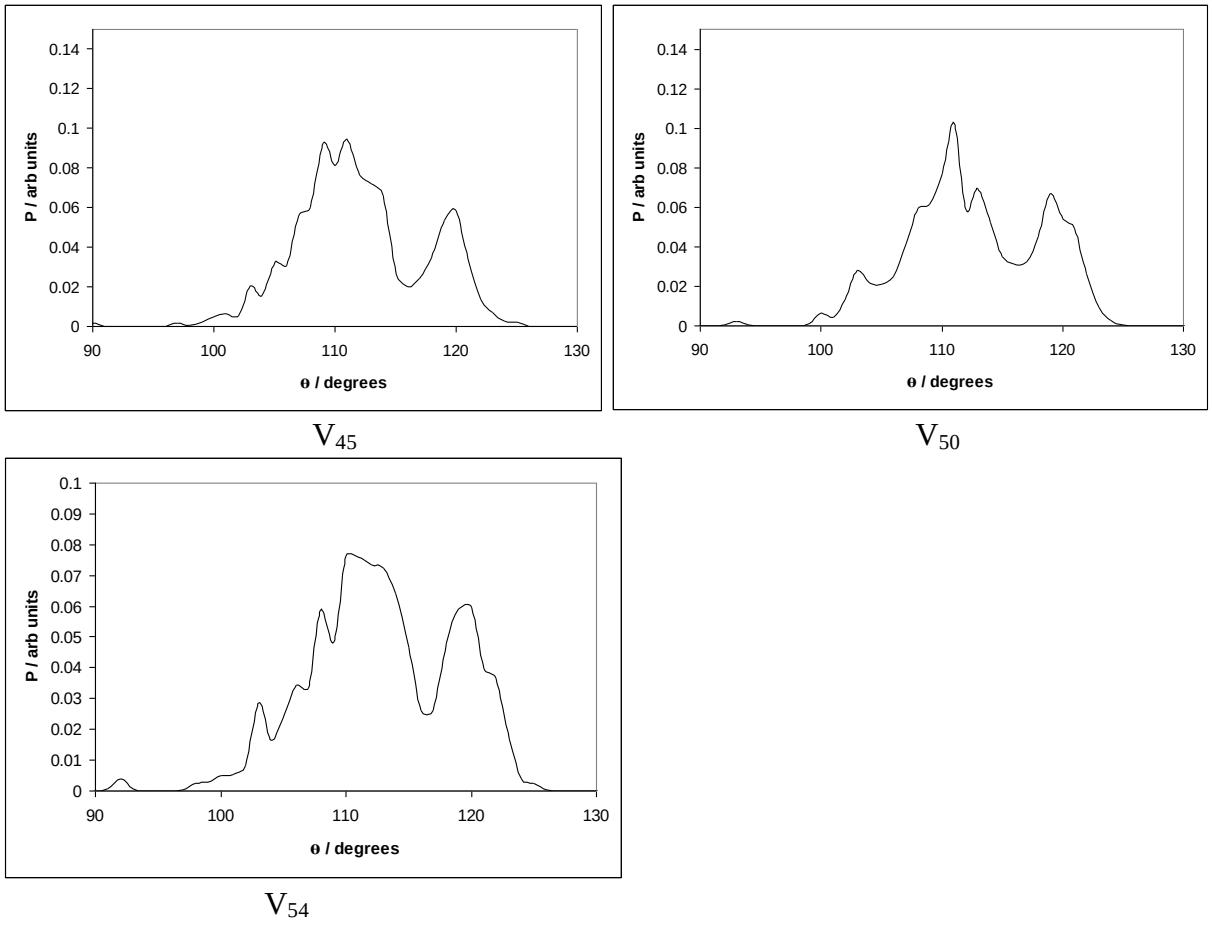

Figure S4. Calculated bond angle distribution function, P, for V_n in the $90 < \Theta < 130$ range. No angles are observed outside the presented range. (n=6, 14, 19, 26, 30, 39, 45, 50, 54).

References

[23] D.M Gruen, O.A. Shenderova and A.Y. Vul, Synthesis, Properties and Applications of Ultrananocrystalline Diamond, Springer, Dordrecht, Berlin, Heidelberg, New York, **2005**.

[24] J. M. Baker, *Diamond Relat. Mater*. **2007**, *16*, 216.

[25] (a) U. Bangert, A.J. Harvey, R. Jones, C.J. Fall, A.T. Blumenau, P.R. Briddon, M Schreck and F. Hörmann, *New J. Phys*. **2004,** *6*, 184. (b) K. Iakoubovskii, S. Dannefaert and A. Stesmans. *Phys. Rev. B* **2005**, *71*, 233201.

[26] See e.g. (a) S. Welz, Y. Gogotsi and M. J. McNallan, *J. Applied Phys.*, **2003,** *93*, 4207. (b) T. X. Nguyen, J.-S. Bae and S. K. Bhatia, *Langmuir*, **2009**, *25*, 2121.

[27] J. Chmiola, G. Yushin, Y. Gogotsi, C. Portet, P. Simon and P.L. Taberna, Science, 2006, 313, 1760.

[28] (a) B.J. Coomer, A. Resende, J.P. Goss, R. Jones, S. Öberg, and P.R. Briddon, *Physica B***,** **1999**, *274*, 520.

(b) L.S. Hounsome, R. Jones, P.M. Martineau, D. Fisher, M.J. Shaw, P.R. Briddon and S. Öberg, *Phys. Rev. B*, **2006**, *73*, 125203.

[29] L.S. Hounsome, R. Jones, P.M. Martineau, M.J. Shaw, P.R. Briddon, S. Öberg, A.T. Blumenau and N. Fujita, *Phys. Stat. Sol. (a)* **2005,** *202*, 2182.

[30] (a) R. Jones, B.J.Coomer, J.P. Goss, B. Hourahine and A. Resende, in *Special Defects in Semiconducting Materials, Solid State Phenomena*, edited by R. P. Agarwala, Vol. 71. pp 173-248. (Scietech Publications Ltd., Zuerich-Uetikon, Switzerland, 2000).

(b) A, Blumenau, R. Jones, T. Frauenheim, B. Willems, O.I. Lebedev and G. van Tendeloo, *Phys. Rev. B* **2003**, *68*, 014115.

[31] N. Fujita, R. Jones, S. Öberg, and P.R. Briddon, *Diamond Rel. Mat.* **2009,** *18*, 843.

[32] D. Porezag, T. Frauenheim, T. Köhler, G. Seifert and R. Kaschner, R. *Phys. Rev. B* **1995**, *51*, 12947.

[33] "Simulations of large Multi-atom Vacancies in Diamond" I. Laszlo, B. Slepetz, M. Kertesz and Y. Gogotsi, *Diamond Rel. Mat*. **2010**, in press.

[34] See e.g. S. Irle, G. Zheng, M. Elstner and K. Morokuma, *Nano Lett.* **2003**, *3*, 465.

[35] D. W. Brenner, O. A. Shenderova, J. A. Harrison, S. J. Stuart, B. Ni and S.B. Sinnott, *J. Phys.: Solid State* **2002**, *14*, 783.

[36] O.A. Shenderova, D.W. Brenner and R.S. Ruoff, *Nano Lett.* **2003** *3*, 805.

[37] I. Snook, A. Barnard, S. Russo, R. Springal and J. Srbinovsky, *J. Molec. Simul.* **2005**, *31*, 495.

[38] A. Sorkin, J. Adler and R. Kalish, *Phys. Rev. B.* **2006**, *74*, 064115.

[39] A.T. Balaban, D.J. Klein, J.E. Dahl and R.M.K. Carlson, *The Open Org Chem. J*., **2007**, *1*, 13.

[40] Materials Studio v4.3.0.0 Copyright 2008, Accelrys Software Inc.

[41] D.J. Chadi and K.J. Chang, *Phys. Rev. B* **1988**, *38*, 1523.

[42] T. Akiyama, A. Oshiyama and O. Sugino, *J. Phys. Soc. Jap.* **1998**, *67*, 4110.

[43] S.K. Bhatia and A.L. Myers, *Langmuir*, **2006**, *22*, 1688.

[44] For linear chains in carbons, see e.g. G. Onida, N. Manini1, L. Ravagnan, E. Cinquanta, D. Sangalli, and P. Milani, *Phys. Status Solidi*, **2010**, *B 247*, 2017.

[45] (a) S. K. Jain, R. J.-M. Pellenq, J.P. Pikunic and K.E. Gubbins, K. E. *Langmuir*, **2006**, *22*, 9942.

(b) B. Saha, S. Shindo, S. Irle and K. Morokuma, *ACS Nano*, **2009**, *3*, 2241.

(c) J.C. Palmer, A. Llobet, S.-H. Yeon, J.E. Fischer, Y. Shi, Y. Gogotsi and K.E. Gubbins, *Carbon*, **2010**, *48*, 1116.

[46] For strained single bonds, see: C.H. Choi and M. Kertesz, *Chem. Comm*. **1997**, 2199. For compressed single bonds, see: D.R. Huntley, G. Markopoulos, P.M. Donovan, L.T. Scott and R. Hoffmann, *Angew. Chem*. **2005**, *44*, 7549. For CSD statistics, see J.S. Siegel, *Nature* **2006**, **439**, 801.

[47] Cambridge Structural Database (CSD), http://www.ccdc.cam.ac.uk/products/csd/

[48] A.A. El -Barbary, R.H. Telling, C.P. Ewels, M.I. Heggie and P.R. Briddon, *Phys. Rev. B.* **2003**, *68*, 144107.

[49] B. Slepetz, I. Laszlo, and M. Kertesz, to be published. See also, Martinez, J. *Chem. Phys. Lett.* **2009**, *478*, 310.

CHAPTER 4

THE [V-C=C-V] DIVACANCY AND THE INTERSTITIAL DEFECT IN DIAMOND: VIBRATIONAL PROPERTIES[*]

Abstract

We describe a particularly stable isolated divacancy [V-C=C-V] in diamond, in which the two vacant sites are separated by two bonded carbons. Its structure, vibrational properties and stability are described by using Density Functional Theory (DFT). We validated the calculated C=C stretching frequencies for eleven molecules. The isolated divacancy [V-C=C-V] is found to be very stable and is separated by a high barrier of 5 eV from the divacancy of two missing adjacent carbons, V_2. The predicted characteristic C=C stretching frequency of the isolated divacancy [V-C=C-V] is 1607 cm^{-1}, close to Raman bands at 1620-1630 cm^{-1} observed in various nanodiamonds, offering an alternative interpretation for the assignment of this vibrational band. We conclude that the alternative interpretation based on the CC stretching mode of an interstitial defect can be ruled out. Our accurate and validated vibrational calculations offer further evidence that the vibrational structure of the 3H optical center in diamonds should be assigned to the interstitial defect because it provides excellent agreement with the observed vibrational frequencies of three isotopologues.

[*] Reproduced with permission from [Hyde-Volpe, D.H.; Slepetz, B.; Kertesz, M. *J. Phys. Chem C* **2010**, *114*, 9563-9567] Copyright [2010] American Chemical Society.

Introduction

Diamond-like materials including nanodiamonds contain a large variety of defects that are difficult to identify at the atomic level.[1] A particularly important question is the ratio of the sp^2/sp^3 carbons.[2] Raman spectroscopy has been particularly useful in identifying sp^2 carbons due to the signature bands of the C=C vibrations observed around 1620-1630 cm^{-1} under a variety of synthetic and preparative conditions in nanocrystalline diamonds.[3] A Raman band around 1600 cm^{-1} has been associated with the reorganization of amorphous carbon into a graphitized phase.[4] Mochalin et al. assigned the broad asymmetric bands between 1500 and 1800 cm^{-1} with a maximum around 1640 cm^{-1} to -OH bending with minor contributions from sp^2 carbons and C=O group stretching .[5] Note that the peak of these bands in various experiments is at a higher frequency than the G band that is observed in graphite, carbon nanotubes and graphitic carbons around 1580 cm^{-1}.[6] Earlier studies on amorphous carbons indicated that localized modes above 1300 cm^{-1} occur that are attributable to sp^2 hybridization.[7] Note that localized CC stretching modes under ~1380 cm^{-1} are difficult to observe due to the bulk vibrational modes of diamond itself.[8]

The modeling of defects and vacancies in diamond began with Coulson and Kearsley who used qualitative molecular orbitals for the dangling bonds around a diamond monovacancy, V_1.[9] A recent Molecular Dynamics (MD) investigation, using a Brenner potential, of the 1630 cm^{-1} peak assigns the frequency to the much-discussed [100] split interstitial.[24] Jones et al. investigated by DFT various interstitial defects in diamond offering the interpretation of a board range of experimental data relating to their vibrational bands.[23]

The key challenges for modelling vibrational modes of defects in diamond are: (a) Assumptions about the nature and geometry of the defect and its environment can profoundly affect the vibrational modes. (b) The level of theory at which reasonably reliable vibrational frequencies can be obtained is rather high, and often frequency scaling is necessary in order to obtain frequencies that are within 10-15 cm^{-1} of the observed modes.[10] (c) Intensities of vibrational modes require even higher levels of theory; resonance Raman intensities are particularly challenging to calculate and therefore vibrational band intensities will not be addressed here.[11] In this paper we propose a possible interpretation of the 1620-1630 cm^{-1} Raman band as arising from a particularly stable divacancy structure, the [V-C=C-V], which is described below.

Twitchen, et al. identified the so called R4/W6 EPR active center in diamond as belonging to the [111] divacancy cluster, V_2, ruling out a possible divacancy arrangement involving a "[V-C-C-V]" defect, possibly containing a double bond, with C_{2h} symmetry.[12,13] In this notation, only carbons are indicated through which the two vacant atoms can be connected via a shortest path. In the presented calculations for this connected divacancy we determined the C-C interaction to be essentially a normal double bond. The direction of the C=C bond before relaxation is parallel to [111], but relaxation changes this direction. We will refer to this defect as the isolated divacancy [V-C=C-V]. As two isolated monovacancies in a cubic diamond lattice migrate towards each along the [110] chain, the two monovacancies must, before they can merge to form the more stable V_2, adopt the configuration [V-C=C-V] (Figure 1).

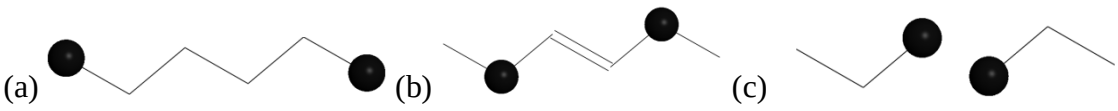

Figure 1 Migration of the monovacancies along the [110] chain. Vacancies are shown as large black spheres. (a) two V_1 vacancies separated by three atoms [V-C-C-C-V] (b) [V-C=C-V] defect that is described in this paper (c) divacancy, V_2.

If such a [V-C=C-V] structure would be stable, an issue to be investigated, then it would represent a trap for two migrating monovacancies as two of the eight dangling bonds of the two approaching V_1 vacancies begin to overlap to form an essentially normal, though somewhat pyramidalized, π-bond. (Note that in Fig. 1. the hypothetical [V-C-V] vacancy cluster is missing, that is an unstable species.) This decrease in the number of dangling bonds is expected to lower the formation energy of the [V-C=C-V] defect relative to two isolated V_1 vacancies. The [V-C=C-V] defect could be observable at mid-range annealing temperatures (700-950 K) [14], where the monovacancy is mobile, but not enough thermal energy is available to form a divacancy, V_2. The presented DFT calculations describe the stability and diffusion barriers leading to [V-C=C-V] and preventing it from collapsing into V_2.

Frequency trends based on pyramidalized double bonds from the literature[15] foretell that there might be a strong Raman peak around 1600 cm^{-1} for the [V-C=C-V] defect structure. This is confirmed by the presented calculations and is discussed below. This peak should be observable if the defect is the dominant defect due to the fact that no other vibrational mode is present in the 1600 cm^{-1} region of diamond.[11]

Methods

Computations were performed using DMol[16] in the Materials Studio (Accelrys Inc.) package of programs. The Becke,[17] Lee, Yang, and Parr[18] (BLYP) non-local density functional was utilized with a double numerical (DN) basis set. Direct inversion of the iterative subspace (DIIS) and smearing of 5 mHa was employed to improve self consistent field convergency. A hydrogen terminated cluster (HTC), containing the defect, was used in the presented calculations. Formation energies for defects in the HTC were calculated as follows

$$E_f = E_N^v - E_N^0 + v\mu_c \qquad (1)$$

where E_f is the formation energy, N is the number of atoms of the defect-free cluster, v is the number of vacancies, E_N^v is the calculated energy of a cluster containing N-v atoms, E_N^0 is the energy of a defect-free cluster, and μ_c is the energy per C atom of diamond, calculated with a supercell containing 64 atoms and at the same BLYP/DN level.

The neutral [V-C=C-V] and other defects were created in the hydrogen terminated cluster (HTC) $C_{190-v}H_{110}$, where v is the number of vacancies. (Here only v=1 *and* v=2 cases were considered.) The CC interstitial was modeled in a cluster $C_{71+1}H_{60}$ while the Humble defect was calculated with $C_{215+2}H_{120}$. The HTC was chosen over the supercell method because it provides a good compromise between accuracy and the computational cost for the more expensive vibrational calculations. We selected the Raman active modes that involved the CC stretch and were in the 1400 to 1750 cm^{-1} region as characteristic frequencies. Our choice for the HTC was a diamondoid whose edge carbon atoms are capped by hydrogen atoms as illustrated in Figure 2).

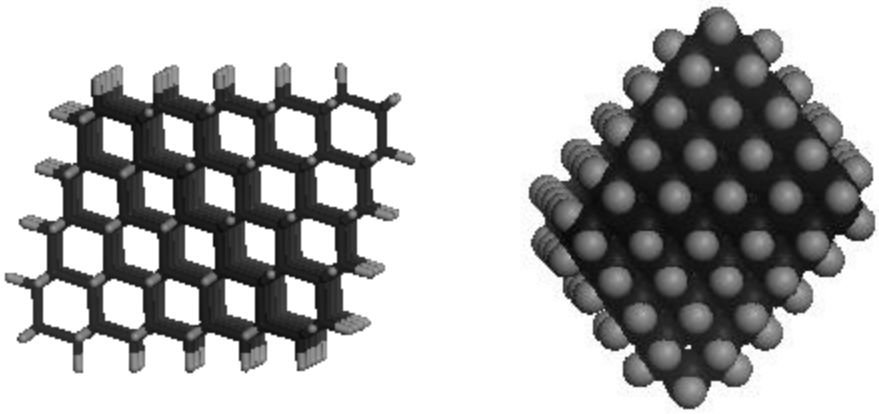

Figure 2 Two views of the C_{190} H_{110} hydrogen terminated cluster used in the calculations.

Periodic supercell calculations were also employed and are referred to in the text as "Supercell" calculations. These correspond to a 64-ν atom cubic cell with ν missing atoms. The level of theory for supercell calculations was PBE[19]/DN within the DMol package by Accelrys.

Validation

The HTC method was evaluated by three different approaches to ensure that the results matched that of the bulk diamond. The vibrational densities of states, and the electronic density of states (see Supporting Information) were in reasonable agreement with literature results.

The accuracy of the level of theory used was primarily validated by comparing our calculated frequencies to experimentally determined frequencies for a broad range of pyramidalized double bonds in small hydrocarbon molecules (Figure 3 and Table S2). Given the excellent correlation between the computed and observed frequencies, we concluded that the applied level of theory is sufficient to capture the essential parameters of the CC stretching vibration in the environments relevant for the various defects in diamond discussed here.

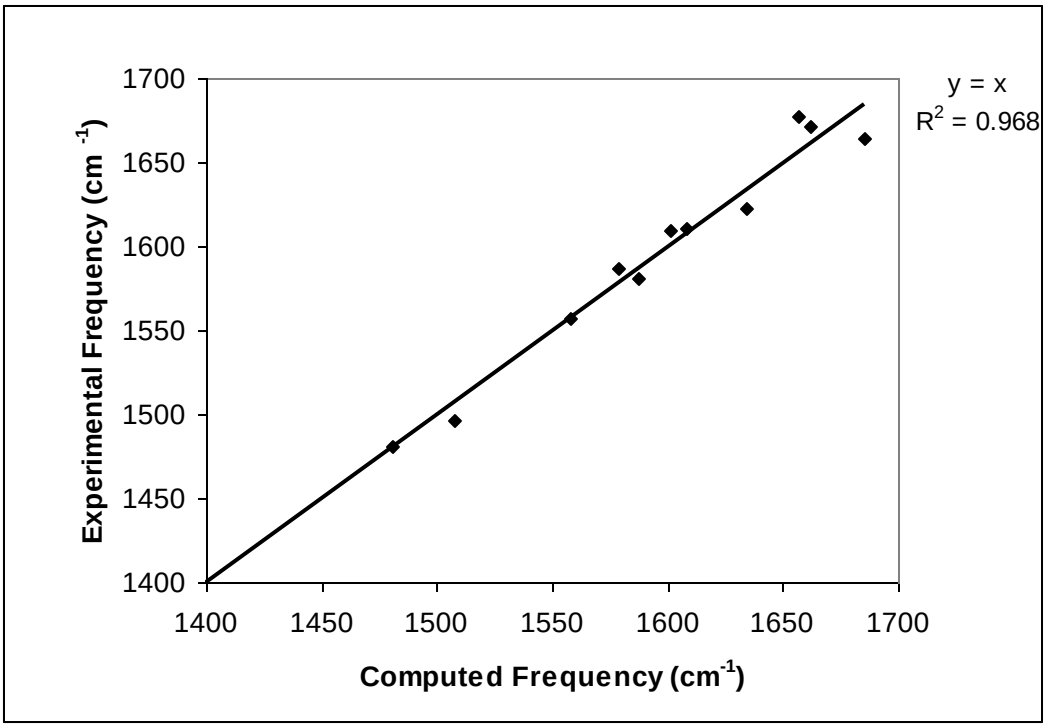

Figure 3 Correlation between computed (unscaled BLYP/DN) and experimentally determined frequencies for various pyramidalized C=C double bonds. (For the data see Table S2.)

Figure 4 contains the correlation between the calculated pyramidalization angles and the C=C stretching frequencies for the same set of molecules listed in Table S2 and compared with the respective calculated data of the [V-C=C-V] defect. This correlation helps to identify the nature of the vibrational mode discussed in the next section.

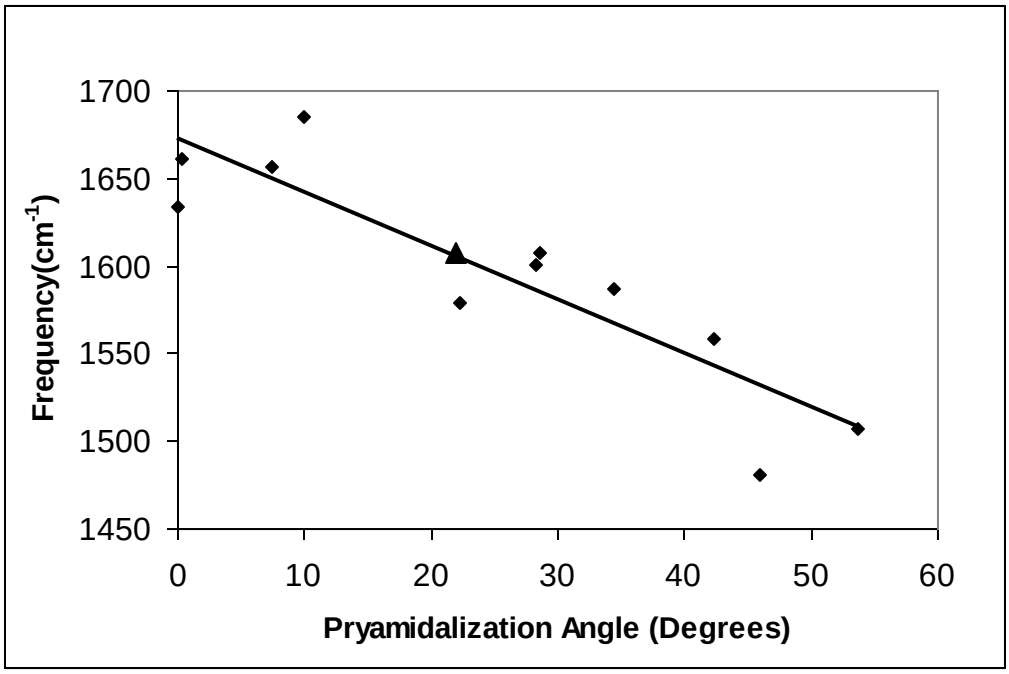

Figure 4 Computed carbon-carbon double bond stretching frequencies are shown for various pyramidalized hydrocarbon molecules as a function of computed pyramidalization angles for molecules listed in Table S2. The triangle corresponds to the [V-C=C-V] defect which is discussed in more detail below. The linear fit is shown to guide the eye.

Results

The [V-C=C-V] defect is illustrated in Figure 5. Unrestricted formalism exhibited competition between singlet and triplet ground states, the sensitivity of which is dependent on nearest neighbor relaxation. In our calculations, we obtain an open-shell singlet ground state about 8 meV lower than a triplet state (Table 1). According to the RBLYP optimization, the defect has C_{2h} symmetry and a rather short C=C double bond length of 1.352 Å. Further interatomic distances for the optimized geometry are given in the Supporting Information section. The angle of pyramidalization was found to be 21.9^{o}. This bond length and pyramidalization angle both fall in the range of our validation data, therefore, we expect the vibrational prediction to be quite accurate for the stretching mode of the defect.

Table 1: Calculated formation energies for [V-C=C-V] for different methods and spin states.

HTC	**E_f / eV**	**Supercell**	**E_f / eV**
RBYLP	12.563	RPBE	9.479
UBLYP, S = 0	11.907	UPBE, S = 0	8.926
UBLYP, S = 1	11.915	UPBE, S = 1	8.934

Based on pyramidalization alone, according to the correlation obtained in Fig 4., the [V-C=C-V] defect would be expected to have a Raman active mode at approximately 1610 cm^{-1}.

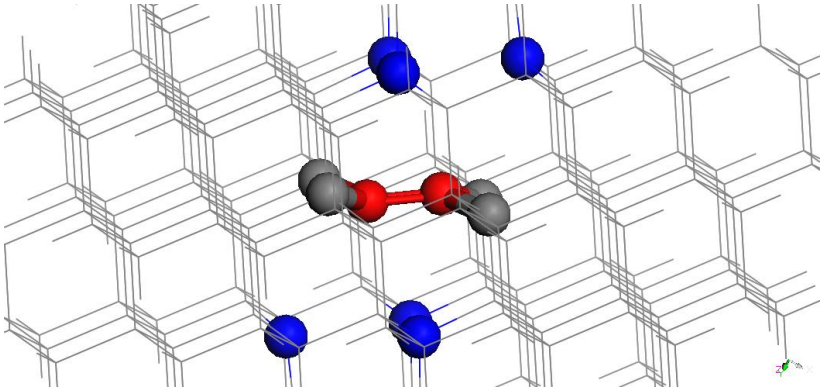

Figure 5. Illustration of the [V-C=C-V] defect. Red connected spheres represent the two doubly bonded central carbons. The carbons with dangling bonds located adjacent to the vacancies are indicated by blue spheres.

The computationally determined Raman frequency mode for the C=C stretching of the [V-C=C-V] defect is presented in Table 2, along with the istopically shifted frequencies. For comparison the CC stretching frequencies of other important defects are also given in Table 2: the C-C interstitial[20] (aka [100] split interstitial, or $I_1^{[100]}$), the Humble di-interstital and the 3H optical

center's sharp local CC stretching mode. The latter has been assigned to the C-C interstitial,[21,24] although its exact nature is being debated[22]. These two defects in diamond are illustrated in Figure 6.

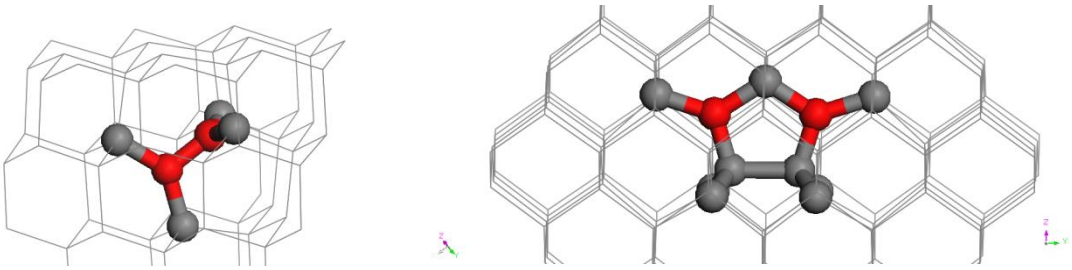

Figure 6. C-C [100] split-interstitial (left) and the Humble di-interstitial (right). Red spheres denote interstitial atoms (equivalent for C-C interstitial), gray atoms denote nearest neighbors.

Given the maximum deviation in Figure 3 of 20 cm^{-1}, the calculated value of 1607 cm^{-1} agrees very well with the experimental[3] bands at 1620-1630 cm^{-1} mentioned in the Introduction and can be considered a reasonable basis from which to tentatively assign that peak to the [V-C=C-V] defect. The close correlation of experimental frequencies with those of the presented calculations leads us to argue that the C-C interstitial produces frequencies that do not agree with the experimental data for the 1620-1630 cm^{-1} mode, and should not be assigned to that band. It is interesting to note that the three calculated frequencies of the C-C interstitial for three different isotope substituted species in this work correlate well with the local vibrational modes of the 3H optical center (Table 3). This center had been assigned[21, 24] to the neutral C-C interstitial, but more recently it has been attributed to the positively charged Humble di-interstitial.[23] Based on the frequency data presented in Table 3 we argue that the assignment of the neutral C-C interstitial to the 3H optical center is equally if not more justified. The calculated shifts for the

Table 2
Calculated CC stretching frequencies of isotope substituted local defects in diamond (cm^{-1}) compared with experiment

Type of defect	Symmetry	$^{12}C/^{12}C$	$^{12}C/^{13}C$	$^{13}C/^{13}C$
C=C [V-C=C-V][a]	C_{2h}	1607 (A_g)	1577	1546
C-C interstitial [a]	D_{2d}	1744	1711	1677
Humble di-interstitial [a]	C_{2v}	1440 (A_1) 1519 (B_2) 1661 (B_2) 1667 (A_1)		1399 (A_1) 1468 (B_2) 1599 (B_2) 1607 (A_1)
C-C interstitial[24]	Not reported	1620		
C-C interstitial[23]	D_2	1915	1842	1840
Humble di-interstitial[23]	C_{2v}	1495 (A_1) 1594 (B_2) 1826 (A_1) 1842 (B_2)	-	-
Positively charged Humble[23]	C_{2v}	1820	-	-
3H optical center[21] Experiment	C_{2v}	1757	1726	1693
Nanodiamond Raman peak[3] Experiment	-	1630	-	-

[a] This work, HTC, BLYP/DN.

^{13}C isotope substituted [V-C=C-V] defect should be experimentally testable in ^{13}C-enriched samples of nanodiamonds.

Stability of [V-C=C-V]

In order to assess the viability of such a novel defect, we need to find out whether this is a stable defect both in terms of it not collapsing into a V_2 and it being more stable than two isolated V_1 vacancies. Formation energies of the [V-C=C-V] defect along with the V_1 and the V_2 are shown in Table 3 along with supercell calculations.

TABLE 3: Computed formation energies of various vacancy defects in diamond (eV)

	[V-C=C-V], ν=2	V_1, ν=1	V_2, ν=2	[V-C-C-C-V] , ν=2
Cluster[a]	12.56	7.62	10.37	-
Supercell[b]	9.48	6.07[c]	7.81	10.20

[a]HTC, BLYP/DN, $C_{190-\nu}H_{110}$.
[b]PBE/DN, $C_{64-\nu}$.
[c] LDA DFT value by ref. [25] was 7.2eV.

The above formation energies indicate that the [V-C=C-V] defect is more stable than two isolated V_1's by about 3 eV, but is less stable than the fully localized V_2 by about 5 eV.

To be a stable, observed defect, one should expect the [V-C=C-V] to pass through a high barrier against V_2 formation since the C=C double bond must be broken as these atoms migrate towards the flanking C_3 triangles (Figure 7). We studied the barriers of the transitions between [V-C-C-C-V] to [V-C=C-V] and [V-C=C-V] to V_2, First, geometry optimizations were performed on all defects, where it was found that the V_2 is the most stable with the smallest

formation energy (Table 3). Then, transition structures were found for the reaction paths, in a way similar to reference [26] but using a quadratic synchronous transit[27]. The barrier from [V-C-C-C-V] to [V-C=C-V] was low at 1.86 eV, as compared with the measured barrier to migration of isolated vacancies[28] of 2.3 eV. In contrast, the barrier from [V-C=C-V] to V_2 was much higher at 5.17 eV. The [V-C=C-V] defect should therefore be a stable trap inhibiting the formation of V_2.

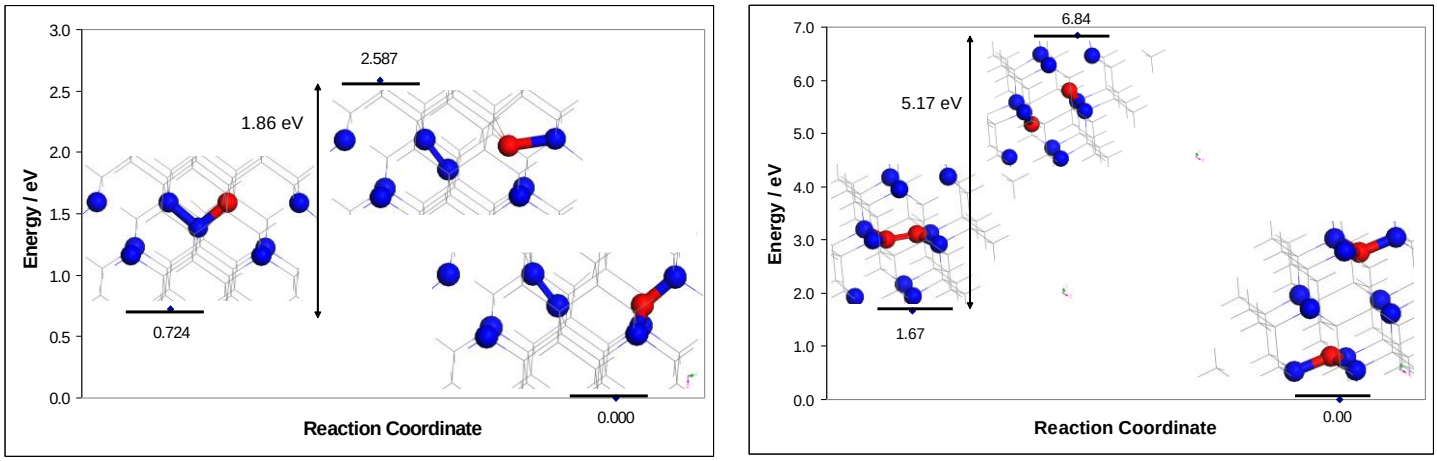

Figure 7. Energy profiles for the conversion of [V-C-C-C-V] to [V-C=C-V] (left) and [V-C=C-V] to V_2 (right). Colored spheres represent neighbors to the starting vacancy. Red spheres denote migrating atom(s). The transitions states are indicated in the middle of both diagrams.

Spin states and orbitals

We plan to discuss briefly the local orbitals that are occupied by the two radical electrons showing their pictures. A reference to Staroverov, V. N.; Davidson, E. R. *J. Mol. Struct. (THEOCHEM)* **2001**, *573*, 81. will be used to indicate the appropriateness of the UDFT for such diradicaloids.

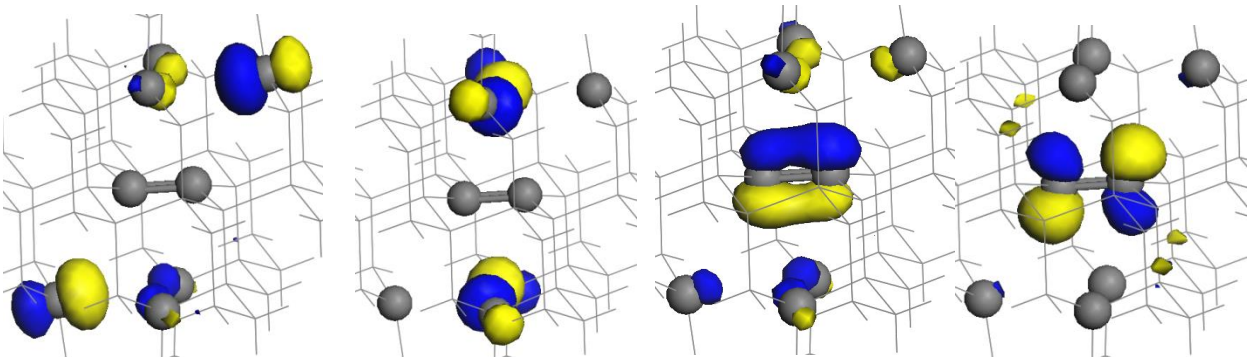

HOMO **LUMO** **HOMO-1** **LUMO+3**

Concluding Remarks

We have shown by DFT computations that a novel defect [V-C=C-V], containing a C=C double bond between two vacancy sites in diamond is a stable defect trap. It has a characteristic Raman active vibrational mode predicted at 1607 cm^{-1}, which, together with its two further isotope shifted modes should be observable. We tentatively assign this mode to the often observed 1620-1630 cm^{-1} Raman mode in diamonds noting that alternative assignments of this peak are possible depending on preparative conditions. [3, 5] We find the assignment of this band to the interstitial defect less convincing based on the presented accurate vibrational frequencies. The presence of the [V-C=C-V] defect in diamond-like materials should be verified by more direct experimental evidence. I expect something like this: The local double bond-like entity should have a low lying $\pi \rightarrow \pi^*$ transition. Our calculations indicate this to be at 3.79 eV. Given the direct coupling of this transition to the length of the C=C bond, this transition should generate a reonant Raman band for the 1607 cm^{-1} C=C stretching mode and should make it more observable. We also offer an alternative assignment of the 3H optical center to the C-C

interstitial defect given the excellent correspondence of the calculated frequencies to the observed vibrational frequencies of three isotopologues.

Acknowledgements. Support from the DOE (Grant No. DE-FG02-07ER46472) is gratefully acknowledged. David Hyde-Volpe's stay at Georgetown University was supported by a Research Opportunity for Undergraduates Grant from NSF (CHE-0851581). We are indebted to Prof. Y. Gogotsi and Dr. Vadym Mochalin for calling our attention to this problem and for useful discussions.

References

[1] Baker, J. M. *Diamond Relat. Mater*. **2007**, *16*, 216.

[2] Gilkes, K. W. R.; Prawer, S.; Nugent, K.W.; Robertson, J,; Sands, H.S.; Lifshitz, Y.; Shi, X. *J. Appl. Phys*. **2000**, *87*, 7283.

[3] Prawer, S.; Nugent, K. W.; Jamieson, D. N.; Orwa, J. O.; Bursill, L. A.; Peng, J. L. *Chem. Phys. Lett.* **2000**, *332*, 93.

[4] Ferrari, A. C.; Robertson, J. *Phys. Rev. B.* **2001**, *64*, 075414.

[5] Mochalin, V.; Osswald, S.; Gogotsi, Y. *Chem. Mater.* **2009**, *21*, 273.

[6] See e.g. Gogotsi, Y.; Libera, J.A.; Kalashnikov, N.; Yoshimura, M. *Science.* **2000**, *290*, 317.

[7] (a) Wang, C. Z.; Ho, K. M. *Phys. Rev. Lett*. **1993**, *71*, 1184.

(b) Drabold, D. A.; Fedders, P. A.; Stumm, P. *Phys. Rev*. B. **1994**, *49*, 16415.

[8] Bosak, A.; Krisch, M. *Phys. Rev*. B. **2005**, *72*, 224305.

[9] Coulson, C. A.; Kearsley, M. J. *Proc. R. Soc. London, Ser. A.* ***1957***, *241*, 433.

[10] Pulay, P.; Fogarasi,G; Pongor, G. Boggs, J. E.; Vargha, A. *J. Am. Chem. Soc.* **1983**, *105*, 7037; Baker, J.; Jarzecki, A. A.; Pulay, P. *J. Phys. Chem. A.* **1998**, *102*, 1412.

[11] See e.g. Zhang, D.; Zhang, R. Q. *J. Phys. Chem*. **2005**, *109*, 9006.

[12] Twitchen, D. J.; Newton, M. E.; Baker, J. M.; Anthony, T. R.; Banholzer, W. F. *Phys. Rev. B* **1999**, *59*, 12900-12910.

[13] Baker, J. M.; Hunt, D. C.; Newton, M. E.; Twitchen, D. J. *Radiat. Eff. Defects Solids.* **1999**, *149*, 233-237.

[14] Dannefaer, S. *Phys. Status Solidi C.* **2007**, *4*, 3605.

[15] (a) Vázquez, S.; Camps, P. *Tetrahedron.* **2005**, *61*, 5147-5208.

(b) Borden, W. T. *Chem. Rev*. **1989,** *89*, 1095.

(c) Michl, J.; Radziszewski, J. G.; Downing, J. W.; Kopecky, J.; Kaszynski, P.; Miller, R. D. *Pure Appl. Chem*. **1987**, *59*, 1613.

[16] Delley, B. *J. Chem. Phys.* **1990**, *92*, 508; Delley, B. *J. Chem. Phys.* **2000**, *113*, 7756.

[17] Becke, A. D. *J. Chem. Phys.* **1988**, *88*, 2547.

[18] Lee, C.; Yang, W.; Parr, R. G. *Phys. Rev. B*. **1988**, *37*, 786.

[19] Perdew, J. P.; Burke, K.; Ernzerhof, M. *Phys. Rev. Lett*. **1996**, *77*, 3865

[20] Breuer, S. J.; Briddon, P. R. *Phys. Rev. B.* **1995**, *51*, 6984.

[21] Steeds J. W.; Davis T. J.; Charles, S. J.; Hayes, J. M.; Butler, J. E. *Diamond Relat. Mater*. **1999**, *8*, 1847–1852.

[22] Iakoubovskii, K.; Kiflawi, I.; Johnston, K.; Collins, A.; Davies, G.; Stesmans, A. *Physica B*. **2003**, *340*, 67.

[23] Goss, J. P.; Coomer, B. J.; Jones, R.; Shaw, T. D.; Briddon, P. R.; Rayson, M.; Öberg, S. *Phys. Rev. B*. **2001**, *63*, 195208.

[24] Prawer, S.; Rosenblum, I.; Orwa, J. O.; Adler, J. *Chem. Phys. Lett.* **2004**, *390*, 458.

[25] Bernholc, J.; Antonelli, A.; Del Sole, T.M.; Bar-Yam, Y.; Pantelides, S.T. *Phys. Rev. Lett.* **1988**, *61*, 2689.

[26] Butorac, B.; Mainwood, A. *Diamond Relat. Mater*. **2008**, *17*, 1225-1228.

[27] Gonzalez, C.; Schlegel, H. B. *J. Chem. Phys.* **1991**, *95*, 5843.

[28] Davies, G.; Lawson, S. C.; Collins, A. T.; Mainwood, A.; Sharp, S. J. *Phys. Rev. B*. **1992**, *46*, 13157.

CHAPTER 5

DIVACANCY IN DIAMOND: A STEPWISE FORMATION MECHANISM*

Abstract

Diffusion of monovacancies in diamond creates various trapped multivacancy clusters. The simplest diffusion process leads to a divacancy, V_2. The formation of V_2 is a critical step in the formation of larger vacancy clusters. We explored the relaxed potential energy surfaces in the formation of V_2 by *ab initio* density functional theory (DFT) obtaining structures, relative energies, diffusion barriers and reaction paths. Divacancies separated by one carbon are not stable. Even though the divacancy is the most stable final product, a novel isolated divacancy with two vacant sites separated by two bonded carbons [V-C=C-V] can be transformed into a divacancy only via a very large (>4.3 eV) barrier and therefore it should be a defect observable in irradiated diamonds.

1. Introduction

Diamond-like materials including nanodiamonds contain a large variety of defects that are difficult to identify at the atomic level.[1] Baker has emphasized the importance to consider the vacancy cluster formation as resulting from precursors that have been created by accumulation of migrating vacancies such that a "family tree of ancestors" with sufficient stabilities and lifetimes can be identified. From this genealogical approach it follows that the steps to accumulate any particular cluster must involve precursors with the same configuration of vacancies, less one or

* Reproduced with permission from B. Slepetz and M. Kertesz; in submission: Phys. Rev. B

two adjacent vacancies. The simplest of such genealogies is the formation of a bound pair of two monovacancies, which is the subject of this work. It is surprising that the literature lacks discussion of the most elementary of these processes, the

$$V_1 + V_1 \rightarrow \text{bound } V_2 \qquad (1)$$

process, where V_1 is a monovacancy and V_2 refers to a divacancy.

Vacancy diffusion is considered as the dominant self-diffusion mechanism in diamond.[2] Butorac and Mainwood [3] revealed key parameters by first principles DFT methods of the migration of the complexes of N, H with V_1 (V in their notation) in diamond. In this work we applied a similar methodology to the following problem: what are the immediate preceding steps represented by Eq. (1)? Are there any traps that are sufficiently stable to prevent the formation of a divacancy from two diffusing monovacancies?

The nearest neighbour divacancy V_2 in diamond was confirmed by Twitchen et al. to be responsible for the "R4/W6" EPR active center. In their analysis they considered, but ruled out a possible divacancy arrangement involving a "[V-C-C-V]" defect that might contain a double bond between isolated carbons and possess C_{2h} symmetry.[4,5] This notation indicates that the two vacant atoms can be connected via a shortest path that includes two singly bonded carbons. Here, we discuss this and other hypothetical defects that must form before coalescing to the V_2. As two isolated monovacancies in a cubic diamond lattice migrate towards each other, the two monovacancies must approach each other in one of the three topologically different configurations separated by at least 3 atoms—shown in the left column of Fig. 1—before they can merge to form the more stable V_2, shown at the right end, passing through or possibly getting stuck in a series of configurations separated by at least 2 atoms (2O and 2C) and a configuration

separated by one atom (1I). These are indicated in Fig. 1. Our goal here is to explore these pathways using geometry optimizations based on density functional theory (DFT).

Due to the structural isomerisms illustrated in Fig. 1, various structures need to be compared and their mutual transformations explored energetically. For the 3 series (the vacancy positions are separated by at least 3 atoms in the lattice) the notations of E, A, and C refer to equatorial, axial and chain configurations, respectively. For the 2 series (the vacancy positions are separated by at least 2 atoms in the lattice) C and O refer to chain and opposite, respectively. For the divacancy separated by one atom there is only one isomer, (I for isolated, commonly referred to as the 'saddle divacancy') which in our analysis turns out not to be a local minimum.

Some of the barriers are so high that transformations among them are not viable at any reasonable temperature. The sequence of arrows illustrates the general direction of the formation of a V_2, which is generally an energetically favorable process due to the reduction of the number of dangling bonds from 8 (for isolated monovacancies, $2V_1$) to 6 (for a divacancy, V_2). However, just by simple bond counting one might assume that the structure 2C might become stabilized due to the possibility of relaxation of the central single σ-bond into a double bond as indicated by 2C (one of the degenerate red-blue arrangements in the top series in Fig. 1) when the dangling bonds are reoriented. Indeed, the presented calculations point to 2C being a stable trap, although not as stable as V_2.

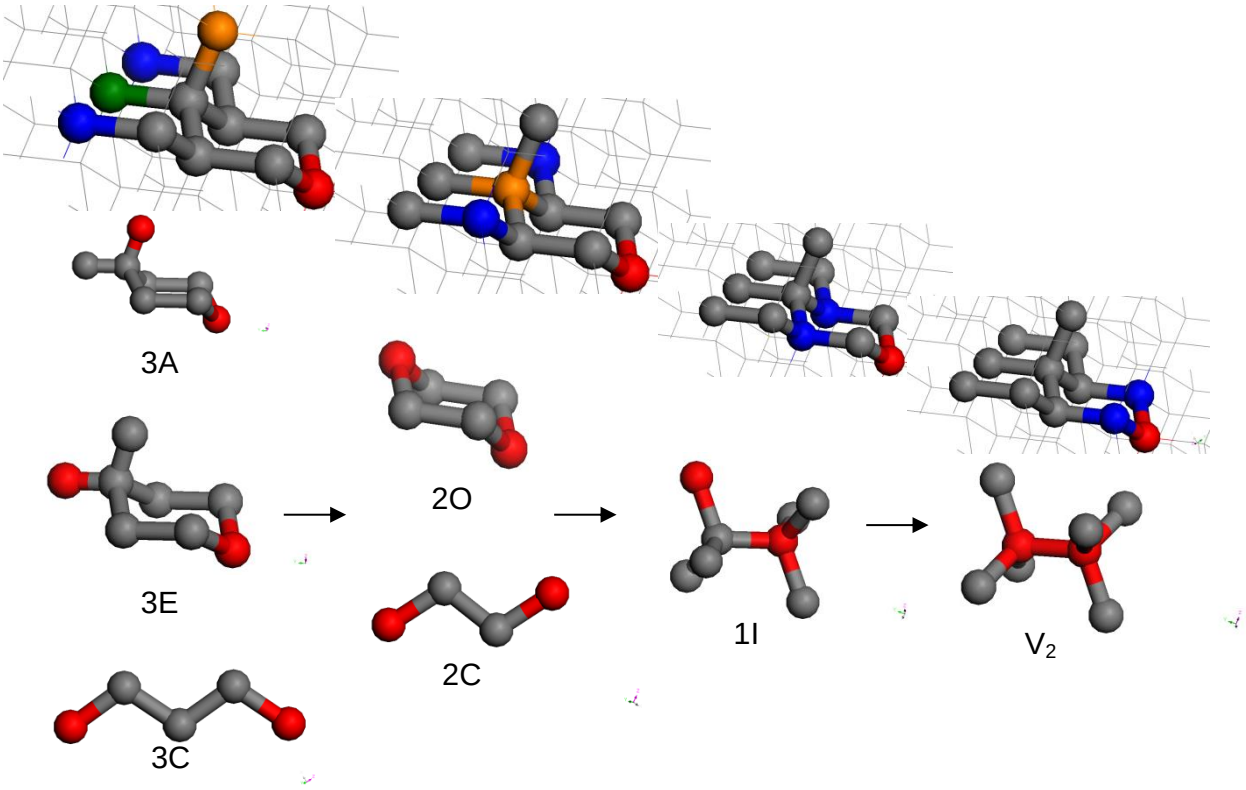

Fig. 1. Structural models for the migration of monovacancies in diamond. On the top series, color coded atoms vacancy atoms separated by 3, 2 and 1 atoms. Same color indicates degeneracy, which are shown in the diagrams underneath with respective symbols. The first number in the symbol indicates the number of atoms separating the two monovacancies.

2. Methods

The augmented plane wave electronic structure code PWscf—part of the Quantum ESPRESSO[6] package—was used to perform self-consistent field (SCF) total energy calculations on the seven species shown in Fig. 1 in both spin-polarized and closed shell formalism. All calculations on vacancy species and potential surfaces were made with the exchange correlation functional of Perdew et al. (PBE)[7]. The nudged elastic band (NEB) with climbing image method[8] was used to calculate the energies of structures along the pathway that connects relevant species.

Spin-polarization was not used in NEB calculations; instead single point spin-polarized energies are calculated on transition structure (TS) and this value is used in reporting barrier heights. For all calculations, the kinetic energy cutoff of the plane waves was 48.0 Ry with a charge density cutoff of 348 Ry. Electron SCF convergency was set at 10^{-8} within the gamma point, and Fermi-Dirac electron smearing of 10^{-3} Ry was used. A Vanderbilt ultra-soft pseudopotential, parameterized for carbon systems by Meyer[9] was used to treat the carbon core electrons. For the full geometric optimizations, convergency was satisfied when the total energy change between successive steps was less than 10^{-7} E_H and the components of all the forces on the atoms were reduced below 51 meV/Å.

Formation energies for defects were calculated as follows

$$E_F^n = E_{vac}^n - \frac{N-n}{N} E_{cryst}^N \tag{2}$$

where E_f is the formation energy, N is the number of atoms of the defect-free unit cell, *n* is the number of vacancies, E_N^n is the calculated energy of a cluster containing N-*n* atoms, E_N^0 is the energy of a defect-free cluster. A cubic supercell containing N=216 atoms within the Γ-point approximation was used. These approximations allowed extensive searches on the potential energy surface (PES). Transition structures (TS) were found by repeated conjugate gradient minimizations on an initial TS constructed from the well-defined reactant and product structures. The initial searches were followed by quadratic synchronous transit (QST) maximization.[10] The TS search process found local maxima for all structures with the exception of the 1I structure (see below).

3. Validation

We report on three cases as a way to validate our approach. First, for V_2 we obtain a ground state triplet[11] (D_{3d}) as did Coomer at al.[12] both being consistent with experiment.[4] We performed a reaction path search along the straight connecting line of the two V_1 locations along the [111] direction and obtained a barrier of 3.27 eV for the diffusion of V_1. This is in close

agreement with the 3.3 eV barrier of Breuer and Briddon.[13] along the same path although higher than the experimental barrier of 2.3 ± 0.3 eV.[14] Note, that their symmetry breaking path deviates somewhat from their value of 2.8 eV.[13] For V_1, we use a small smearing in order to maintain the T_d symmetry. We obtained a relaxed structure with an increase in the nearest neighbor distance by 0.196 Å, to be compared with the earlier LDA value of 0.2 Å.[13] The formation energy for V_1 was 6.07 eV, to be compared with the LDA results of 7.2 eV from Bernholc et al.[2]

4. Results

Equilibrium vacancy structures

What follows are brief descriptions of the eight species studied in this work: the monovacancy and seven divacancies. Both spin-restricted and spin-polarized calculations were performed and we find S = 1 states be lowest in energy for all species except for 2O and V_1, for which unrestricted S = 0 states were found to be lower, highlighting the importance of spin-polarization in describing these equilibrium structures. The geometries of the defects are not generally dependent on spin state as the rigid framework the diamond lattice prevents large changes in atomic relaxation but subtle changes are observed which sometimes makes energy

TABLE I. Formation energies, spin states, and geometries of the presented vacancy clusters.

Species	E_f[a]	*Spin*	*Mag*[b]	*Sym*	*R1*[c]	*R2*	*R3*	*R4*	*R5*	*R6*
V_2	8.85	0	0.0	D_{3d}	2.66	2.66	3.07	3.07		
	8.60	0	2.1	C_{2h}	2.65	2.67	3.07	3.06		
	8.49	1	2.3	D_{3d}	2.65	2.65	3.07	3.07		
2C	10.86	0	0.0	C_{2h}	1.35	2.69	2.70			
	10.49	1	2.4		1.35	2.71	2.68			
	10.37	0	3.9		1.35	2.77	2.66			
	10.34	1	4.0		1.35	2.77	2.67			
2O	11.81	0	0.0	C_{2h}	1.39	2.85	2.77	2.70	2.75	
	11.76	0	2.0		1.39	2.84	2.77	2.65	2.75	
	11.59	1	2.4		1.40	2.80	2.78	2.70	2.72	
	11.55	0	3.3		1.40	2.80	2.77	2.68	2.72	
3C	12.07	0	0.0	C_{2v}	1.48	3.08	2.69	2.66	3.01	2.98
	11.50	1	3.8		1.48	3.08	2.65	2.74	3.00	3.00
1I	12.47	0	0.0	C_{2v}	2.57	2.70	2.65	2.65	2.51	
	12.12	1	2.5		2.59	2.69	2.62	2.72	2.52	
3E	13.20	0	0.0	C_s	1.50	1.53	2.49	2.73		
	12.42	1	4.4		1.49	1.52	2.50	2.77		
	12.35	2	4.6		1.50	1.51	2.51	2.72		
	12.23	1	5.5		1.51	1.51	2.53	2.76		
3A	13.46	0	0.0	C_s	1.51	1.51	2.49	2.69		
	12.29	1	5.5		1.50	1.49	2.49	2.63		
V_1[d]	13.10	0	0.0	D_{2d}	2.72	2.59	2.72	2.72	2.72	2.59
	12.34	1	2.9	C_{2v}	2.76	2.76	2.76	2.68	2.68	2.68
	12.13	0	3.0	T_d	2.73	2.73	2.73	2.73	2.73	2.73

[a]Energies are in eV. [b]Absolute magnetization; Bohr magnetons/unit cell. [c]Distances are in Å; see Figures 3-8 for a description of the parameters. [d]V_1 formation energies are multiplied by 2 for comparison.

convergency difficult. Table I summarizes the formation energies, spin states, and geometries of the vacancies of Fig. 1 and are listed in the ascending order of their spin-restricted formation

Monovacancy, $\mathbf{V_1}$

V_1 in diamond (Fig. 2) has been studied extensively both experimentally and theoretically. Removal of a single carbon from the ideal diamond lattice leaves four nearest neighbors separated by 2.52 Å with T_d symmetry and outward relaxation maintains this symmetry. The defect is identified[15] with GR1 absorption line at 1.673 eV arising from electronic transition between the ground ^1E state to a nearby ^3T excited state. Correctly modeling V_1 normally requires configuration interaction of competing multiplets, otherwise Jahn-Teller distortion is observed lowering the symmetry to D_2d or C_{2v} symmetry[16], as is the case in our spin-restricted calculation (Table I). We obtain a formation energy of 6.55 eV, a value that is between the representative LDA calculations [2] and a restricted open-shell Hartree-Fock method[16]. With spin- polarization, we find a T_d structure with a formation energy of 6.06 eV and a near-lying triplet state with the C_2v point group. Above 1100 K, V_1 is mobile and appreciably

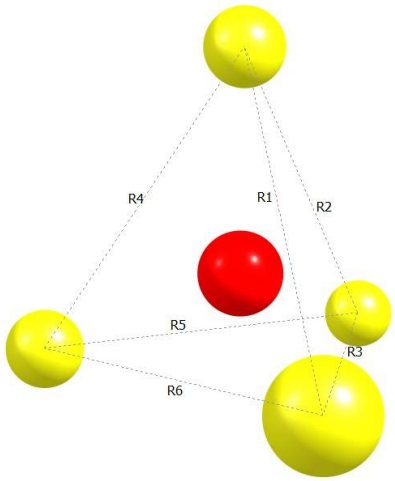

Fig 2. Nearest neighbors (yellow) to the monovacancy V_1. The vacancy removed is shown in red.

forms divacancies unless the diamond sample is rich in nitrogen which traps migrating vacancies[4]. Anderson et al. obtained a stabilization energy of 3.45 eV[17] using their semi-empirical quantum chemical method for the $V_1 + V_1 \rightarrow V_2$ process, which compares well with our calculated value of 3.55 eV.

Divacancy, **V_2**

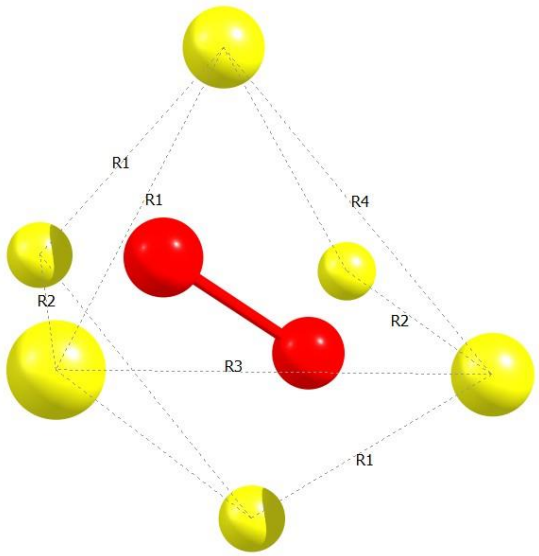

Fig. 3. The six nearest neighbors (yellow) to the divacancy (red).

The V_2 divacancy (Fig. 3) is created from removing two adjacent carbons in the diamond lattice leaving six nearest neighbors with D_3d symmetry. This leaves six states in the gap with the one electron description $a_{1g}^2 a_{1u}^2 e_u^2$ leaving the possibility of a Jahn-Teller distortion[12]. ESR experiments confirm the S = 1 ground state but with temperature dependent geometry; C_{2h} below 30 K and undistorted D_{3d} above this mark[4]. We calculate the restricted formation energy to be 8.85 eV which lowers by 0.36 eV when spin-polarization is introduced. Our calculation reveals D_{3d} symmetry and S = 1 spin with a C_{2h} unrestricted singlet state 0.11 eV higher.

Divacancy defect, **2C**

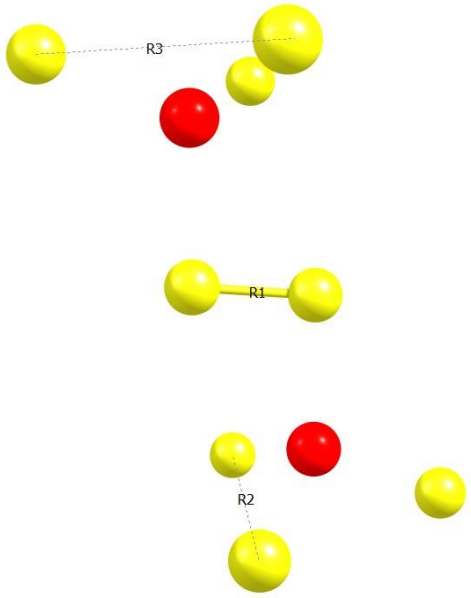

Fig. 4. Nearest neighbors (yellow) to the 2C divacancy (red).

The 2C defect (Fig. 4) is produced by removing a pair of carbon atoms separated by two along the [110] chain direction. Relaxation of the isolated pair along [110] produces a pyramidalized (~24°) sp^2 bond of 1.35 Å length which has a calculated characteristic C=C stretching frequency close to 1610 cm^{-1}.[18] This defect was considered by Twitchen et al. as it was ruled out as a possible explanation for the R4/W6 ESR center in irradiated diamond. We previously described[18] this defect modeling it with a hydrogen-terminated cluster and a 216 atom supercell with BLYP density functional and a numerical atomic orbital basis set. In contrast to that study, here we find an S = 1 ground state with a low-lying S = 0 diradical state; the results were reversed in our previous study. In both spin states, the spin density is located primarily on the six atoms that make up the two triangles that lie above and below the sp^2-bonded carbons. Migration of 2C to V_2 is high relative to 2O migration (see below) and thus may a stable trap for migrating vacancies and observable with ESR.

Divacancy defect, **2O**

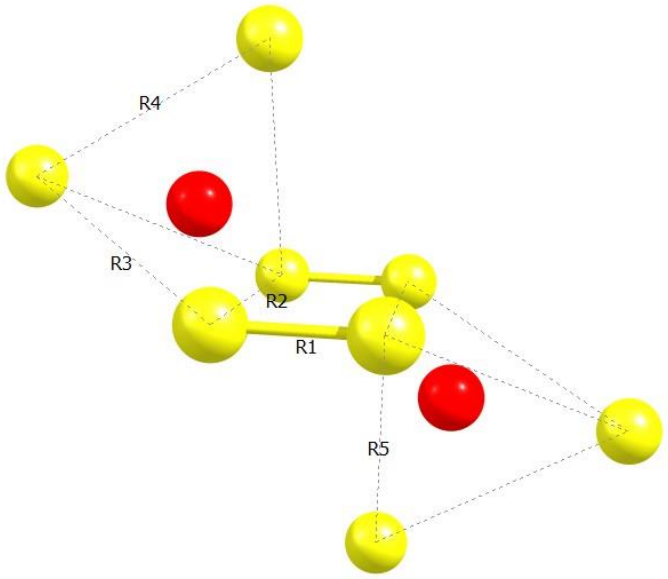

Fig. 5. Nearest neighbors (yellow) to the 2O divacancy (red).

Removing a pair of carbons situated at the opposite ends of a C_6 chair in the diamond lattice produces 2O defect (Fig. 5). Although removal of these atoms leaves behind two pairs of isolated nearest neighbors, as in 2C, these atoms are not as readily free to sp^2-hybridize because structural motive of these atoms are not situated along [110] and their bonded neighbors are twisted relative to each other, denying potential overlap. These carbons shrink to a distance of about 1.40 Å. The void space can be viewed as two closely interacting monovacancies and concerted migration of one quasi-sp^2 pair towards the void space produces the adjacent V_2. The simplicity of this path combined with the high cost of breaking the sp^2 bond in 2C make this the more favorable precursor to V_2 production. This is the only divacancy for which we find an S = 0 (unrestricted) ground state.

Divacancy defect, **3C**

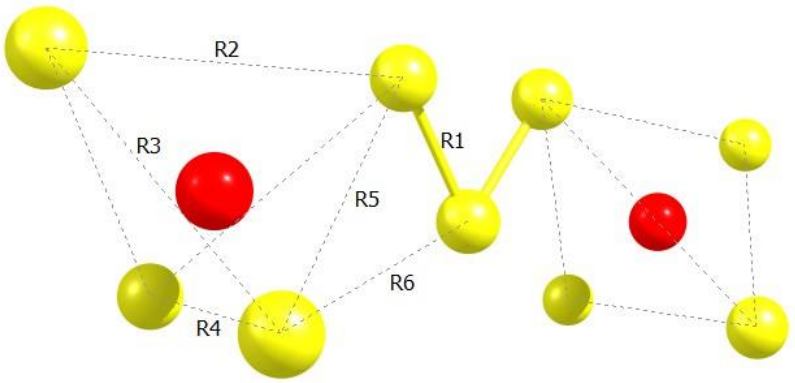

Fig. 6. The nearest neighbors (yellow) to the 3C divacancy (red).

The 3C (C for chain) defect (Fig. 6) is produced by removing a pair of atoms along [110] separated by three carbons. The two carbons along [110] that neighbor the vacancies relax towards their common neighbor shrinking their bond length to 1.48 Å. Concerted migration of these two atoms towards the void would produce the V_2 but we find this costly relative to the migration of a single atom towards one vacancy producing the [110] 2C divacancy.

Divacancy defect, **1I**

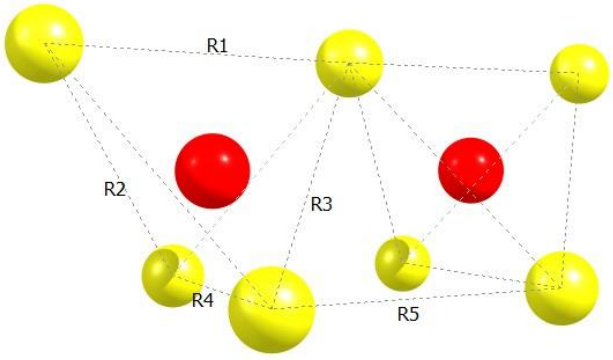

Fig. 7. Nearest neighbors (yellow) to the isolated divacancy 1I (red).

Early work by Coulson and Larkins[11] considered the 1I (Fig. 7) competitive with V_2. We achieve convergency on this structure for both spin-restricted and spin-polarized formalism but its formation energy is about 3.6 eV higher than V_2. NEB calculations for the 1I → V_2 process shows no barrier and we consider the 1I to be a transition structure for V_2 migration. This not only rules out one of the seemingly stable divacancy structures, but also limits the pathways of viable interconversion processes as we discuss below.

Divacancy defects, **3E and 3A**

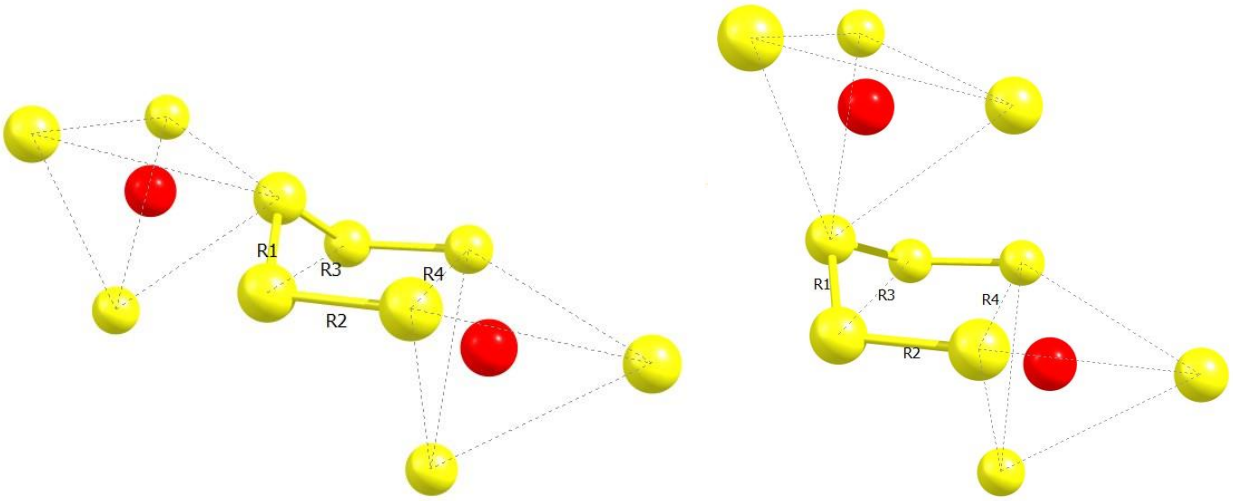

Fig. 8. 3E (left) and 3A (right) defects showing the nearest neighbors (yellow) surrounding the vacancies (red)

Starting with a C_6 chair, removing a carbon from the chair followed by the removal of a carbon separated by three atoms produces either the 3E or 3A defect (Fig. 8) depending on whether the axial or equatorial carbon is removed. 3E is shown (Table I) to be more stable but the difference is small and both are on accord with two isolated monovacancies. It is interesting then to note that even at this close of a distance the vacancies do not interact in an appreciable

way. Migration of the point carbon on the C_6 chair towards its respective equatorial or axial vacancy produces the 2O defect. Conversion of 3E or 3A to 3C is complicated due to structural constraints and therefore energetically unfavorable. One expects high barriers between structures in the three series due to the large atomic rearrangement that would be necessary for these transformations. The calculated barriers among 3A, 3E and 3C range from 5.0 eV to 7.5 eV, and are too high to consider these processes as viable. Therefore, once one of the three 3A, 3E or 3C structures has been formed, they should either dissociate or form either 2C or 2O.

Pathways

The results of our NEB calculations for transition structures and the related energetics are presented in Table II. The reaction energies are according to the direction of the written step, thus the negative values indicate all processes are exothermic. All NEB calculations were performed with RBPE and these results are shown on the first line for each step. The second line shows the estimated values taken spin-polarization into account. Thus, the reaction energy found in the second line is the difference between the reactive species' lowest formation energies, regardless of spin state and the barriers are estimated by taking the difference between the spin-polarized single point SCF energy of the (spin-restricted) transition structure and the calculated energy of the ground state of the reactant.

The formation of V_2 from 2O is a two atom migration where the bond of one of the isolated pairs breaks, with the atoms moving towards the 2O vacancy sites, leaving the void of V_2. The barrier is comparable to the V_1 diffusion barrier and proves the only viable path for the formation of V_2. A one atom migration was considered where one carbon on one of the two

isolated pairs moves towards a vacancy at the opposite end, however, the long distance traveled along this path induces a high barrier. Fig. 9 shows the integrated energy profile for V_2 production from 2O and 2C. One immediately notices the reduced barrier starting from 2O despite the extra stability the 2C possess.

TABLE II. Reaction energies and barriers for the elementary steps studied in this work. Energies are in eV. The first line in each step refers the spin-restricted calculations. The second line shows the values using spin-polarization.

Step	***Rxn E***	***Barrier***
3E -> 2O		
	-1.39	1.92
	-0.68	2.52
3A -> 2O		
	-1.66	1.61
	-0.74	2.33
3C -> 2C		
	-1.21	1.72
	-1.16	1.64
2C -> V2		
	-2.01	4.40
	-1.85	4.33
2O -> V2		
	-2.96	2.26
	-3.06	2.46

Moving backwards in the genealogy of Fig. 1, the integrated potential energy scan for the production of 2O from 3E and 3A are shown in Fig. 10. Both have similar and modest (spin-restricted) barriers of 1.92 eV (3A→ 2O) and 1.61 eV (3E→ 2O). This establishes a path from two free V_1 vacancies to V_2, first via 3A or 3E and then via 2O.

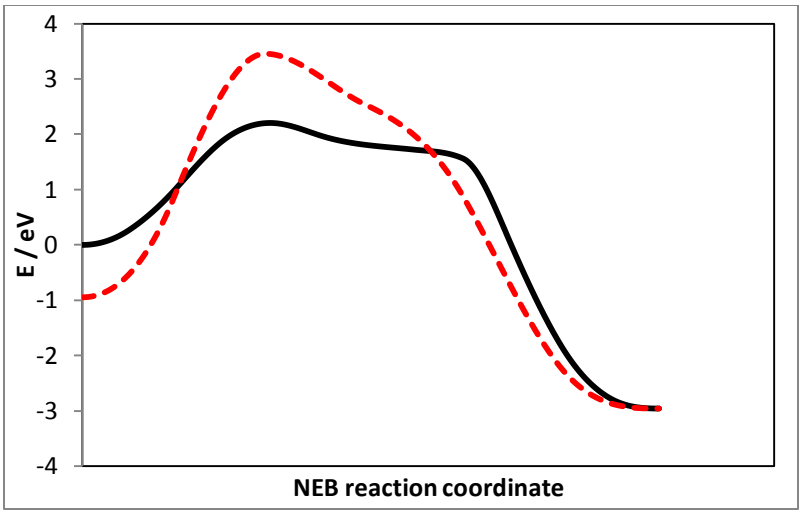

Fig 9. Energy profiles for the 2O → V_2 (black) and 2C → V_2 (dashed red) processes.

On the other hand, 3C (which is twice as likely to be formed on statistical grounds assuming all else being equivalent) can only be transformed into a trap, 2C (barrier = 1.72 eV), from which the barrier as discussed is too high to generate V_2.

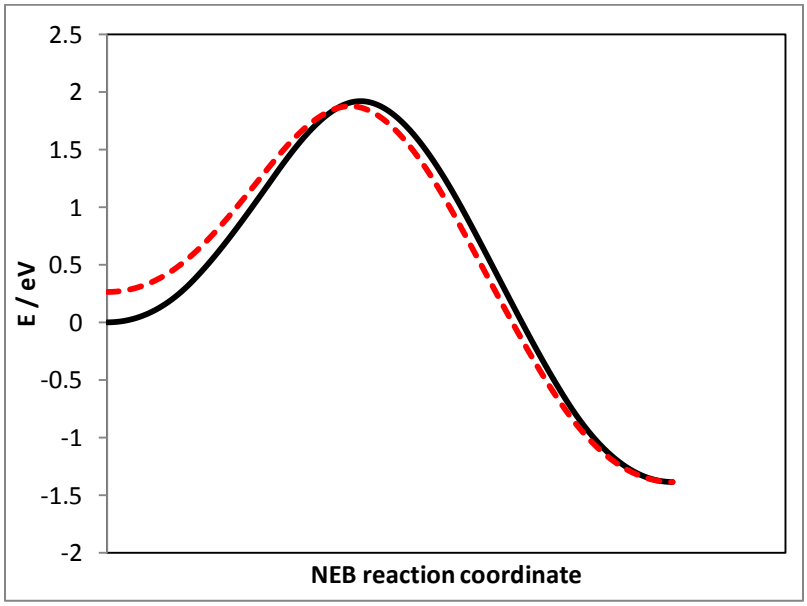

Fig. 10. Energy profile for the 3E→V_2 (black) and 3A→2O (dashed red) processes.

Some of the transition structures show interesting relaxations, such as in the case of 2O → V_2 where the transition structure (TS) contains a shortening of the quasi-sp^2 bonded pair which again elongates in the product. This transient shortening leads to a stabilization of the TS and lowers the barrier.

Fig. 11 summarizes the spin-polarized barriers for the processes discussed above. It is surprising that the process leading to the most stable end product, V_2, encounters barriers that are significantly higher than the barrier to the novel 2C structure with the C=C bond. Note that assuming a random initial structure the 3C is twice as likely to occur compared to the 3A and 3E. Therefore, we conclude that the product 2C should be observable in addition to the more stable V_2 divacancy.

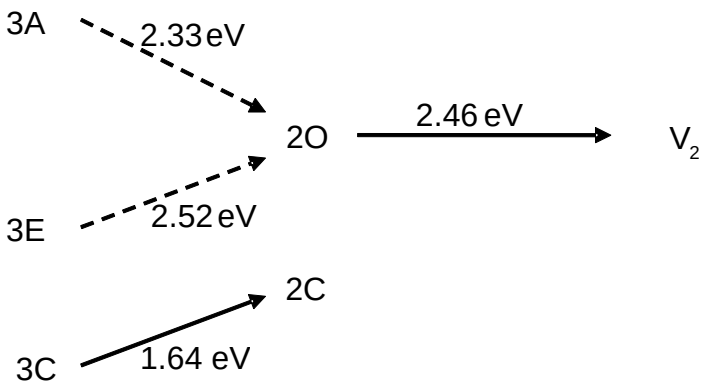

Fig. 11. Calculated spin-polarized energy barriers for the processes discussed in this paper. V_2 is more stable than 2C [V-C=C-V] by about 1.85 eV, but given the smaller barriers leading to 2C, it may be more prevalent than V_2. (Position of symbols does not represent relative energetics.)

6. Conclusions

We have shown with DFT computations that the capture of one monovacancy, V_1, by another can lead to a stable divacancy V_2 and alternatively to a more complex novel 2C isolated divacancy [V-C=C-V] structure, which would trap the two monovacancies in a stable state. Computational modeling indicates that the mechanism of the formation of these bound vacancy clusters is likely to occur via the 2O intermediate, while the chain-like intermediate is stabilized by the formation of a double bond creating a stable divacancy trap. The computed series of barriers indicate that the novel 2C isolated divacancy [V-C=C-V] should be produced in the process of monovacancy diffusion *in addition to* the more stable divacancy, V_2. The new structure of the isolated divacancy shows that the eight dangling bonds of a divacancy can relax not only as the nearest neighbor adjacent divacancy, but in a manner creating an approximate double bond inside of diamond.

We also concluded that 1I (the divacancy separated by one carbon) is not a stable structure, similarly to the case of silicon, where Hwang and Goddard have pointed[19] out the instability of such as structure toward a V_2. Given the well-known differences[12, 20] between Si and diamond; this similarity does not follow automatically.

Acknowledgements. Research is supported by the U.S. Department of Energy, Office of Basic Energy Sciences, Division of Materials Sciences and Engineering under Award No. DE-FG02-07ER46472. Support by GridChem is acknowledged for computer time. We are indebted to Prof. Yury Gogotsi and Dr. Vadym Mochalin for useful discussions.

References

[1] J.M. Baker, Deducing atomic models for point defects in diamond: The relevance of their mechanism of formation, Diamond Relat. Mater. **16**, 216 (2007).

[2] J. Bernholc, A. Antonelli, T.M. Del Sole, Y. Bar-Yam, and S.T. Pantelides, Mechanism of self-diffusion in diamond, Phys. Rev. Lett. **61**, 2689 (1988).

[3] B. Butorac, and A. Mainwood, Theoretical study of migration processes in bulk diamond, Diamond Relat. Mater. **17**, 1225 (2008).

[4] D.J. Twitchen, M.E. Newton, J.M. Baker, T.R. Anthony, and W.F. Banholzer, Electron paramagnetic-resonance measurements on the divacancy defect center R4/W6 in diamond Phys. Rev. **B 59**, 12900 (1999).

[5] J.M. Baker, D.C. Hunt, M.E. Newton, and D.J. Twitchen, Centres involving two vacancies in diamond Radiat. Eff. Defects Solids **149**, 233 (1999).

[6] Quantum ESPRESSO is a community project for high-quality quantum-simulation software, based on density-functional theory, and coordinated by Paolo Giannozzi. See http://www.quantum-espresso.org and http://www.pwscf.org.

[7] J.P. Perdew, K. Burke, and M. Ernzerhof, Phys. Rev. Lett., **77**, 3865 (1996).

[8] G. Henkelman, B.P. Uberuaga, and H. Jonsson, A Climbing image nudged elastic band method for finding saddle points and minimum energy paths, J. Chem. Phys. **113**, 9901 (2000) .

[9] See http://www.physics.rutgers.edu/~dhv/uspp/uspp-cur/Work/006-C/006-C-gpbe--bm/

[10] T.A. Halgren, and W.N. Lipscomb, Synchronous-transit method for determining reaction pathways and locating molecular transition-states, Chem. Phys. Lett. 49, 225 (1977).

[11] C.A. Coulson, and F.P. Larkins, Electronic structure of the neutral isolated divacancy in diamond, J. Phys. Chem. Solids. **30**, 1963 (1969).

[12] B.J. Coomer, A. Resende, J.P. Goss, R. Jones, S. Oberg, P.R. Briddon, The divacancy in silicon and diamond, Physica **B 273**, 520 (1999).

[13] S.J. Breuer, and P.R. Briddon, Ab-intio investigation of the native defects in diamond and self-diffusion, Phys. Rev. B. **51**, 6984 (1995).

[14] G. Davies, S.C. Lawson, A.T. Collins, A. Mainwood, and S.J. Sharp, Vacancy-related centers in diamond, Phys. Rev. **B46**, 13517 (1992).

[15] C.D. Clark, R.W. Ditchbum, and H.B., Dyer, Proc. R. Soc. **234**, 363 (1956).

[16] S.S. Moliver, An Open-shell method for neutral vacancy in silicon and diamond, Phys. Sol. State. **42**, 655 (2000).

[17] A.B. Anderson , E.J. Grantscharova, and J.C. Angus, Molecular-orbital theory of monatomic and diatomic substitutional defects as shallow n-type dopants in diamond, Phys. Rev. **B 54**, 14341 (1996).

[18] D. Hyde-Volpe, B. Slepetz, and M. Kertesz, The [V-C=C-V] divacancy and the interstitial defect in diamond: Vibrational properties, J. Phys. Chem. **C 114**, 9563 (2010).

[19] G.S. Hwang, W.A. Goddard III, Diffusion and dissociation of neutral divacancies in crystalline silicon, Phys. Rev. **B 65**, 233205 (2002).

[20] In carbons both sp^2/sp^3 hybridizations play an important role, as opposed to Si.

CHAPTER 6

THERMAL [4+4] CYCLOADDITION OF [2.2](9,10)ANTHRACENOPHANE*

Abstract

We show that the reaction path connecting the tethered [2.2] (9,10)anthracenophane and its photodimer proceeds step-wise via a diradicaloid transition state where one σ–bond is made before a second. The newly found transition state (TS) has a smaller molecular volume than either the reactant or the product giving an atomistic explanation to the recently found pressure catalyzed barrier lowering and rate enhancement. The density functional methods used include long-range contributions as required in a system where the dispersion interactions are significant. We discuss this transformation in the context of the diamond-to-graphite transition owing to the similarity of σ–bond breakage into a delocalized π-system. We also comment on the controversy surrounding the equilibrium geometries of photoisomerized cyclophanes, concluding that D_{2h} symmetry in the photoisomer of the title molecule is a transition structure connecting a pair of degenerate ground state D_2 geometries.

Introduction

In a surprising experiment[1] Jezowski et al. showed that the application of mechanical pressure significantly reduces the barrier for the thermal cycloaddition of [2.2] (9,10)anthracenophane (Scheme 1). In Zeonex (polycycloolefin) polymer matrix, the activation energy for the dissociation of the photoisomer was reduced from 93 kJ mol^{-1} at ambient pressure to 7 kJ mol^{-1} under 0.9 GPa applied pressure. Typically much higher pressures around 10-20

* Reproduced with permission from B. Slepetz and M. Kertesz; in submission: J. Am. Chem. Soc.

GPa[2,3,4] are needed to break bonds and generally negative activation volume signals bond formation and not bond breaking as discussed by Jezowski et al.[1] The authors hypothesized that the transition structure that connects the title compound with its photoisomer would show a smaller molecular volume than either equilibrium structure. Here were explore the potential energy surface of the thermal cycloaddition reaction to answer the question: Is there a transition structure (TS) or intermediate to be found on the potential energy surface that can provide an atomistic interpretation for this new experimental result?

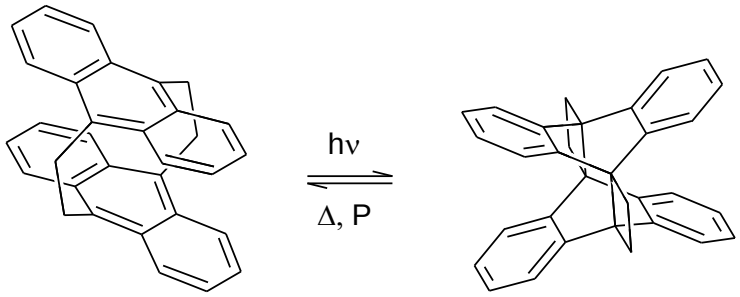

Scheme 1. The [4+4] cycloaddition of [2.2] (9,10)anthracenophane. The reaction is reversible under ambient conditions and the reverse reaction is catalyzed by pressure[1].

A second motivation for finding an accurate reaction path for this reaction derives from the interest in interatomic contacts between carbon atoms in the range of 1.7-2.8 Å. These contact values are uncommon but not unprecedented[5] and continue to attract interest[6]. Note, that the X-ray crystal structure data for the title compound and its photoisomer show that the critical CC contacts are[7] d(1-2)=2.765 Å and d(1-2)=1.653 Å, respectively. One of the motivations of this study is to see whether a reaction intermediate can be identified with CC contacts closer to the "forbidden" 2.0-2.5 Å range.

Special structural and electronic peculiarities[8] such as strain, steric hindrance, ionic charge, and radical character are necessary to generate long CC bonds >1.65 Å or short CC contacts <2.9 Å. Electron deficient carbocations are known[9,10] to interact with electron rich π-

bonds to form a three-center, two electron homoaromatic bond with CC distances in the 1.6-1.75Å range as in **1**[11]. Neutral sp^3-sp^3 bond lengths >1.7 Å have been observed in benzocyclobutane derivatives[12], as in **2**. Here, the steric crowding of the phenyl groups forces the respective CC bond to a greater distance where a long σ-bond is preferred over a diradical state. 1,1,2,2-tetraarylpyracene (**3**) has a long CC σ-bond with two distinct distances, 1.71 Å and 1.78 Å, due to two crystallographically independent molecules in the unit cell[13].

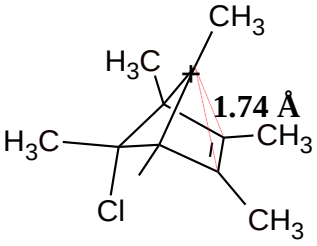

1

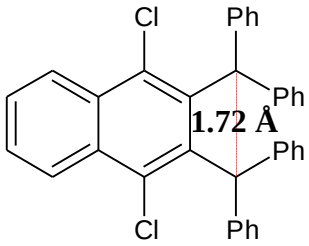

2

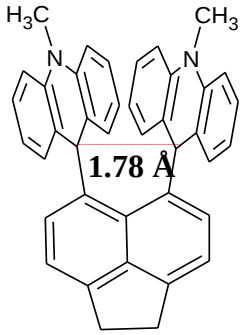

3

Paracyclophanes, another example containing unusual CC distances, are of chemical interest due to their unconventional structures and photoisomerization reactivities[14,15]. Applications in the fields of chiral catalysis[16,17], electronic materials[18] and optical switches[19] have broadened this interest. Structural anomalies in paracyclophanes include nonplanar distorted aromatic rings and unusual distances between sp^3-hybridized carbons. While the structure of paracyclophanes has been studied experimentally[20,21,22,23] and theoretically[24,25,26,27,28,29] with a variety of methods, the reaction paths of photoisomerization have been largely ignored. [2.2] (9,10)anthracenophane (**4**) can form a photodimer (**5**) through an intramolecular [4+4] cycloaddition (Figure 1) in which the central aromatic rings

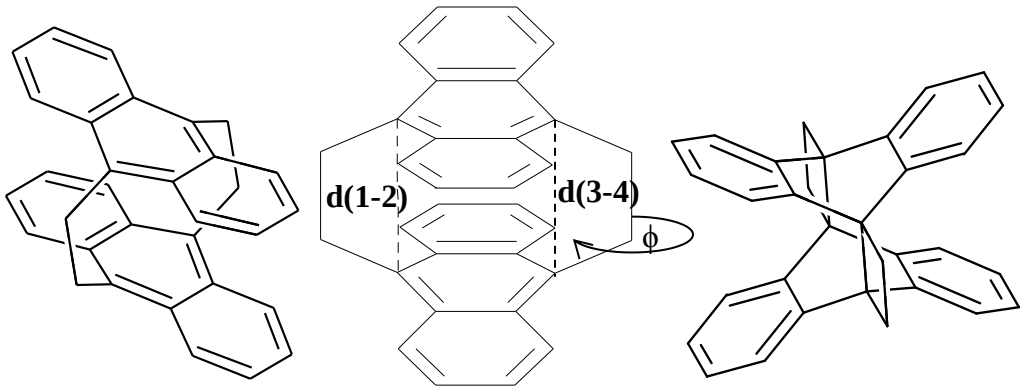

4 **5**

Figure 1. [2.2] (9,10)anthracenophane (left, **4)** with the distance d(1-2)/d(3-4) labeled (center) that undergoes the greatest geometrical change during isomerization. The photodimer **5** is shown at right. The torsion ϕ correlates with d(1-2) and may be parallel or twisted relative to the torsion on the opposite side.

connect via sp^2-sp^3 transition. Other photodimers, of the Diels-Alder [4+2] variety, might be formed under high pressure without photoexcitation.[30] We also note the analogy of cycloaddition to the diamond-to-graphite transition; as the paracyclophane undergoes intramolecular isomerization, the distance d(1-2) (Figure 1) decreases, breaking the aromaticity of the connecting rings, forming an elongated electron pair σ-bond.

[2.2] (9,10)anthracenophane is of particular interest because the anthracene unit, with its three aromatic rings, can aid in the stabilization of intermediate structures during photoisomerization. **4** isomerizes to **5** in a thermally forbidden, photochemically allowed [4+4] cycloaddition (Scheme 1). The reverse, bond dissociative reaction (**5** → **4**) can be accelerated by hydrostatic pressure leading to the notion that the TS has a smaller volume than the photoisomer **5** or the clamped bisanthracene **4.**[1] This study presents the computational modeling for the reverse **5** → **4** because the experimental data refer to this dark reaction[1].

X-ray data indicate that **4** (CSD refcode: ANTMET05[7]) has d(1-2)=2.765 Å and **5** (CSD refcode: ANTMEU03[7]) has d(1-2)=1.653 Å. As cycloaddition proceeds, the central ring

transforms from a nearly planar sp^2-hybridized aromatic system to a nonplanar system with d(1-2) bonding two sp^3-hybridized carbons. This process spans the distances that are encountered as graphite is compressed into diamond. We will present two pathways for the ground state photoisomerization of [2.2] (9,10)anthracenophane and discuss these in the context of the diamond-to-graphite transformation. We have explored the potential energy surface (PES) and find detailed information for two competing pathways that involve the breaking of the d(1-2)/d(3-4) pair of bonds: one in which they break in synch and another where one pair breaks before the other.

Methodology

All molecular calculations were performed with the Gaussian 09[31] suite using the M06-2x[32] and Grimme's B97D[33] density functionals paired with various Gaussian split-valence[34] basis sets. The accuracy of the M06-2x model chemistry applied to reproducing the geometric parameters of small paracyclophanes was previously demonstrated by Bachrach[29] using the split-valence triple-zeta basis 6-311G(d,p). Quenneville and Germann used extensive DFT calculations with 6-31G(d) for exploring the potential energy surfaces of benzene and anthracene dimers under pressure.[30] Our test calculations with the 6-31G(d,p) basis set on **4** and **5** showed minute geometrical changes with distances within 0.001 Å. The difference in ΔE between these species from the 6-311G(d,p) basis to the smaller 6-31G(d,p) was 0.2 kcal mol^{-1}. We therefore use the smaller basis set in this work. M06-2x and B97D was chosen because medium range electron correlation effects are important for interacting conjugated substructures. Energy minima and maxima were confirmed through vibrational analysis ensuring only real frequencies for minima and exactly one imaginary frequency for transition structures. Transition structures

were searched for by quadratic synchronous transit[35] (QST) and were connected to energy minima by following the amplitude of the imaginary frequency as implemented in the intrinsic reaction coordinate[36] (IRC) method. Molecular volumes were calculated from the electron density by the method described by Wong et al.[37] in which the volume is defined as that within a 0.001 electron/Bohr^3 contour, estimated with a Monte Carlo integration. A total of 100 iterations were used with the number of integration points per cubic bohr chosen to obtain a total of approximately 10,000 integration points, as demonstrated in previous studies[1,38].

For solid state calculations, the augmented plane wave electronic structure code PWscf—part of the Quantum ESPRESSO[39] package—was used to perform self-consistent field (SCF) total energy calculations on the rhombohedral structures. We use the exchange correlation functional of Perdew et al. (PBE)[40]. The structure is defined by three independent parameters as shown in Figure 2: the interlayer separation q, unit cell length a, and the inter-axes angle α. The values of these parameters are what determine the in-plane bond length r and the inter-layer angle θ. The diamond and graphite structures were fully optimized such that the atoms and cell parameters were permitted to relax to minimize the energy. Note that due to the lack of long-range dispersion in the PBE functional, the interlayer interactions at the graphite end are not well represented. All other structures along the path were constructed with the separation of the atoms q taken as a given starting point and the cell parameters a and α were varied until a local minimum was obtained. The optimized parameters for diamond, graphite, and the transition state are summarized in the supporting information. For all calculations, the kinetic energy cutoff of the plane waves was 48.0 Ry with a charge density cutoff of 348 Ry. Electron SCF convergency was set at 10^{-8} within a 16x16x16 Monkhorst–Pack Brillion zone sample grid, and Fermi-Dirac electron smearing of 10^{-3} Ry was used. A Vanderbilt ultra-soft pseudopotential,

parameterized for small organic molecules by Meyer[41] was used to treat the carbon core electrons. For the full geometric optimizations, convergency was satisfied when the total energy change between successive steps was less than 10^{-7} E_H and the components of all the forces on the atoms were reduced below 51 meV/Å.

Diamond-to-graphite transition

The modeling of the diamond-to-graphite transition is simplified[42,43] when using a two atom rhombohedral cell in which the first carbon atom lies at the origin at a distance *q* from the second carbon, aligned along the z-axis. This cell allows a smooth transition from diamond to ABC graphite and is described (Figure 2) by three parameters: the in-plane bond length *r*, the interlayer distance *q*, and the interlayer angle *θ*. Ideal diamond has $q=r=1.54$ Å with $\theta=109.5°$. As *q* increases towards graphite, *r* decreases as π-electron delocalization develops.

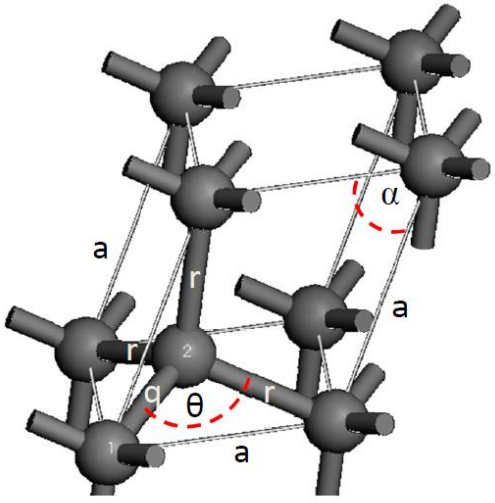

Figure 2. Schematic representation of the parameters involved in the diamond-to-graphite transition. *r* is the in-plane bond length, *q* is the interlayer separation, θ is the interlayer angle.

Table S1 contains the parameters as calculated in this work for diamond, graphite, and the structure with highest energy along the synchronous transition. Figure 3 shows the energy

profile for the diamond-to-graphite transition as a function of *q*. The transition structure is at *q*=2.06 Å with *r*=1.47Å and θ=102°. Unrestricted formalism at this geometry did not lower the energy as neither a spin-triplet or diradical state were found. This point is worth discussing further. The lack of splitting of α and β orbitals is an indication that instead of developing localized spins when the σ-bonds break, the system gains energy by forming delocalized π-like orbitals. Given the pyramidalization angle of θ =102° it is not surprising that the electronic structure undergoes a rearrangement without such a spin symmetry breaking. Typically, larger exact exchange component in a hybrid DFT leads to a wider range of geometrical parameters with spin symmetry breaking. The maximum propensity to such broken symmetry solutions occur with 100% exact exchange at UHF. After extensive efforts we found such a symmetry broken solution with UHF only with a minimal energy lowering of 0.9 kcal mol^{-1} at *q*=2.1 Å. This finding explains why at the PBE level we find no broken symmetry solution in the graphite-to-diamond transition.

The geometry at the TS along the graphite to diamond path discussed here is characterized by geometrical parameters that are not unexpected for transition between a σ-bond and simultaneous delocalization of the resultant radical electrons into a delocalized π-electron system. Therefore, it is instructive to see how the various geometrical parameters change during this transformation which will serve as a basis of comparison for the valence isomerisation of the title compound. Figure 3 shows the energy profile for the diamond-to-graphite transition as a

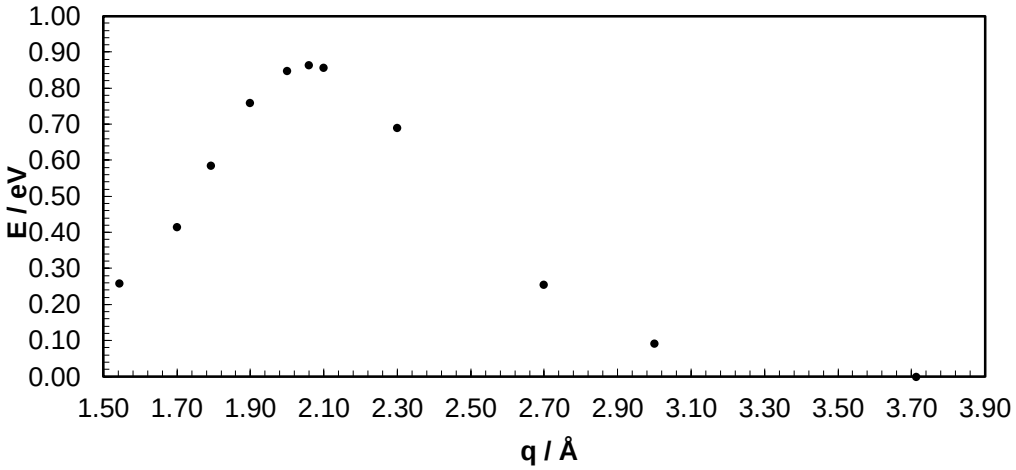

Figure 3. Relaxed scan of the total energy per unit cell for the diamond-to-graphite transition along the inter-planar distance *q* using DFT band theory. The transition structure (TS) is at *q*= 2.06 Å.

function of *q* where it is observed that the activation energy is about 0.6 eV/unit cell. This is only about 15% of the bond dissociation energy observed in CC σ-bonds in typical organic molecules[44], highlighting the importance of delocalization in stabilizing bond breakage.The geometrical relaxation confirms this process. In figure 4, the in-plane bond length is plotted against *q*. Likewise, in figure 5 the interplane angle θ is plotted against q. Both curves show a smooth transition from the sp^3-hybrid parameters of 1.54 Å and 109.5° to the sp^2-hybrid parameters of 1.41 Å and 90° indicating that as the π-bonds develop parallel to the σ-bonds being broken. While the graphitic layers are still quite corrugated at the TS (θ=102°) the in-plane bonds *r* are more than half-way at their final graphitic values.

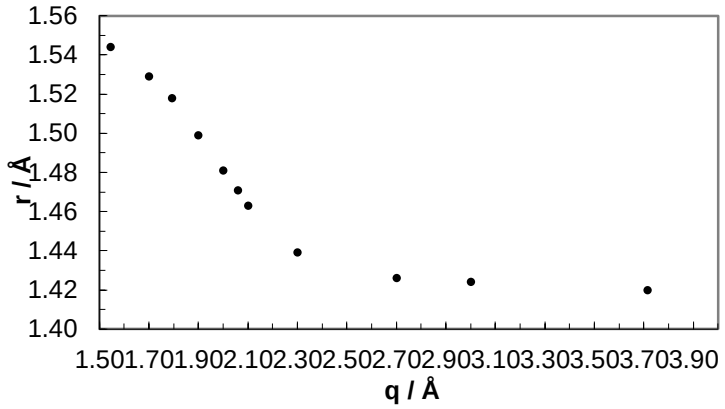

Figure 4. Change in the in-plane bond length *r* with interlayer separation, *q*. Data correspond to the relaxed scan in Figure 3.

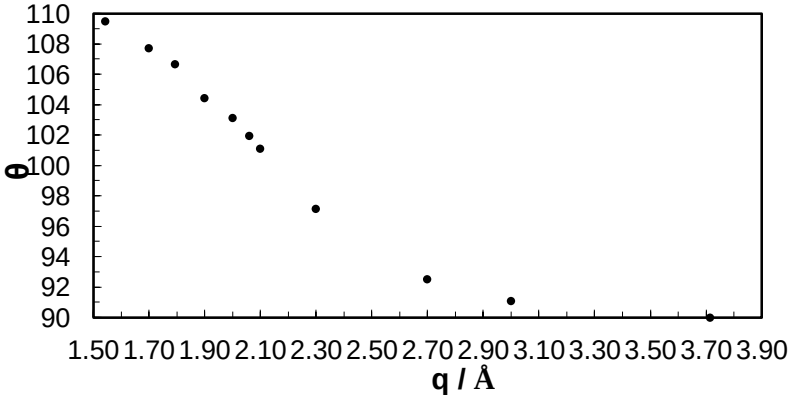

Figure 5. Change in the inter-plane angle θ with inter-planar distance *q* for the diamond-to-graphite transition. Data correspond to the relaxed scan in Figure 3.

Valence tautomers and conformers of the Cyclophane [2.2] (9,10)anthracenophane

The energies and geometries of five relevant conformers and tautomers involved in the cycloaddition of [2.2] (9,10)anthracenophane are summarized in Table 1 for two model chemistries. In both models, the relative energies of the species follow the same order and the difference between the D_2 dissociated tautomer (**4a**) and its conformer, the crystallographically observed C_2 structure (**4b**), is less than 1 kcal mol^{-1}. The largest difference between the two methods is the calculated dissociation reaction energy (**5a**-to-**4a**), which is exothermic at -9.11

kcal mol^{-1} in M06-2x/6-31G(d,p) and -21.2 kcal mol^{-1} in B97D/6-31+G(d). The B97D model is closer to the exothermic heat of reaction experimental value[45], as measured by differential scanning calorimetry, of -35 to -39 kcal mol^{-1}. However, M06-2x better predicts the reaction barrier energy (see text below).

Figure 6, illustrates the relevant CC distances that undergo the greatest change are d(1-2) and d(3-4).

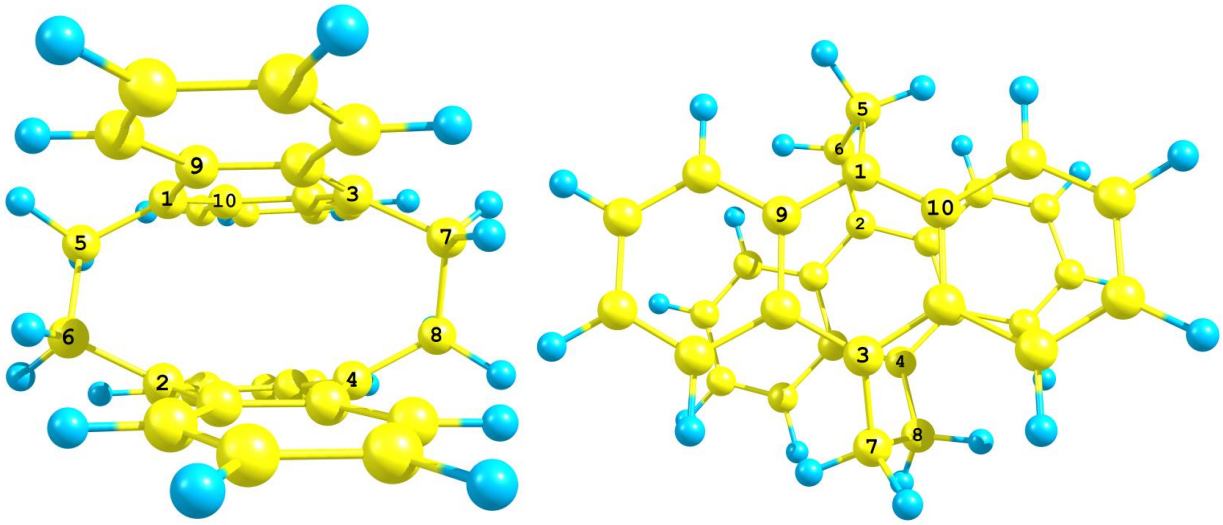

Figure 6. Two views of **4**. d(1-2) and d(3-4) undergo the greatest change during isomerization to **5**. The torsional angles ϕ(1-5-6-2) and ϕ(3-7-8-4) also change significantly.

Where these distances are unequal, d(3-4) will refer to the longer of the two. For both model chemistries, the global minimum is found to have D_2 symmetry (**4a**) whereby the torsional angles of the bridging carbons twist relative to one another. An isomer with C_2 symmetry (**4b**)—observed with X-ray crystallography[7,46,47]--is found to be less than 1 kcal mol^{-1} above **4a** (See supporting information Figure S4). We found a transition structure linking these torsional isomers (not pictured) that is energetically 1.35 kcal mol^{-1} above **4a**.

Table 1. Relative energies and relevant geometric parameters for the molecular species presented in this work.[a]

DFT		M06-2x/6-31G(d,p)			B97D/6-31+G(d)		
Species	Symm.	Energy	d(1-2)	ϕ(1-5-6-2)	Energy	d(1-2)	ϕ(1-5-6-2)
4a	D_2	0	2.802	33.5	0	2.823	32.9
4b	C_2	0.75	2.814	20.5	0.43	2.826	19.5
5a	D_2	9.11	1.645	17.5	21.2	1.688	16.9
5b	D_{2h}	13.8	1.645	0.2	24.5	1.689	0.0
6[b]	C_2	36.9	1.692 2.626	17.4 35.1	36.8	1.814 2.609	17.5 32.4

[a] Energies in kcal mol^{-1}, distances in Å, angles in °. [b]Energy minimum in M06-2x, TS in B97D.

The crystal structure[7,47,48,49,50] of the cycloaddition product, 9,9':10,10'-diethano-9,9':10,10'-bi-9,10-dihydroanthracene, has D_{2h} symmetry (**5b**) but we find this geometry to be 5 kcal mol^{-1} higher than a structure possessing D_2 symmetry (**5a**) (See supporting information Figure S5). The equilibrium geometry of smaller cyclophanes has been has been the subject of debate[27,51,52] with X-ray diffraction data indicating a D_{2h} geometry for [2.2]paracyclophane with no twist. We find the D_{2h} structure to be a first-order saddle point on the PES connecting two degenerate D_2 isomers as the carbon bridges twist relative to each other.

We also find a local minimum in M06-2x that has not been described before: it has broken-symmetry (BS, **6**) (Figure 7) with intermediate and unequal CC distances d(1-2)=1.69 Å , d(3-4)=2.63Å. The BS tautomer ground state is a diradical with spin density localized on the

long CC atoms and the only example we have found of a stationary point having a spin-unrestricted solution as all other species have closed shells. Structure is **6** key in understanding the full potential energy surface and it corresponds to one of the bonds being broken while the other is stretched only slightly to be discussed in the next section. A triplet ground state is competitive, calculated to be higher in energy by 0.6 kcal mol^{-1} which should be contrasted with the calculations by Quenneville and Germann[30] who found for the dimerization of untethered anthracene under high pressure that the triplet path is lower than the singlet path for the asynchronous transit but overall the synchronous transit ends up being the lower barrier path.

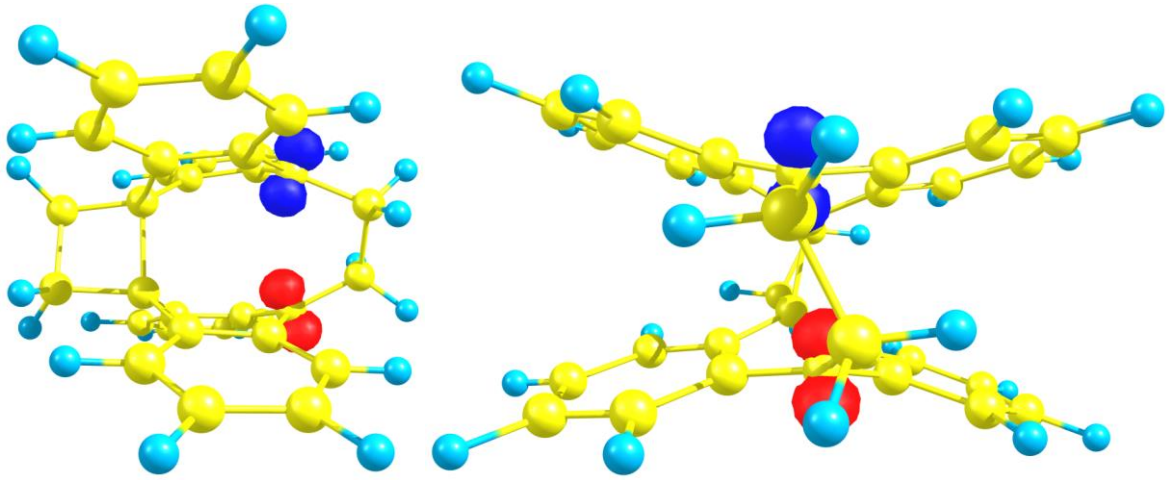

6

Figure 7. Two views of the broken-symmetry (**6**) tautomer at the M06-2x/6-31G(d,p) level showing where the bulk of the spin density is located at the long carbon-carbon contact sites. d(1-2) = 1.69 Å (shown as a bond), d(3-4)=2.63 Å joins the radical sites.

Pathways

We have calculated two PESs for the thermal cycloaddition transition, monitoring the changes in geometry, energy, and spin density (where applicable) to compare with the graphite-to-diamond transition. We start with a synchronous path in which d(1-2)=d(3-4) along all points

of the reaction. As shown in Figure 8, the cycloaddition transition proceeds through a (left-to-right) barrier of 38 kcal mol^{-1} and is exothermic with reaction energy of 9 kcal mol^{-1} in M06-2x/6-31G(d,p) model chemistry. All points along the path have closed shells except for the maximum at d(1-2) = 2.20 Å. A spin-restricted single point energy calculation for this geometry is 9.95 kcal mol^{-1} higher.

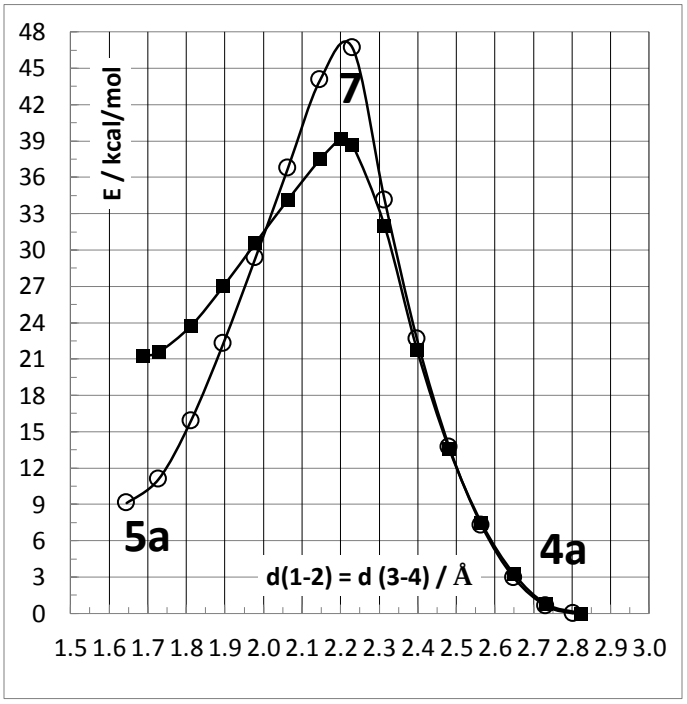

Figure 8. Total energy along the synchronous path for the cycloaddition of [2.2](9,10)anthracenophane at the UM06-2x/6-31G(d,p) (circles) and UB97D/6-31+G(d) (squares) levels.

Vibrational analysis on the maximum energy structure **7** (Figure 9) reveals two imaginary modes: one with synchronous displacement among the pair of long carbon contacts and another that stretches the carbon contact pairs asymmetrically towards a structure that resembles the BS species **6**. In B97D/6-31+G(d), the barrier is reduced due to a lower total energy for the transition state and a greater exothermic difference between equilibrium species.

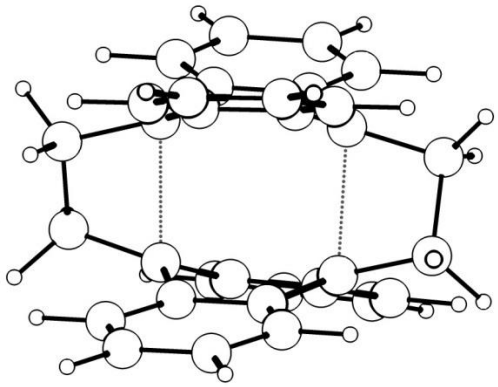

7

Figure 9. The structure of the second-order saddle point calculated for the synchronous path with d(1-2) = 2.20 Å at the M06-2x/6-31G(d,p) level. Dashed lines indicate the short contacts between d(1-2) and d(3-4).

Figure 10 shows the change in the distances d(1-9) and d(1-10) calculated with M06-2x/6-31G(d,p) along the synchronous path, which are analogous to the in-plane bond length *r* in the diamond-to-graphite transition. In the latter case there is only one distance value with all in-plane bonds being equivalent. For each distance, two nearly close correlations are observed around the transition structure. Likewise, Figure 11 depicts the changes in angles θ(9-1-2) and θ (10-1-2) that are analogous to the diamond-to-graphite interplane angle. Here we find two different types of angles with θ(10-1-2) spanning 103°-120° while θ (9-1-2) is more analogous to the sp^3/sp^2 diamond-to-graphite transition, following close correlation between 91°-107°.

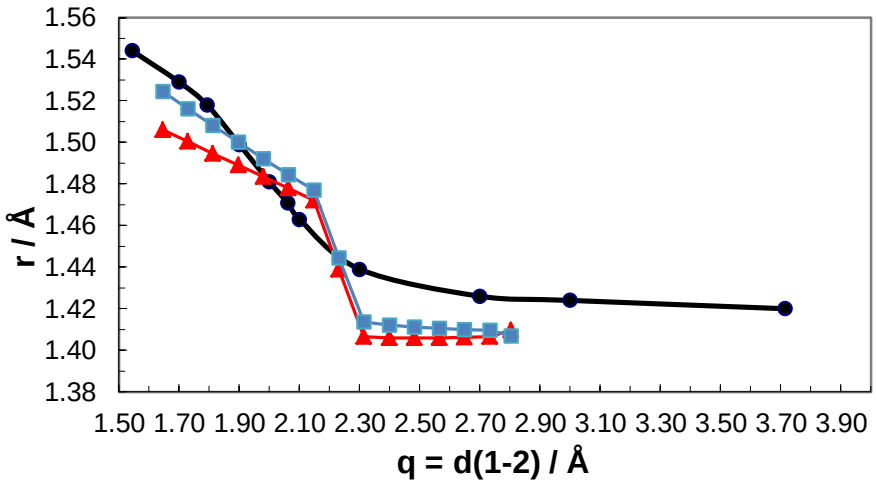

Figure 10. Change in the in-plane bond length *r* as a function of the interplane distance *q* in the diamond-to-graphite transition (black circles) overlaid with the analogous bond lengths in the synchronous transition of **5a** to **4a**. Blue squares refer to d(1-9), red triangles refer to d(1-10).

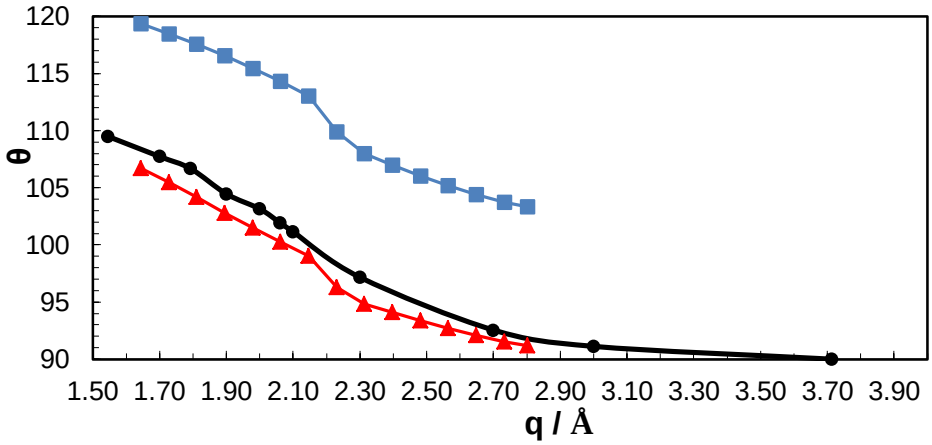

Figure 11. Change in the interlayer angle θ as a function of interplane distance *q* in the diamond-to-graphite transition (black circles) overlaid with the change in the analogous pair of angles in the synchronous transition of **5a** to **4a**. Blue squares refer to θ(10-1-2), red triangles refer to θ(9-1-2).

We now consider the possibility of a pathway where d(1-2) changes asymmetrically, that is, one bond forms in the cycloaddition before the other. Figure 12 shows such a pathway in (d(1-2), d(3-4)) space based on our two model chemistries. For M06-2x, the asymmetric path passes through two transition states that flank a very shallow local minimum, **6** (BS). TS1 connects **5a** to **6** and lies just 0.2 kcal mol^{-1} above **6**. TS2 connects **6** to **4a** and is 2 kcal mol^{-1}

above **6**. In B97D, the equilibrium structures are connected by single TS with no intermediate. It is an essential feature of this reaction, that the lower barrier path in both model chemistries proceeds through a region close to structure **6** pointing to a stepwise process.

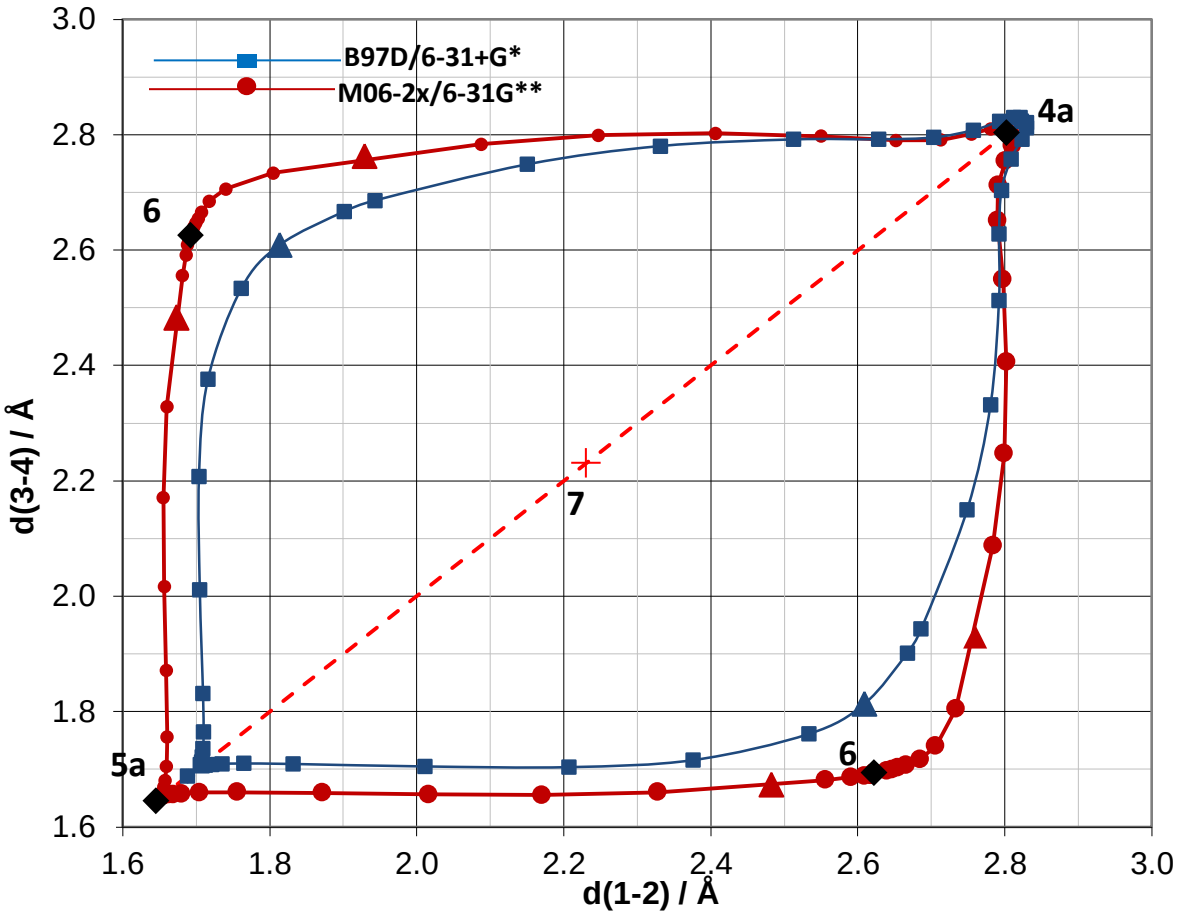

Figure 12. PES of the cycloaddition of [2.2] (9,10)anthracenophane with the two model chemistries used in this work in (d(1-2),d(3-4)) space. Red circles follow the asynchronous path as calculated with UM06-2x/6-31G(d,p), blue squares follow the path calculated with UB97D/6-31+G*. Triangles indicate transition structures and diamonds indicate minima. The red dashed line follows the synchronous path with the + indicating the location of the second order saddle point found in M06-2x/6-31G(d,p).

Figure 12 shows the variation in the parameters d(1-2)/d(3-4) for both model chemistries. Starting at the equilibrium photoisomer **5a** at the M06-2x level (red circles) we see that d(1-2) begins relatively unchanged keeping a (long) σ-bond while d(3-4) breaks until the first transition structure (red triangle) when d(1-2) begins to break appreciably. The path continues passing

through a shallow minimum **6** with d(1-2) still bonded, then through a second transition structure, before arriving at the dissociated **4a** tautomer. The dashed red line follows the synchronous path with d(1-2)=d(3-4) which produced the energy profile given in Figure 8.

The full spin-unrestricted PES along the IRC for both models is shown in Figure 13. In M06-2x/6-31G(d,p), the reaction barrier of 28 kcal mol^{-1} compares favorably to the measured value of 24.0 kcal mol^{-1} in toluene solution[45] and 22.2 kcal mol^{-1} in polycycloolefin polymer matrix[1], overshooting by 4-6 kcal mol^{-1}. The B97D/6-31+G(d) IRC model undershoots the experimental reaction barrier by 7-9 kcal mol^{-1}. The PES displays a diradicaloid character[53] in a narrow range at the BS (**6**) structure corresponding to one broken σ-bond as indicated by the spin density distribution shown in Figure 7. We calculate[54] the number of effectively unpaired electrons to be 1.58 with M06-2x and 1.42 with B97D (due to the difference in amount of exchange) further indicating high diradical character. This is smaller than the value of 2.08 found in the second-order saddle point **7** in the synchronous path. It can then be argued that one of the reasons for the preference of the stepwise asynchronous path is that it minimizes the amount of high-energy diradical character. This intermediate is separated by small barriers on both sides to the two transition structures TS1 and TS2, and therefore in a practical sense the whole region around these structures behave as a transition state in the transformation.

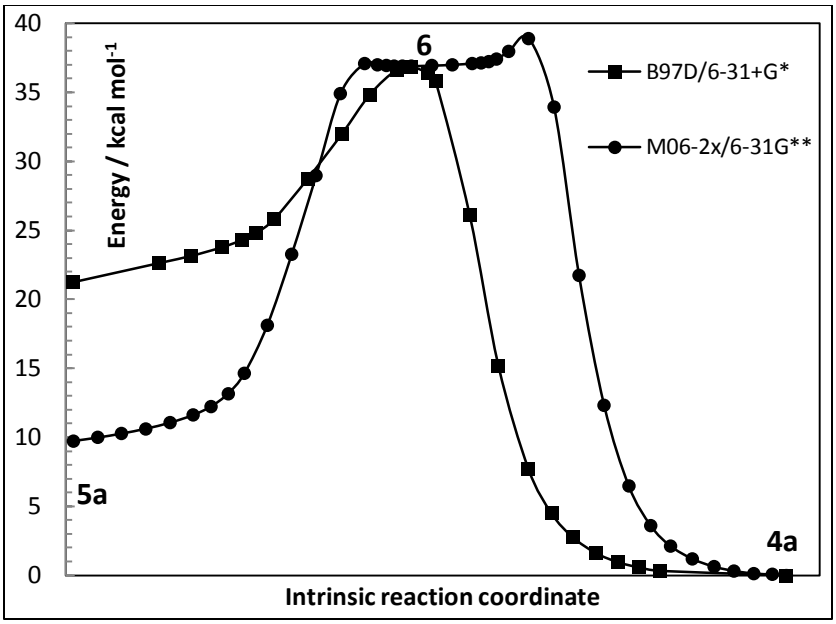

Figure 13. Total energy along the intrinsic reaction coordinate of Fig. 12 for the asymmetric thermal cycloaddition pathway (left: **5a** to right: **4a**) calculated at the UB97D/6-31+G(d) (squares) and UM06-2x/6-31G(d,p) (circles) levels.

Volume change during reaction

Table 2 contains the calculated molecular volumes of the various species presented in this work with various model chemistries. We found the need for the inclusion of diffuse functions in order accurately match experimental X-ray volumes where available. This was particularly clear for **4b**. For this reason we calculated the molecular volumes using a variety of basis sets at both DFTs. The calculated volumes of both transition structures **6** and **7** are the same within one standard deviation, giving credence to the proposed dissociation mechanism involving a TS with a smaller molecular volume.[1] The calculated volume change is about 15-19%, much larger than the ~3% obtained experimentally[1]. We expect this discrepancy to be largely due to the difference between the experiment in a polymer matrix, where reactant molecules are encapsulated, and the gas phase calculation. The reduction of the molecular volume is significant in the TS region fully supporting at the atomistic level the mechanism proposed by Jezowski et al.[1]

Table 2. Molecular volumes[a] of the various species in this work.

Species	Exp.[b]	UB97D/6-31+G(d)	UM06-2x/6-31G(d,p)
4a	-	508.3	431.5
4b	510.3	505.3	429.3[d]
5a	506.5[c]	507.1	493.2
6	-	437.0	429.8
7	-	433.3	425.0

[a]Volumes are in $Å^3$. [b]X-ray structures taken from reference 7. [c]Experiment is on the D2h structure (**5b**). [d]When diffuse functions are added, we obtain volumes of 501.2 and 505.5 for the basis sets 6-31+G(d) and 6-31+G(d,p), respectively.

Conclusions

The [4+4] cycloaddition in [2.2] (9,10)anthracenophane process has similarities to the diamond-to-graphite transition. We calculated two pathway PES, a synchronous change and an asymmetric change, and observe the sp^3-sp^2 change during photoisomerization mimics the carbon allotropic change in some respects. Among them, the complete absence of stationary points with nearest neighbor CC distances around 2.20 Å. In fact, this distance seems to be "off limits" and we know of molecule exhibiting this distance between sp^3 carbons except in the crowded environment of cyclic compounds. The change in d_{12} is subtle away from the transition structure but dramatic at 2.1 Å < d(1-2) < 2.3 Å, where it is clear that there is no geometry that can satisfy a minimum energy structure and instead we find transition structures in this range. By breaking (or completing) the bond separated by either d(1-2) or d(3-4) before the other, higher energy structures in which both of these distances must be near 2.3 Å simultaneously is circumvented and this asymmetric pathway reduces the barrier by 10 kcal mol^{-1} relative to the

synchronous path. A diradical structure is found along the assymetric path, near the transition, but whether this structure is a true minimum depends on the model chemistry used. Quenneville and Germann[30] noted that the lowest energy path is synchronous for the dimerization of anthracene at the 9 and 10 sites as here without the tethers present in this work although they also noticed a diradicaloid intermediate on the triplet surface. This is in contrast to our lowest energy path with proceeds via a singlet diradicaloid asymmetrical (stepwise) intermediate. The effect of the tethers is to holds the pairs of the 9 and 10 sites in proximity during the reaction.

The molecular results inspire the thought that an alternative asymmetric-type path might be modeled in the diamond-to-graphite transition that passes through a smaller barrier compared to the simple synchronous path. The computed reduction of the molecular volume is significant in the TS region regardless of the applied density functional fully supporting the pressure accelerated reaction mechanism proposed by Jezowski et al.[1]

Acknowledgement. We thank the National Science Foundation for its support of this research (grant number CHE-1006702).

Supporting Information

Table S1. Optimized parameters for the diamond, graphite, and transition structures used in this work.

	a / Å	α / °	q / Å	r / Å	θ /°
Diamond	2.52	60.00	1.544	1.544	109.5
Transition structure (TS)	2.768	53.50	2.060	1.471	101.95
Graphite	3.978	36.11	3.714	1.420	90.0

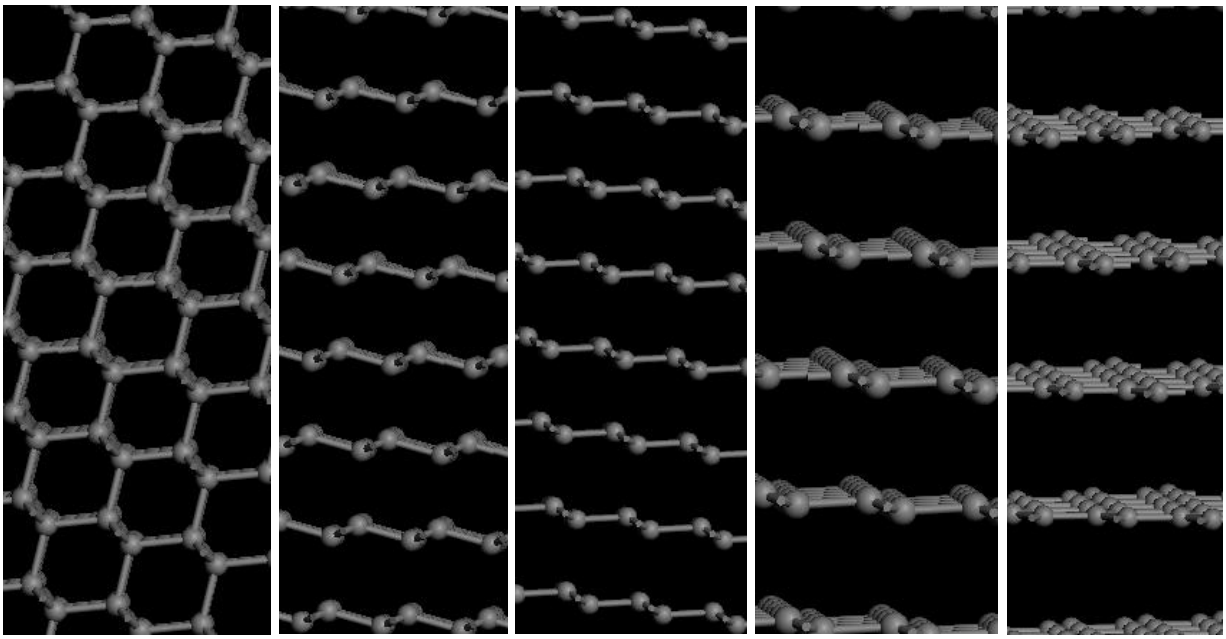

Figure S1. Five images of the diamond-to-graphite transition with (left to right) q=1.54, 1.7, 2.0, 2.3, 3.34.

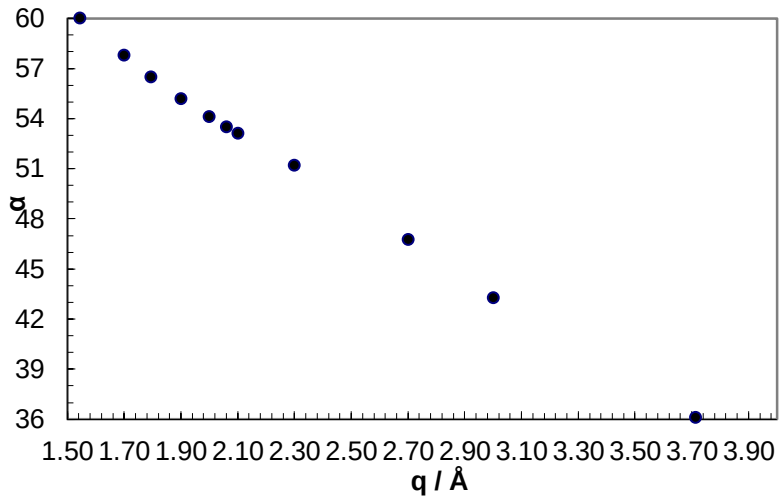

Figure S2. Change in the cell parameter α with inter-layer separation q diamond to graphite transition**.** Data correspond to the relaxed scan in Figure 3.

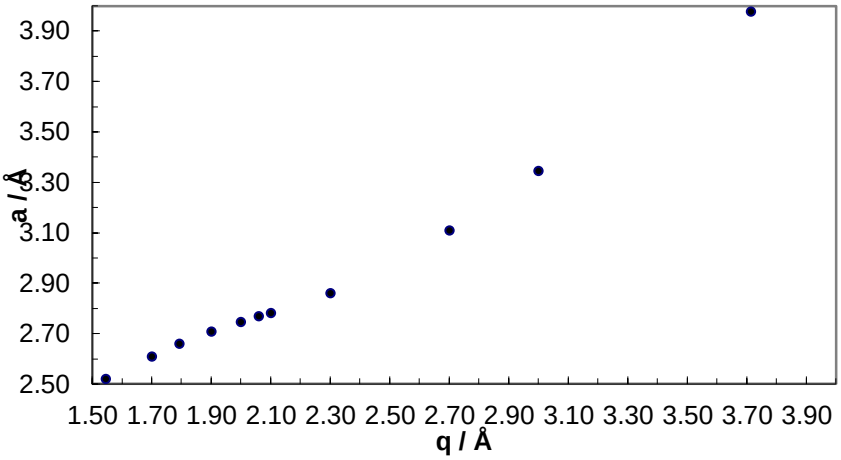

Figure S3. Change in the cell parameter *a* with inter-layer separation *q* diamond to graphite transition. Data correspond to the relaxed scan in Figure 3.

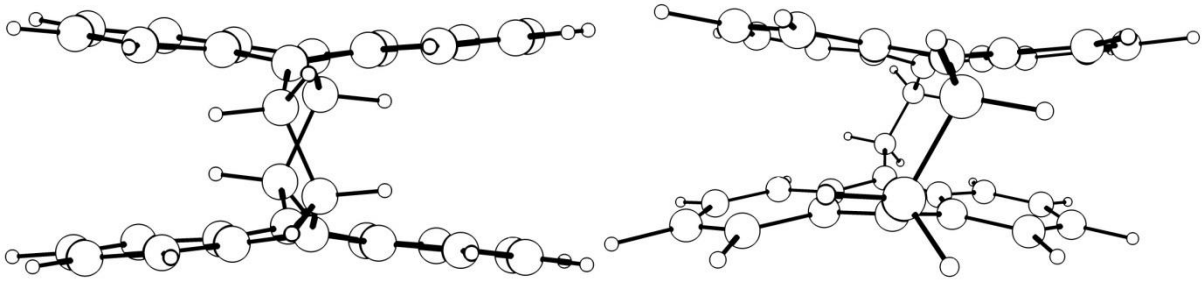

4a **4b**

Figure S4. [2.2] (9,10)anthracenophane with D_2 symmetry (left) and C_2 symmetry (right). **4a** is calculated to be lower in energy by 0.75 kcal mol^{-1} at the M06-2x/6-31G(d,p) level.

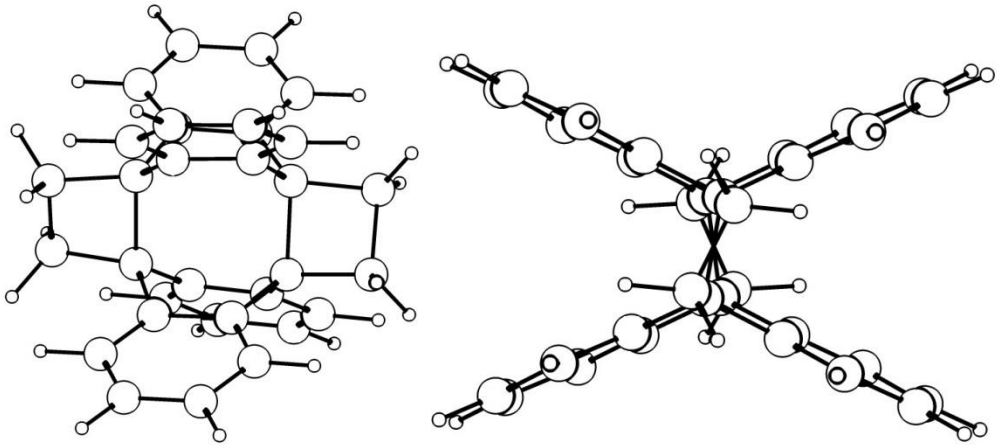

5a

Figure S5. Two views of the optimized geometry of the cycloaddition product **5a** (D_2 symmetry) at the M06-2x/6-31G(d,p) level.

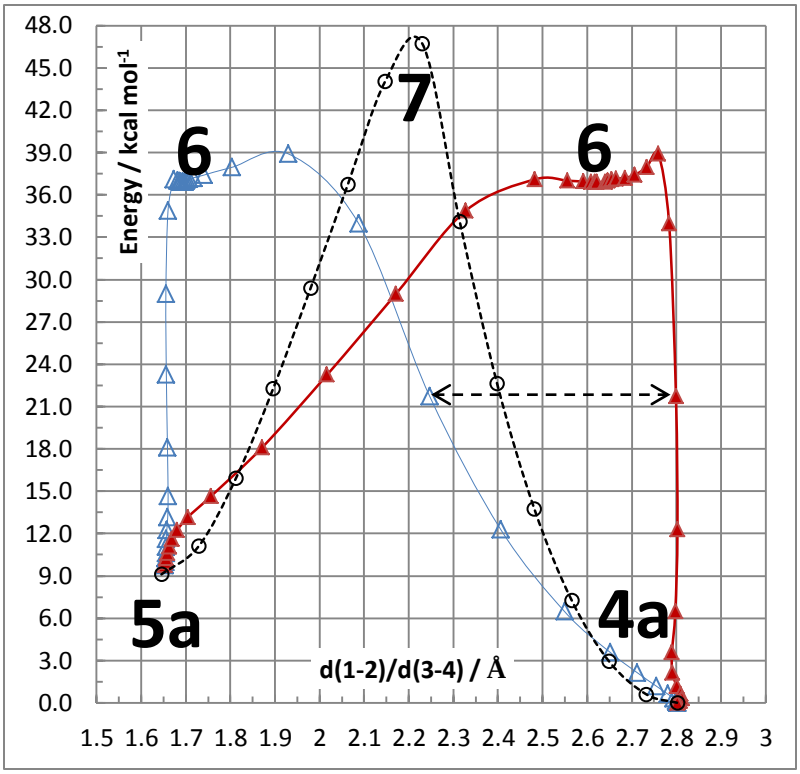

Figure S6. Change in the parameter d(1-2)/d(3-4) for both thermal pathways discussed in this work calculated at the UM06-2x/6-31G(d,p) level. Blue and red triangles plot the changes in d(1-2) and d(3-4), respectively, in the assymetric path. Note that initially d(1-2) changes little as d(3-4) elongates until the first transition state (TS1), at which point d(1-2) breaks. The broken black line (circles follows the synchronous path where d(1-2)=d(3-4) universally. A pair of corresponding d(1-2)/d(3-4) values is indicated by the horizontal dashed line with arrows.

References

[1] Jezowski, S. R.; Zhu, L; Wang, Y.; Rice, A. P.; Scott, G. W.; Bardeen, C. J.; Chronister, E. L.*J. Am. Chem. Soc*. **2012**, *134*, 7459-7466.

[2] Wen, X.-D.; Hoffmann, R.; Ashcroft, N. W. *J. Am. Chem. Soc.* **2011**, *133*, 9023-9035.

[3] Beneditti, L. R.; Nguyen, J. H.; Caldwell, W. A.; Liu, H.; Kruger, M.; Jeanloz, R. *Science* **1999**, *286*, 100.

[4] Zeng, Q.; He, Z.; San, X.; Ma, Y.; Tian, F.; Cui, T.; Liu, B.; Zou, G.; Mao, H. *Proc. Nat. Acad. Sci*. **2008**, *105*, 4999-5001.

[5] Streek, J. *Acta Crystalogr. B*, **2006**, *62*, 567-579.

[6] Fokin,A.A.; Chernish, L.V.; Gunchenko,G.A.; Tikhonchuk, E.Y.; Hausmann, H.; Serafin, M.; Dahl, J,E.P.; Carlson, R.M.K.; Schreiner, P.R. *J. Am. Chem. Soc.* **2012**, *134*, 13641-50.

[7] Trzop, E.; Turowska-Tyrk, I. *Acta Crystallogr. B.* **2008**, *64*, 375-382.

[8] Komarov, I. V. *R. Chem. Rev*. **2001**, *70*, 991-1016.

[9] Tantillo, D. J. *Chem. Soc. Rev*. **2010**, *39*, 2847-2854.

[10] Bremer, M.; Schotz, K.; Schleyer, PVR.; Fleischer, U.; Schindler, M.; Kutzelnigg, W.; Koch, W.; Pulay, P. *Angew. Chem. Int. Ed. Engl*. **1989**, *28*, 1042-1044.

[11] Laube, T.; Lohse, C. *J. Am. Chem. Soc*. **1994**, *116*, 9001-9008.

[12] Toda, F.; Tanaka, K.; Stein, Z.; Goldberg, I. *Acta Crystallogr. C*, **1996**, *52*, 177-180.

[13] Kawai, H.; Takeda, T.; Fujiwara, K.; Inabe, T.; Suzuki, T. *Cryst. Growth Des*. **2005**, *5*, 2256-2260.

[14] Tsuji, T. *Adv. Strained Interesting Org. Mol*. **1999**, *7*, 103-152.

[15] *Modern Cyclophane Chemistry*; Gleiter, R., Hopf, H., Eds.; Wiley-VCH: Wienheim, Germany, 2004.

[16] Xin, D.; Ma, Y.; He, F. *Tetrahedron: Asymmetry* **2010**, *21*, 333-338.

[17] Cheemala, M. N.; Gayral, M.; Brown, J. M.; Rossen, K.; Knochel, P. *Synthesis*. **2007**, *24*, 3877-3885.

[18] Bartholomew, G. P.; Bazan, G. C. *Acc. Chem. Res.* **2001**, *34*, 30-39.

[19] Meier, H.; Cao, D. *Chem. Soc. Rev.* **2013**, *42*, 143-155.

[20] Winberg, H.E.; Fawcett, F. S. *Org. Synth.* **1962**, *42*, 83.

[21] Hope, H.; Bernstein, J.; Trueblood, K. N. *Acta Crystallogr. B.* **1972**, *28*, 1733-1743.

[22] Gantzel, P. K.; Trueblood, K. N. *Acta Crystallogr. B*. **1965**, *18*, 958-968.

[23] Dodziuk, H.; Szymanski, S.; Jazwinski, J.; Marchwiany, M. E.; Hopf, H. *J. Phys. Chem. A* **2010**, *114*, 10467-10473.

[24] Zhou, X.; Liu, R.; Allinger, N. L. *J. Am. Chem. Soc*. **1993**, *115*, 7525-7526.

[25] Choi, C. H.; Kertesz, M. *Chem. Commun*. **1997**, *22*, 2199-2200.

[26] Orimoto, Y.; Aoki, Y. *Int. J. Quant. Chem*. **2002**, *86*, 456-467.

[27] Dodziuk, H.; Szymanski, S.; Jazwinski, J.; Ostrowski, M.; Demissie, T. B.; Ruud, K.; Kus, P.; Hopf, H.; Lin, S. *J. Phys. Chem. A*. **2011**, *115*, 10638-10649.

[28] Grimme, S.; Muck-Lichtenfeld, C. *Isr. J. Chem*. **2012**, *52*, 180-192.

[29] Bachrach, S. M. *J. Phys. Chem. A*, **2011**, *115*, 2396-2401.

[30] Quenneville, ,J.; Germann, T.G. *J. Chem. Phys*. **2009**, *131*, 024313.

[31] Gaussian 09, Rev. A.02, Frisch, M. J.; Trucks, G. W.; Schlegel, H. B.; Scuseria, G. E.; Robb, M. A.; Cheeseman, J. R.; Scalmani, G.; Barone, V.; Mennucci, B.; Petersson, G. A.; Nakatsuji, H.; Caricato, M.; Li, X.; Hratchian, H. P.; Izmaylov, A. F.; Bloino, J.; Zheng, G.; Sonnenberg, J. L.; Hada, M.; Ehara, M.; Toyota, K.; Fukuda, R.; Hasegawa, J.; Ishida, M.; Nakajima, T.; Honda, Y.; Kitao, O.; Nakai, H.; Vreven, T.; Montgomery, Jr., J. A.; Peralta, J. E.; Ogliaro, F.; Bearpark, M.; Heyd, J. J.; Brothers, E.; Kudin, K. N.; Staroverov, V. N.; Kobayashi, R.; Normand, J.; Raghavachari, K.; Rendell, A.; Burant, J. C.; Iyengar, S. S.; Tomasi, J.; Cossi, M.; Rega, N.; Millam, J. M.; Klene, M.; Knox, J. E.; Cross, J. B.; Bakken, V.; Adamo, C.; Jaramillo, J.; Gomperts, R.; Stratmann, R. E.; Yazyev, O.; Austin, A. J.; Cammi, R.; Pomelli, C.; Ochterski, J. W.; Martin, R. L.; Morokuma, K.; Zakrzewski, V. G.; Voth, G. A.; Salvador, P.; Dannenberg, J. J.; Dapprich, S.; Daniels, A. D.; Farkas, Ö.; Foresman, J. B.; Ortiz, J. V.; Cioslowski, J.; Fox, D. J. Gaussian, Inc., Wallingford CT, 2009.

[32] Zhao, Y.; Truhlar, D. G. *Theor. Chem. Acc*. **2008**, *120*, 215-41.

[33] Grimme, S. *J. Comp. Chem.* **2006**, *27* 1787-1799.

[34] Petersson, G. A.; Al-Laham, M. A. *J. Chem. Phys.*, **1991**, *94*, 6081-90.

[35] Peng, C.; Ayala, P. Y.; Schlegel, H. B.; Frisch, M. J. *J. Comp. Chem*. **1996**, *17*, 49-56.

[36] Hratchian, H. P.; Schlegel, H. B. *J. Chem. Theory Comput*. **2005**, *1*, 61-69.

[37] Wong, M. W.; Wiberg, K. B.; Frisch, M. J. *J. Comput. Chem*. **1995**, *16*, 385–394.

[38] Boa, D.; Ramu, S.; Contreras, A.; Upadhyayula, S.; Vasquez, J. M.; Beran, G.; Vullev, V. I. *J. Phys. Chem. B* **2010**, *114*, 14467-79.

[39] Quantum ESPRESSO is a community project for high-quality quantum-simulation software, based on density-functional theory, and coordinated by Paolo Giannozzi. See http://www.quantum-espresso.org and http://www.pwscf.org.

[40] Perdew, J.P.; Burke, K.; Ernzerhof, M. *Phys. Rev. Lett*. **1996**, *77*, 3865-3868.

[41] See http://www.physics.rutgers.edu/~dhv/uspp/uspp-cur/Work/006-C/006-C-gpbe--bm/

[42] Kertesz, M.; Hoffmann, R. *J. Solid State Chem.* **1984**, *54*, 313-319.

[43] Fahy, S.; Louie, S.G.; Cohen, M.L. *Phys. Rev. B* **1986**, *34*, 1191-1199.

[44] Blanksby, S. J.; Ellison, G. B. *Acc. Chem. Res*. **2003**, *36*, 255-263.

[45] Mau, A. W. H. *J. Chem. Soc.-Faraday Trans. I,* **1978**, *74*, 603-612.

[46] Wada, A.; Tanaka, J. *Acta Crystallogr. B*. **1977**, *33*, 355-360.

[47] Harada, J.; Ogawa, K.; Tomoda, S. *Chem. Lett*. **1995**, 751-752.

[48] Ehrenberg, M. *Acta Crystallogr*. **1966**, *20*, 182-186.

[49] Dougherty, D. A.; Choi, C. S.; Kaupp, G.; Buda, A. B.; Rudzinski, J. M.; Osawa, E. *J. Chem. Soc., Perkin Trans. 2*. **1986**, 1063-1070.

[50] Battersby, T. R.; Gantzel, P.; Baldridge, K. K.; Sigel, J. S. *Tetrhedron Lett*. **1995**, *36*, 845-848.

[51] Grimme, S. *Chem.—Eur. J*. **2004**, *10*, 3423-3429.

[52] Lyssenko, K. A.; Antipin, M. Y.; Antonov, D. Y. *ChemPhysChem*. **2003**, *4*, 817-823.

[53] Staroverov, V.N.; Davidson, E.R. *J. Am. Chem. Soc.* **2000**, *122*, 7377-7385.

[54] Head-Gordon, M. *Chem. Phys. Lett*. **2003**, *372*, 508-511.